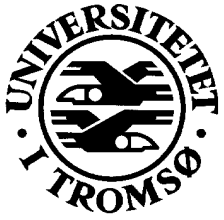

Cand. Scient Thesis
University of Tromsø

Design control and diagnostics of an electron cyclotron resonance plasma source for thin film deposition

by
Ane Aanesland
March 1999

Faculty of Science
Department of Physics
University of Tromsø, N-9037 Tromsø, Norway, Telephone +47 77 64 51 50, Telefax +47 77 64 55 80

Jeg sa til ordene: Bli ånd!
Bli liv! Bli kjøtt og blod og sånn!
Men ordene skjøt rygg og sa:
«Hvor skal vi hente ånden fra?

Fra "Ordene" av
Inger Hagerup

Acknowledgments

It has been a privilege for me to spend so many years of my life learning physics. The most important things I have learnt through the years, though, are patience and initiativ. This goes to my family who made me curious; mum Ina, dad Inge and sister Liv.

The present work was carried out at the Department of Physics, The Birkeland laboratory. First of all I want to thank my supervisors, Åshild Fredriksen and Kristoffer Rypdal, for introducing me to this upcoming field of science. Luckily neither of us knew the trouble ahead when we started, and despite a lot of hardship we survived.

Specially thanks to you, Åshild, for never letting me down the last couple of months with the Atlantic in between. You have patiently improved my English, been constructive towards my ideas, given me new ones and lead me in the right direction.

Secondly, many thanks to Terje Brundtland, Kjell-Arne Willumstad and Knut Sandaker for your expertise and valuable technical support in the construction and assembling of Menja, and for your general helpfulness.

Göran Hellblom for very good cooperation when Menja was assembled and during the first experiment with deposition. We made it!

All my fellow students and friends, at "Norutbrakka" and elsewhere. There have been quite a few moments worth remembering! Thank you all for being there.

Last, but not least, Arne, for your never failing support and love.

Ane Aanesland
Tromsø, March 1999

Contents

Chapter 1

Introduction

1.1 Properties of the ECR plasma source

It is well recognized that magnetically assisted microwave produced plasmas have led to substantial improvements in the fabrication of electric components. In the late seventies the Japanese developed the plasma etching technique as a substitute for the reactive ion etching, by the use of a divergent field electron cyclotron resonance (ECR) plasma reactor (Suzuki *et al.*, 1977). Since then, ECR-plasma sources have been extensively applied to numerous low-pressure plasma processing applications as etching, deposition and ion implantation.

The ECR source offer several advantages compared to the common parallel-plate- or rf-discharge or compared to the conventional chemical process. The microwave power is usually introduced into the vacuum chamber through a dielectric window, and therefore there is no need for electrodes in the plasma to achieve a discharge. Thus, plasma processing can be carried out without the electrodes which is a source of impurities, so that lower contaminations in the plasma process are expected. This electrode-less power coupling also creates high plasma density with low sheath potentials. The impact ion energy on the substrate can therefore be controlled from an independently driven dc-

or rf-source, coupled to the electrode on which the substrate is placed. The degree of ionization, and hence the plasma density can achieve values well above those of low-frequency rf-discharges. The electron density increases with power. Hence, independent control of the ion flux, controlled by input power, and ion-bombarding energy, controlled by dc/rf-source, are possible. The resonant power absorption also allows operation in a extremely wide range of gas pressures. The degree of ionization also seems responsible for the high production rate of reactive particles which cause the high deposition or etching rates in these devices. With these arguments in mind the ECR source have large opportunities with respect to processing applications.

1.2 Previous work

Several important reviews of microwave heated plasmas have been published the last ten years. Among these that are worth noting are; the early work of Asmussen (1989) and Musil (1986) which review the ECR plasma technology for material science; the more recent reviews by Lieberman and Lichtenberg (1994), Lieberman and Gottscho (1994) and Popov (1994) which treat the plasma physics of this sources; Moisan and Pelletier (1992) which deals with the microwave heating of plasmas in general; and the newest review by Asmussen *et al.* (1997) which takes an engineering approach towards the understanding of ECR plasmas.

Several experiments have been done, investigating the etching properties in ECR reactors (Ono *et al.*, 1986; Gadgil *et al.*, 1992; Gorbatkin and Barry, 1992b; Ma *et al.*, 1992; Tempermeister *et al.*, 1994). In all these experiments cited here the etch rate, uniformity and selectivity in poly-silicon etching are investigated, with the emphasis upon the influence of the rf-bias on the substrate and microwave input power. The plasma enhanced deposition process are studied by several authors with a wide range of deposition materials. Matsuo and Kiuchi (1983) and Popov *et al.* (1994) deposit silicon dioxide films, Ono *et al.* (1984) deposit metallic compound films such as tantalum oxide and aluminum oxide, and Spee *et al.* (1995) and Kim *et al.* (1997)

deposit titanium nitride (TiN) films. Common for all these experiments is the investigation of how deposition rate and uniformity depends upon the gas flow rate and microwave power.

Although several experiments have been performed in ECR plasma sources during the last ten to fifteen years, the characterization of the plasma parameters and their influence on the plasma process is not yet fully understand. Thus, there is a lot of research left to obtain a complete insight in the process.

The goal of this thesis is therefore to design an ECR-plasma source for thin film deposition processes. This source is baptized Menja[1], and the source will be referred to by this name. Further goals are to control and characterize the plasma parameters produced in the source with the emphasis on the plasma density, plasma potential, electron and ion temperature. Also an attempt to deposit TiN film on a substrate will be done.

1.3 Contents

In chapter 2 we will present a brief introduction to the plasma enhanced chemical vapor deposition (PECVD) technique. In the following sections the heating mechanism of microwave discharges are discussed and calculation of some plasma parameters are made. The sheath formation is described in chapter 3, together with the theory of the probes used in this thesis, i.e. the Langmuir probes, the flux probe and the ion energy analyzer (IEA). The design consideration of the IEA-probe are also given. Chapter 4 concerns the design of the electron cyclotron resonance plasma source, Menja. The results obtained with the different probes in Menja are presented in chapter 5 and discussed in chapter 6. In chapter 7 we draw conclusions from this work, and suggestion for further research will be given.

[1] After a thrall-woman from Norse mythology

Chapter 2

Theory

2.1 Introduction to PECVD

The plasma enhanced chemical vapor deposition (PECVD) technique is reviewed in several books and papers. Lieberman and Lichtenberg (1994, chapter 16) and Musil (1986) describe the general process of deposition and implantation in microwave plasmas. Spee *et al.* (1995) present a review from a chemical point of view with the example of TiN deposition, while Asmussen *et al.* (1997) discuss several illustrative ECR plasma-processing applications, i.e. deposition and etching.

The plasma enhanced process which improve the thin film deposition is complicated and strongly dependent on many parameters. A complete understanding of the process requires good knowledge of chemistry, plasma physics, as well as solid state physics. It is clearly demonstrated that the plasma parameters play a significant role in the formation of thin films. A precise monitoring and control of the plasma during the deposition process is the only way to produce films with fully reproducible properties (Musil, 1986). In this thesis a brief description of the technique is given, with emphasis on the influence of the plasma particles on the process.

In conventional chemical vapor deposition (CVD) a solid thin film is formed on a substrate by a set of chemical reactions, usually at atmospheric pressure. Reactant gases enter the process chamber and are heated as they approach the hot substrate surface to be coated. Depending on the operating conditions, the reactant gases may undergo homogeneous chemical reactions in the vapor phase before striking the surface of the substrate. The film formation is controlled by the substrate temperature, the available chemical products in the vapor phase, and substrate surface characteristics such as density and morphology. The drawback of the CVD process is the high temperature ($600 - 1100°C$) of the substrate required to deposit a good quality film (Spee *et al.*, 1995). Hence, the range of substrates that can be coated by CVD is limited, since the substrate needs a high melting point. Spee *et al.* (1995) show that one way to lower the minimum temperature necessary to initiate the desired chemical reactions or decomposition is to change the chemistry, which can be done by introducing another reactant gas into the chamber. Temperatures in the range of $200 - 300°C$ are however still necessary for some applications, and therefore new technologies are required.

One of the most promising improvements is the PECVD technology. There are mainly two different methods in the PECVD process, remote- and direct-PECVD. In the remote-PECVD the plasma is generated a certain distance from the substrate surface. Thus, before the ions and electrons reach the substrate they have recombined by collisions, so only neutral particles exist in the neighborhood of the substrate. The direct-PECVD expose the substrate directly by the plasma particles and is the most common PECVD deposition process (Spee *et al.*, 1995). Thus, this process is briefly explained in this section, and illustrated in Figure 2.1.

In all deposition processes there are atoms and molecules, called precursors, that undergo the desired reactions to form the thin film on the substrate. In the CVD process these precursors are the input gases, whose composition depend on the result wanted. In all conventional CVD processes where the reactions are controlled and determined by the substrate temperature, precursors need high reaction temperatures. Such temperatures normally require substrate heating. In the PECVD one makes use of the plasma-chemical

process which has two basic properties (Musil, 1986):

i. Electrons with energy exceeding the threshold binding energy in the molecule can break the initial chemical bonds and dissociate the molecule by collisions. Hence, the electrons excite and activate the working gas, the precursors, to initiate chemical reactions at or near room temperature. The result is that no heating of the deposited substrate is necessary to initiate the desired chemical reactions.

ii. Ions produced in the plasma can be accelerated to the surface of the substrate and bombard the deposited film. Depending on the ion energy this can influence significantly the film growth, its composition, microstructure and stress.

The characteristic of good film quality depend on the particular application. Some common properties are minimum contamination and lattice holes in the film, high sticking coefficient, and high uniformity. To reduce cost also a high deposition rate is required. To obtain the desired film composition the choice of precursor and how it is introduced to the system need careful consideration. The precursor is either introduced as a molecular gas or as a solid target into the reaction chamber as illustrated in figure 2.1. Matsuo and Kiuchi (1983) deposited silicon nitride, Si_3N_4, and silicon dioxide, SiO_2, films in a low pressure divergent ECR plasma. Nitrogen or oxygen and precursor, silane SiH_4, gases were introduced into the plasma and reaction chamber, respectively. The introduced gases are efficiently transported and react to form a film, and the amount of hydrogen in the film is very small. A simplified illustration of this process is shown in Figure 2.1(a). With this method high quality film can be obtained, but the method is somewhat restricted since the materials must be introduced in the form of chemical vapor (Ono *et al.*, 1984). Therefore, Ono *et al.* produced a metal and metallic compound deposition by placing a metal sputter target, tantalum, around the exited plasma stream in the chamber. Sputtering argon gas was introduced into the plasma chamber, and reactive oxygen gas into the process chamber. The simplified process is shown in Figure 2.1(b). Ono *et al.* showed that film

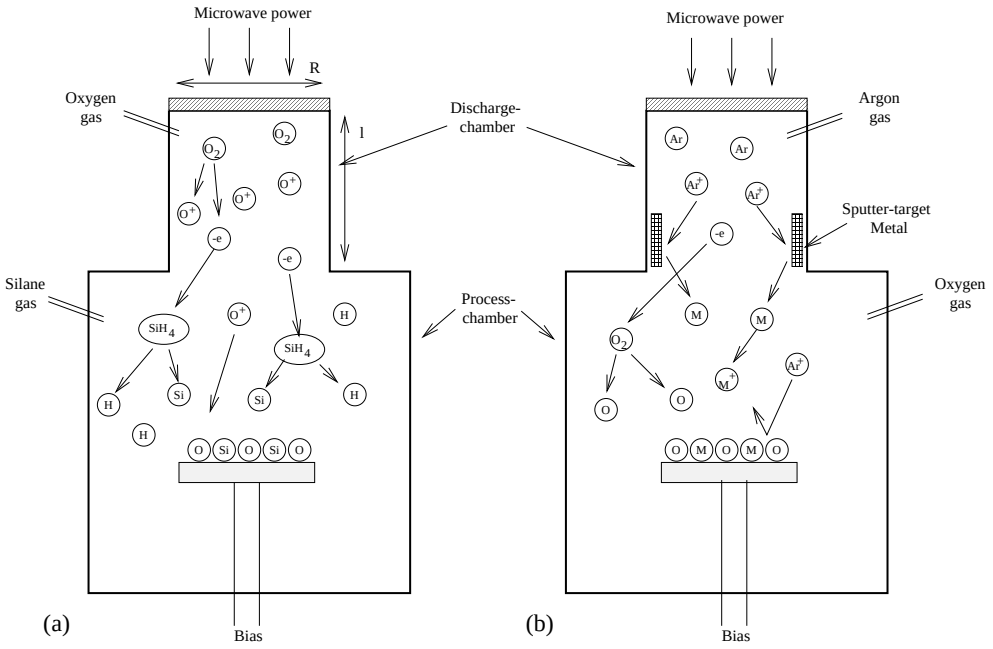

Figure 2.1: A simple illustration of the deposition process in direct-PECVD. (a) shows deposition of a silicon dioxide film using the vapor phase precursors silane. (b) shows a deposition of a metallic oxide film with use of a sputtering metal target.

quality and deposition rate depends on the input microwave power and the gas pressure, where a high quality film and high rate deposition cannot be performed simultaneously. The film composition depends on the reactants available. If some of the components in the desired reaction are missing or not available, other reactions may occur on the surface, thus leading to an undesired contamination. A dense plasma with high to moderate electron or ion energies may assure effective dissociation or sputtering of precursors, which gives access to the required reactants and therefore reduces the problem of contamination.

The plasma ions can be accelerated by electric and magnetic fields, hence by changing the magnetic field configuration or the bias on the substrate the impact energy of the ions to the substrate can easily be manipulated. At low energies these ions can cause enhanced desorption of reactant products, while at high energies they can be implanted (Spee *et al.*, 1995). Thus, changing

the ion energies may affect the lattice of the deposited film, and improve the sticking coefficient so that the thin film does not peel off after deposition (Lieberman and Lichtenberg, 1994). Matsuo and Kiuchi (1983) and Ono *et al.* (1984) used ion energies of the order of 20 eV during deposition. If the ion flux into the substrate increases, the efficiency of the plasma-chemical synthesis of the film and their growth rate increase, thus a denser plasma yields a larger deposition rate (Musil, 1986). Also a good ion flux uniformity, i.e. a uniform plasma, provides a deposited film of high uniformity.

Unfortunately, there are still some deposition processes that require moderate heating of the substrate to achieve good film quality. It has been shown that the lowest deposition temperature necessary to deposit good quality TiN layers is about 450°C, thus the substrate material is heated just sufficiently to ensure surface mobility and reactions (Spee *et al.*, 1995). The first successful deposition of silicon nitride without substrate heating was performed by Matsuo and Kiuchi (Asmussen *et al.*, 1997). The substrate temperature during deposition was in the range from $50 - 150$°C, due to some heating effects by the plasma.

The description given in this section shows that good film quality depends on many parameters. The most important plasma properties are energy and density of electrons and ions and their degree of plasma ionization and uniformity are important (Musil, 1986). For this reason the heating mechanism and calculation of T_e and N_0 are discussed in the following sections.

2.2 Heating of microwave discharges

In microwave discharges the operating pressure is usually low, so that the average energy of the electrons is much larger than the average energy for the heavy ions and neutrals. The excitation and ionization of atoms and molecules are only consequences of electron impact on these heavy species (Wertheimer and Moisan, 1994). The operation microwave frequency is high, usually 2.45 GHz. Hence, the ions are so massive that they do not respond

to the time dependent electromagnetic field. Only the electrons are able to absorb energy from the field. In this section we will treat the case with no magnetic field, and show that the energy transfer is due to collisional processes. In the following sections we look at the case when a magnetic field is introduced, which leads to a collisionless energy transfer.

Power transfer in the absence of a magnetic field

The time and space varying microwave energy which maintains the discharge is represented by the electric field $\boldsymbol{E}(t) = \boldsymbol{E}_0 e^{j\omega t}$. The wave amplitude, $\boldsymbol{E_0}$, is a function of position $\boldsymbol{r}$, and ω is the wave frequency. Consider the plasma to consist of a single fluid of electrons immersed in a background of immobile ions. The thermal electron motion is neglected, which is the cold plasma approximation. Due to this approximation the electron velocity is determined by the electric field. The equation of motion for the electrons in this case is (Goldston and Rutherford, 1995)

$$m_e \frac{d\boldsymbol{v}}{dt} = -e\boldsymbol{E} - m_e \nu_c \boldsymbol{v}, \tag{2.1}$$

where m_e is the electron mass, e is the electron charge and ν_c is the average electron-neutral collision frequency for momentum transfer. Solving 2.1 with respect to the electron velocity we obtain

$$\boldsymbol{v} = \frac{-e\boldsymbol{E}}{m_e(j\omega + \nu_c)}. \tag{2.2}$$

Due to the electromagnetic field the electrons experience a Lorenz force which is equal to $\boldsymbol{F} = -e\boldsymbol{E}$. The work done on the electron per unit time is then $\boldsymbol{F} \cdot \boldsymbol{v}$. The average over a wave period gives the mean power transfer per electron, yielding

$$\begin{aligned} \theta_A = \langle \mathrm{Re}(\boldsymbol{F}) \cdot \mathrm{Re}(\boldsymbol{v}) \rangle &= -\frac{e}{4} \langle (\boldsymbol{E} + \boldsymbol{E}^*) \cdot (\boldsymbol{v} + \boldsymbol{v}^*) \rangle \\ &= -\frac{e}{2} \left[\mathrm{Re}\langle \boldsymbol{E} \cdot \boldsymbol{v}^* \rangle + \mathrm{Re}\langle \boldsymbol{E} \cdot \boldsymbol{v} \rangle \right]. \end{aligned} \tag{2.3}$$

Now, using equation 2.2 we note that

$$\begin{aligned}\langle \boldsymbol{E} \cdot \boldsymbol{v}^* \rangle &= -\frac{eE_0^2}{m_e(-j\omega + \nu_c)} \\ &= -\frac{\nu_c e E_0^2}{m_e(\nu_c^2 + \omega^2)} - \frac{j\omega e E_0^2}{m_e(\nu_c^2 + \omega^2)}\end{aligned} \tag{2.4}$$

and that

$$\langle \boldsymbol{E} \cdot \boldsymbol{v} \rangle = -\frac{eE_0^2}{m_e(j\omega + \nu_c)} \langle e^{2j\omega t} \rangle = 0, \tag{2.5}$$

hence we get (Moisan and Pelletier, 1992)

$$\theta_A = \frac{e^2}{m_e} \left(\frac{\nu_c}{\nu_c^2 + \omega^2} \right) \frac{E_0^2}{2}. \tag{2.6}$$

θ_A is the power delivered from the microwaves and absorbed by the electrons, and $\boldsymbol{v}^*$ is the complex conjugate electron velocity.

In the absence of collisions, $\nu_c = 0$, we can see from equation 2.6 that $\theta_A = 0$. The electron velocity is in anti-phase with the electric field, so the electrons will in the first half of the period be accelerated in one direction, and in the second period in the opposite direction, and during the whole period these accelerations will cancel out. Consequently, no net work is done and no energy is gained by the electrons.

In the presence of collisions, $\theta_A \neq 0$, the electrons receive energy in a random process. During one wave period the electron motion will be disturbed by collisions and the energy gain during the interrupted period is positive. Hence, electrons receive energy from one interrupted period and then from the next interrupted period and so on. Finally the electron energy exceeds the threshold energy for ionization or excitation of the heavy neutrals, and a discharge occurs and is maintained.

Power transfer in the presence of a magnetic field

Wave modes in a magnetized plasma

There are four principal wave modes of the electric field in a magnetized plasma (Geller, 1996). Electromagnetic waves can be launched into the vac-

Wave mode	$\boldsymbol{E}$ direction	$\boldsymbol{k}$ direction	Polarization	Resonance
O-mode	$\boldsymbol{E} \parallel \boldsymbol{B}$	$\boldsymbol{k} \perp \boldsymbol{B}$	Linear	no
X-mode	$\boldsymbol{E} \perp \boldsymbol{B}$	$\boldsymbol{k} \perp \boldsymbol{B}$	Elliptical	UHR
R-mode	$\boldsymbol{E} \perp \boldsymbol{B}$	$\boldsymbol{k} \parallel \boldsymbol{B}$	RHP	ECR
L-mode	$\boldsymbol{E} \perp \boldsymbol{B}$	$\boldsymbol{k} \parallel \boldsymbol{B}$	LHP	no

Table 2.1: The four principal modes are listed, showing the direction of $\boldsymbol{E}$ and $\boldsymbol{k}$ with respect to $\boldsymbol{B}$. The wave polarization and what resonances occur are also listed. RHP and LHP is the right- and left- hand polarized wave and UHR and ECR is the upper hybrid and electron cyclotron resonance, respectively.

uum chamber parallel or perpendicular to the magnetic field $\boldsymbol{B}$, and thus different wave modes propagating in the plasma are obtained. Some of the modes produce a resonance with the plasma electrons and some have no influence on the electrons. The four principal modes, with their characteristic qualities, are listed in Table 2.1.

For perpendicular propagation, $\boldsymbol{k} \perp \boldsymbol{B}$, where $\boldsymbol{k}$ is the wave vector, a resonance occurs when the wave frequency ω is equal to the upper hybrid frequency ω_{uh} given by (Geller, 1996)

$$\omega_{uh} = \sqrt{\omega_{pe}^2 + \omega_{ce}^2}, \tag{2.7}$$

where $\omega_{pe} = \sqrt{e^2 n_e / \epsilon_0 m_e}$ is the electron plasma frequency, and $\omega_{ce} = eB/m_e$ is the electron cyclotron frequency. If the plasma density goes to zero, ω_{pe} goes to zero, causing $\omega_{uh} = \omega_{ce}$. If the magnetic field goes to zero, ω_{ce} goes to zero, and plasma oscillation given by ω_{pe} is recovered. The upper hybrid resonance occurs when the X-mode is launched into the system. External X-mode with $\boldsymbol{E} \perp \boldsymbol{k}$ and $\boldsymbol{E} \perp \boldsymbol{B}$ develops an $\boldsymbol{E}$-component along $\boldsymbol{k}$ when passing through a plasma and thus becomes gradually elliptically polarized.

For propagation along the magnetic field, $\boldsymbol{k} \parallel \boldsymbol{B}$, a resonance occurs when the R-mode wave frequency, ω, is equal to the electron cyclotron frequency, ω_{ec}. For a wave with frequency 2.45 GHz the resonance occurs at the position where the magnetic field amplitude is 875 Gauss.

It is important to recall that R and X modes are automatically formed inside a vacuum chamber containing a magnetized plasma, whatever electromagnetic waves are launched from the outside (Geller, 1996, Ch. 2). Thus, the heating of a magnetized plasma by microwaves is due to both the UHR and the ECR, so the name ECR-plasma sources is a "well-established misnomer" (Roth, 1995, Ch. 13).

Power transfer by the R-mode

In our experiment the external waves propagate mainly parallel to the magnetic field, so the heating process will mainly occur from the R-mode. For simplicity we consider the case where the time-varying electric field $\boldsymbol{E}(t)$ is perpendicular to the static magnetic field $\boldsymbol{B}$ and the wave propagates along $\boldsymbol{B}$. We assume that the electric field is in the xy-plane and the magnetic field is in the z-direction. On that account the heating mechanism from UHR is neglected, and only the ECR heating is explained in this section.

Due to the Lorenz force the charged particles will gyrate along the magnetic field lines with the cyclotron frequency given by $\omega_c = eB/m$. The radius of the gyration, the Larmor radius, is then $r_L = v_\perp/\omega_c$, where $v_\perp$ is the particle velocity perpendicular to the magnetic field. The electrons gyrate with frequency, ω_{ce}, in the direction following the right hand rule, while the positive ions with frequency ω_{ci} rotates in the direction according to the left hand rule.

The time-varying electric field is a linearly polarized microwave field which can be decomposed into the sum of two circular polarized waves rotating in the opposite direction of each other, namely the R-mode and L-mode.

The complex wave-vector can be written in the form

$$\boldsymbol{E} = (\hat{\boldsymbol{x}} - j\hat{\boldsymbol{y}})E_r + (\hat{\boldsymbol{x}} + j\hat{\boldsymbol{y}})E_l, \tag{2.8}$$

where $\hat{\boldsymbol{x}}$ and $\hat{\boldsymbol{y}}$ is the unit vectors, and E_r and E_l are the complex fields

$$E_r = E_{r0}e^{j\omega t}, \quad E_r = E_{r0}e^{j\omega t} \tag{2.9}$$

corresponding to the right- and left-polarized real wave-vectors

$$\begin{aligned}\boldsymbol{E}_r &= E_{r0}(\hat{\boldsymbol{x}}\cos\omega t + \hat{\boldsymbol{y}}\sin\omega t)\\ &= \frac{1}{2}\hat{\boldsymbol{x}}(E_r + E_r^*) - \frac{1}{2}\hat{\boldsymbol{y}}j(E_r - E_r^*)\\ &= \mathrm{Re}[E_r(\hat{\boldsymbol{x}} - j\hat{\boldsymbol{y}}],\end{aligned} \tag{2.10}$$

$$\begin{aligned}\boldsymbol{E}_l &= E_{l0}(\hat{\boldsymbol{x}}\cos\omega t - \hat{\boldsymbol{y}}\sin\omega t)\\ &= \frac{1}{2}\hat{\boldsymbol{x}}(E_l + E_l^*) + \frac{1}{2}\hat{\boldsymbol{y}}j(E_l - E_l^*)\\ &= \mathrm{Re}[E_l(\hat{\boldsymbol{x}} + j\hat{\boldsymbol{y}}].\end{aligned} \tag{2.11}$$

This means that $E_r(\hat{\boldsymbol{x}} - j\hat{\boldsymbol{y}})$ represent the complex R-mode wave-vector and $E_l(\hat{\boldsymbol{x}} + j\hat{\boldsymbol{y}})$ represent the complex L-mode wave-vector.

The equation of motion in the presence of the magnetic field is given by equation 2.1 when adding a term, $-e\boldsymbol{v}\times\boldsymbol{B}$, due to the magnetic field force. The linearized equations are then

$$j\omega v_x = -\frac{e}{m_e}(E_r + E_l) - \frac{eB}{m_e}v_y - \nu_c v_x \tag{2.12}$$

$$j\omega v_y = -\frac{e}{m_e}(-jE_r + jE_l) + \frac{eB}{m_e}v_x - \nu_c v_y \tag{2.13}$$

Again the absorbed power per unit time for one electron is found by averaging:

$$\theta_A = \frac{-e}{2}\mathrm{Re}\langle\boldsymbol{E}\cdot\boldsymbol{v}\rangle = \frac{-e}{2}\mathrm{Re}\langle(E_r + E_l)v_x^* + (-E_r + E_l)v_y^*\rangle. \tag{2.14}$$

By solving equation 2.12 and 2.13 and inserting the solution for v_x and v_y into the equation above, we obtain after averaging

$$\theta_A = m_e\left(\frac{eE_r}{m_e}\right)^2\frac{\nu_c}{\nu_c^2 + (\omega - \omega_{ce})^2} \tag{2.15}$$

When $\omega_{ce}\to\omega$ we have that $\theta_A = e^2E_r^2/m_e\nu_c$, which goes to infinity in the collisionless limit $\nu_c\to 0$. However this behavior is found only in a homogeneous plasma at "exact" resonance (Lieberman and Lichtenberg, 1994).

When there is a nonuniformity in the magnetic field along the z-axis, we can expand the frequency ω_{ce} near resonance to obtain

$$\omega_{ce}(z') = \omega + \alpha z', \tag{2.16}$$

where $z' = z - z_{res}$ is the distance from the exact resonance point z_{res}, and $\alpha \equiv \frac{d\omega_{ce}}{dz}$ is proportional to the gradient in $B(z)$. To find the power absorbed by one electron passing the resonance zone, equation 2.16 is substituted into equation 2.15, and integrated over the resonance zone:

$$\begin{aligned} \theta_{A,\text{zone}} &= m_e \left(\frac{eE_r}{m_e}\right)^2 \int_{-z_0}^{z_0} \frac{\nu_c}{\nu_c^2 + (\alpha z')^2} dz \\ &= \frac{2e^2 E_r^2}{m_e \alpha} \tan^{-1}\left(\frac{\alpha z_0}{\nu_c}\right), \end{aligned} \tag{2.17}$$

where $2z_0$ is the width of the resonance zone. When $\nu_c \ll |\alpha| z_0$, the trigonometric function approaches the value $\pi/2$. The result given in equation 2.17 shows that the power absorbed by the electrons in the presence of a magnetic field is a collisionless process, and that the right hand polarized wave is the mode responsible for resonance heating. Hence, the L-mode does not contribute to a resonance as listed in Table 2.1. We have shown that when electromagnetic waves are launched into the chamber parallel to the magnetic field ($\boldsymbol{k} \parallel \boldsymbol{B}$), only the R-mode contribute to the ECR-heating. This is assumed to be the main heating process for the conditions in Menja.

The calculation leading to equation 2.17 is valid only if z_0 is small enough for the expansion 2.16 to be valid. This is only true if $|\alpha| z_0/\omega \ll 1$. On the other hand, the integral in 2.17 is independent of ν_c only if z_0 is chosen such that $|\alpha| z_0/\nu_c \gg 1$. Both inequalities are satisfied only if $\nu_c \ll \omega$, hence the absorption is collisionless only for collision frequencies much lower than the wave frequency which equals the electron cyclotron frequency at resonance. The collision frequency for electron neutral collisions is given by (Lieberman and Lichtenberg, 1994)

$$\nu_{en} = K n_g, \tag{2.18}$$

where K is the rate constant, to be defined in section 2.3, and n_g is the neutral gas density which is given by the ideal gas law, $n_g = p/T_g$ where

p is the operating pressure and T_g is the neutral gas temperature. Using the rate constant for ionization given by equation 2.20, and assume that the neutral gas is at room temperature 300 K, the collision frequency for ionization is $2 \cdot 10^4 \mathrm{s}^{-1}$ for a pressure $1 \cdot 10^{-3}$ mbar. Using the rate constant for elastic scattering the frequency is even higher. When the pressure increases to 7 mbar the collision frequency for ionization is in the order of the wave frequency. Thus, the magnetic field has little or no influence on the heating process when the pressure is high, so the ECR heating at 2.45 GHz is not useful above 7 mbar, which is in agreement with the result given in Asmussen (1989).

2.3 Calculation of plasma parameters

In a noble gas, the molecular inelastic collision processes such as dissociation, attachment, and rotational and vibrational excitations which greatly complicate the understanding of discharge behavior, are absent (Asmussen *et al.*, 1997). Thus, argon gas is usually chosen as the "test" gas for characterization of ECR discharges. The electron temperature T_e, the plasma potential V_p, and the plasma density n_0 are, as discussed in section 2.1, some of the most important parameters for plasma processing applications. To estimate these parameters and their variations with power, pressure, and source geometry, some assumption are made. We consider a Maxwellian electron energy distribution with the related temperature, T_e, and assume that electron collision rates are uniform throughout the discharge volume. Electron-ion recombination is absent in the discharge volume and occurs only on the discharge walls.

Determination of electron temperature

We assume that the ions are created in the discharge volume by ionization and lost by diffusion to the wall only, i.e. we neglect the ion-electron recom-

bination in the volume. The ion conservation equation then becomes

$$A_l\Gamma_l + A_r\Gamma_r = V\mathcal{R}. \tag{2.19}$$

The left side is the axial and radial ion loss to the wall where A_l and A_r are the areas of the axial-end-wall and the radial-side-wall, respectively. The ion fluxes are given by Γ_l and Γ_r. The right side gives the ion production in the volume V with a reaction rate for ionization, $\mathcal{R} = K_{iz}n_g n_0$, where K_{iz} is the rate constant for ionization given by Lieberman and Lichtenberg (1994):

$$K_{iz}(T_e) \approx K_{iz0}\exp\left(-\frac{\varepsilon_{iz}}{T_e}\right). \tag{2.20}$$

Here ε_{iz} is the threshold ionization energy and the pre-exponential factor for argon is $K_{iz0} \approx 5\cdot 10^{-14}\mathrm{m^3s^{-1}}$. Thus, the ion conservation equation 2.19 can be written

$$n_0 C_s(2\pi R^2 h_l + 2\pi R l h_R) = \pi R^2 l K_{iz} n_g n_0. \tag{2.21}$$

It is shown in chapter 3.1, equation 3.12, that the ion velocity at the sheath edge is equal to the ion acoustic velocity $C_s = (T_e/m_i)^{1/2}$. Using equation 2.23 equation 2.21 can be written as (Lieberman and Lichtenberg, 1994)

$$\frac{K_{iz}(T_e)}{C_s(T_e)} = \frac{1}{n_g d_{\mathrm{eff}}}. \tag{2.22}$$

A characteristic discharge length, d_{eff}, for a cylindrical microwave source is given by Lieberman and Lichtenberg (1994)

$$d_{\mathrm{eff}} = \frac{1}{2}\frac{Rl}{Rh_l + lh_r} \tag{2.23}$$

where R and l are the radius and length of the discharge volume, see Figure 2.1(a), and h_r and h_l are the edge-to-center density ratios in the r and z direction,respectively. These edge-to-center density ratios are estimated and the result is given as (Lieberman and Lichtenberg, 1994)

$$\begin{aligned} h_l &= \frac{n_{sl}}{n_0} \approx 0.86\left(3 + \frac{l}{2\lambda_i}\right)^{-\frac{1}{2}} \\ h_r &= \frac{n_{sr}}{n_0} \approx 0.80\left(4 + \frac{R}{\lambda_i}\right)^{-\frac{1}{2}}, \end{aligned} \tag{2.24}$$

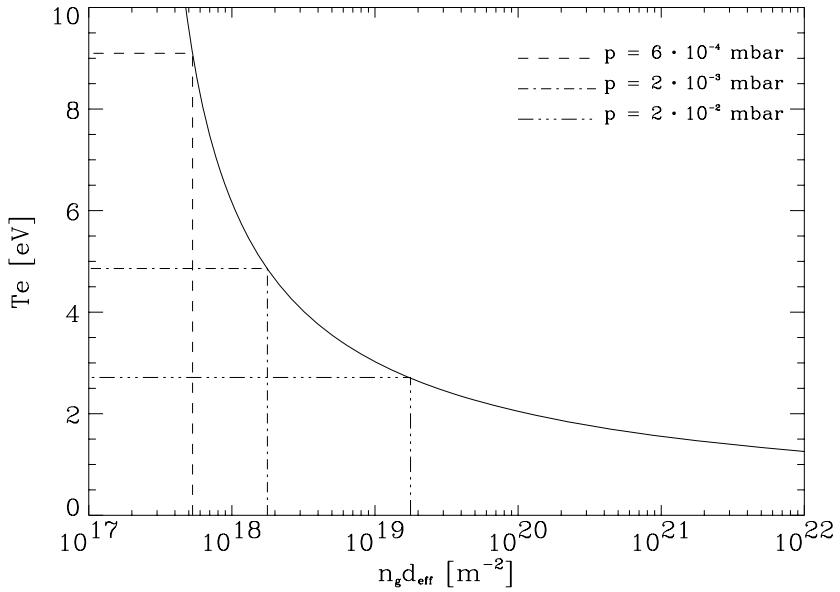

Figure 2.2: T_e versus $n_g d_{\text{eff}}$ for Maxwellian electrons in argon. d_{eff} is calculated for the parameters in Menja, and the dashed lines shows the temperature results for some typical operating pressures.

where n_{sl} and n_{sr} are the axial and radial sheath edge densities, respectively (definition of sheath and sheath edge are given in chapter 3.1).And n_0 is the bulk plasma density. λ_i is the ion mean free path given by $\lambda_i \approx 1/n_g\sigma_i \approx 1/330p$ (cm), where σ_i is the ion collision cross section, n_g the neutral gas density and p is the neutral gas pressure given in Torr.

Both K_{iz}, given by equation 2.20, and C_s are functions of electron temperature, as indicated. Thus, by solving equation 2.22 we obtain the curve shown in Figure 2.2, where T_e versus $n_g d_{\text{eff}}$ is plotted. According to equation 2.23 and 2.24 the characteristic discharge length, d_{eff}, depends on the reactor dimensions, R and l, and the operating pressure, p. Thus, given the dimensions of the discharge chamber of Menja, we can obtain the expected electron temperatures for the typical operation pressures. As shown in Figure 2.2, T_e is calculated for different pressures, obtaining an expected temperature ranging from 3 to 9 eV in Menja. It is also evident from the figure that when lowering

the pressure the electron temperature increases.

Note that the electron temperature is determined by particle conservation only, and is independent of the plasma density and therefore also independent of the input microwave power. Hence, T_e is mainly determined by the discharge geometry and operating pressure.

Determination of plasma density

A steady-state microwave plasma is characterized by the balance between the electromagnetic power absorbed by the plasma electrons, P_{abs}, and the power loss in the plasma volume, expressed as (Asmussen, 1989)

$$P_{\text{abs}} = P_{\text{loss}} \tag{2.25}$$

As treated in section 2.2 the efficient microwave coupling in the divergent ECR-plasma source leads to negligible microwave circuit loss and the coupling efficiency is $> 95\%$ (Stevens *et al.*, 1991). Thus, we can assume that all the incident microwave power P_{w} is absorbed by the electrons so that $P_{\text{abs}} \approx P_{\text{w}}$.

To determine the power loss P_{loss} in the plasma volume, we must consider the energy loss mechanisms. An important quantity is the collisional energy loss, ε_c, per electron-ion pair created in the system, which is defined as (Lieberman and Gottscho, 1994)

$$K_{iz}\varepsilon_c = K_{iz}\varepsilon_{iz} + K_{ex}\varepsilon_{ex} + K_{el}\frac{3m_e}{m_i}T_e, \tag{2.26}$$

where ε_{iz}, ε_{ex} and $\varepsilon_{el} \approx \frac{3m_e}{m_i}T_e$ are the energies lost by an electron as a result of ionization, excitation and elastic scattering against neutral particles, respectively. K_{iz}, K_{ex} and K_{el} are the rate constants for these reactions, where K_{iz} is given by equation 2.20, $K_{ex} \approx K_{ex0}\exp(-\varepsilon_{ex}/T_e)$ with $K_{ex0} \approx 3/4K_{iz0}$, and for the elastic scattering we approximate $K_{el} \approx K_{el0} \approx 10^{-13}\text{m}^3\text{s}^{-1}$. The threshold energies for ionization and excitation of argon are $\varepsilon_{iz} = 15.8$ eV and $\varepsilon_{ex} = 11.62$ eV, respectively (Nordling and Östermann, 1982, Physics Handbook)

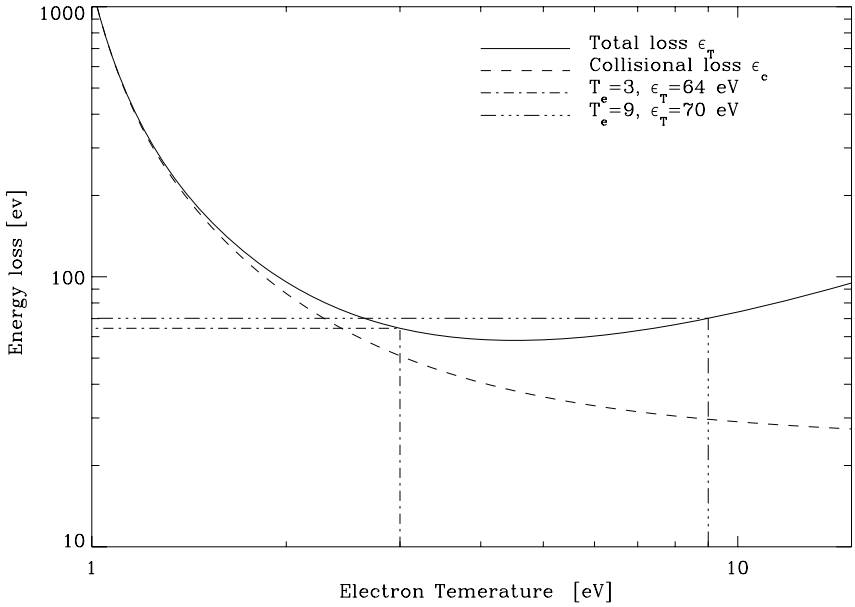

Figure 2.3: ε_T and ε_c versus T_e for Maxwellian electrons in argon. The solid line is the total energy loss per ion lost in the discharge given by equation 2.28. The dashed line is the collisional energy loss given by equation 2.26. The dash-dotted lines indicate the energy loss for the temperature range expected in Menja.

The energy ε_c is lost when the electron-ion pair created is lost. In a monoatomic low-pressure plasma, such as argon plasma, the dominant loss mechanism is the flow of particles to the walls. This loss rate, K_{loss}, in steady state must be balanced by the rate of formation, i.e. the ionization rate $K_{iz} = K_{\text{loss}}$, which is the cause of the factor K_{iz} on the left hand side of equation 2.26 (Lieberman and Gottscho, 1994).

In addition to the collision loss, there is also kinetic energy lost due to the loss of electrons and ions carrying this energy. Maxwellian electrons have a mean kinetic energy of $\varepsilon_e = 2T_e$ (Lieberman and Lichtenberg, 1994). The mean kinetic ion energy lost to the wall origins from the energy obtained in the bulk plasma and in the sheath. The ions have a velocity C_s when reaching the sheath edge so that $\varepsilon_{i0} = \frac{1}{2}m_i C_s^2 = \frac{1}{2}T_e$. Since the vacuum chamber in Menja is grounded a sheath is formed close to the wall with a

potential difference between the bulk plasma and the wall equal to the plasma potential V_p (chapter 3). Thus the ions are accelerated by a potential given as $\varepsilon_{is} = eV_p$. V_p is determined from (Gorbatkin and Barry, 1992b)

$$V_p = V_f + \frac{T_e}{2e} \ln\left(\frac{m_i}{2.3m_e}\right), \tag{2.27}$$

where e is the electron charge and V_f is the floating potential given by equation 3.20. For an argon plasma V_p is approximately $\sim 4T_e$ according to equation 2.27. The kinetic ion energy lost to the wall is therefore $\varepsilon_i = \varepsilon_{i0} + \varepsilon_{is} = 4.5T_e$. The total energy loss ε_T per ion lost from the system as a function of T_e is found using equation 2.26i,

$$\varepsilon_T = \varepsilon_{iz} + \frac{3}{4}\varepsilon_{ex} \exp\left(\frac{\varepsilon_{iz} + \varepsilon_{ex}}{T_e}\right) + \frac{3K_{el0}m_e}{K_{iz0}m_i} \exp\left(\frac{\varepsilon_{iz}}{T_e}\right) + 4.5T_e. \tag{2.28}$$

The total power loss in the system is mostly due to particle loss to the walls, hence

$$\begin{aligned} P_{\text{loss}} &= (\Gamma_l A_l + \Gamma_R A_R) e\varepsilon_T \\ &= n_0 C_s e 2\pi R(Rh_l + lh_R)\varepsilon_T \\ &= n_0 C_s e \frac{\pi R^2 l}{d_{\text{eff}}} \varepsilon_T. \end{aligned} \tag{2.29}$$

From equation 2.25 we have that the power lost in the system is equal to the incident microwave power, hence solving equation 2.29 with respect to n_0 gives

$$n_0 = \frac{P_{\text{abs}}}{\pi R^2 l} \frac{d_{\text{eff}}}{C_s e \varepsilon_T}, \tag{2.30}$$

where $P_{\text{abs}}/\pi R^2 l$ can be considered as the average discharge power density (Lieberman and Gottscho, 1994).

The result of ε_T versus T_e from equation 2.28 and ε_c versus T_e from equation 2.26 are plotted in Figure 2.3, for the case of an argon plasma in a grounded vacuum chamber. We can see that for low temperatures the collision loss is the dominating loss mechanism, while for higher temperatures the kinetic energy loss to the wall dominates. If the gas pressure is known, T_e is found from equation 2.22, and the total energy loss ε_T can be found graphically

p [mbar]			$P_{\text{abs}} = 500\text{W}$	$P_{\text{abs}} = 1000\text{W}$
	T_e [eV]	ε_T [eV]	n_0 [m^{-3}]	n_0 [m^{-3}]
$6 \cdot 10^{-4}$	9.1	70.5	$7.3 \cdot 10^{16}$	$1.4 \cdot 10^{17}$
$2 \cdot 10^{-3}$	4.9	58.3	$1.2 \cdot 10^{17}$	$2.4 \cdot 10^{17}$
$2 \cdot 10^{-2}$	2.7	68.8	$1.3 \cdot 10^{17}$	$2.7 \cdot 10^{17}$

Table 2.2: Calculated parameters for an argon plasma in Menja. Three different operating pressures is chosen as listed in the first column. The expected T_e and ε_T for these pressures is calculated using equation 2.22/figure 2.2 and equation 2.28/figure 2.3, respectively. n_0 is calculated from equation 2.30 at two different values of absorbed powers.

from Figure 2.3. If the absorbed power P_{abs} is known, equation 2.30 can be solved to yield the plasma density n_0. Result of this calculation are listed in table 2.2 for some typical operation pressure and microwave power.

Note that the plasma density n_0 is determined by the total power balance in the discharge and is a function of pressure only through the pressure dependence of h_l and h_R (equation 2.24) and the weaker dependence of T_e on p.

Chapter 3

Probe theory

As discussed earlier the interesting plasma parameters produced in Menja are in this thesis the plasma potential V_p, electron and ion density and temperature n_e, n_i, T_e and T_i, respectively. To measure the parameters we insert electrical probes into the plasma. These probes will disturb the local plasma behavior. Thus, the difficulty in measuring the parameters is to understand how the probes perturb the plasma locally and how the local plasma parameters are related to the unperturbed plasma far from the probe (the bulk plasma). In this chapter the perturbing effect is briefly discussed in section 3.1. In section 3.2 we present the theory for the common Langmuir probe theory, which allows us to measure V_p, n_e and T_e. In section 3.3 an ion flux probe is described, from which n_i can be obtained. Section 3.4 deals with the ion energy analyzer (IEA), which is the most complicated electrical probe used in this thesis. The IEA-probe is used to derive the ion energy distribution.

3.1 Sheath formation

In a quasi-neutral plasma consisting of equal numbers of positive ions and electrons, the electrons are far more mobile than the ions. Fast-moving electrons will rapidly be lost to the walls, while the less mobile ions are maintained in the plasma, hence the plasma will charge positively with respect

to the wall. A positive ion sheath forms near the wall in which $n_i \gg n_e$. The net positive charge within the sheath leads to a potential profile that is positive in the plasma and falls sharply to zero near the wall, as shown in Figure 3.1. The electric field within the sheath points from the plasma to the wall, hence electrons are decelerated and the ions are accelerated in this direction, so that the ions and electrons are lost to the walls at the same rate. Hence, the plasma can remain quasi neutrality, $n_e \approx n_i$. A sheath forms close to all material surfaces in the plasma, also near probe surfaces. It will be shown that the sheath thickness is limited so that the perturbing effect from a probe is limited under certain conditions.

The Debye length

When a charge is inserted into the plasma it generates an electric field. The plasma particles tend to redistribute themselves so as to shield the plasma from the perturbing field. The effect of the charge on the plasma may be deduced from Poisson's equation. Doing this we have to assume that the ion density near the charge is equal to the ion density far from the charge, $n_i \approx n_\infty$, and that the electrons are in thermal equilibrium. Hence, the electron density is determined by the Boltzmann factor,

$$n_e = n_\infty \exp\left(\frac{eV}{T_e}\right). \tag{3.1}$$

Here T_e is the electron temperature in Joule, n_∞ is the electron density far from the charge, e is the electron charge and V is the perturbing potential from the charge. The potential V is given by Poisson's equation. Solving this equation in one dimension yields (Hutcinson, 1995):

$$V(x) = \exp\left(\pm\frac{x}{\lambda_D}\right), \tag{3.2}$$

where λ_D is the shielding length, called the Debye length given by

$$\lambda_D = \left(\frac{\epsilon_0 T_e}{e^2 n_\infty}\right)^{\frac{1}{2}}, \tag{3.3}$$

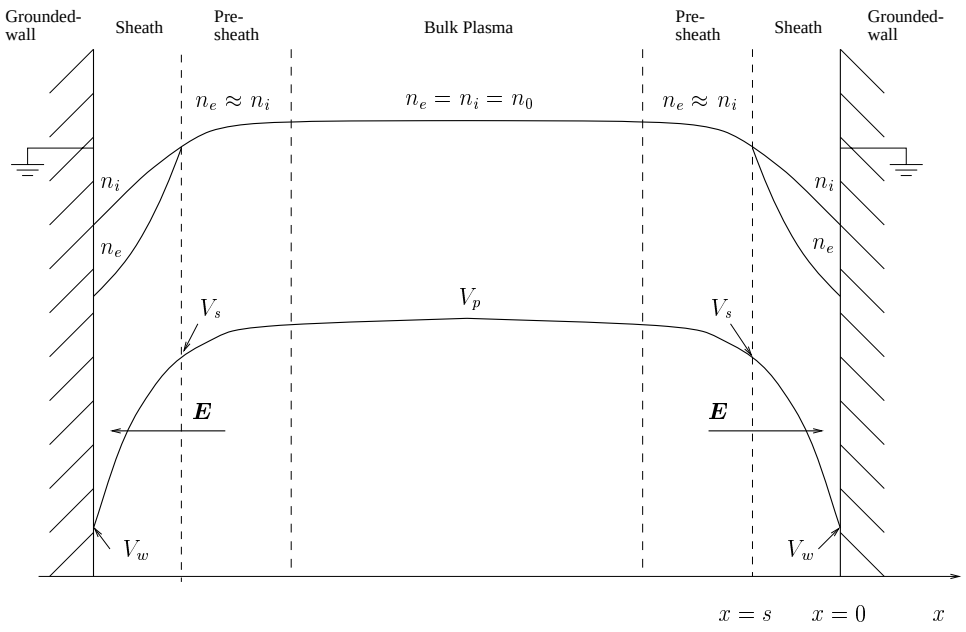

Figure 3.1: Formation of plasma sheaths and pre-sheaths in contact with conducting walls. The qualitative behavior for the electron and ion densities and potential after formation of the sheath is drawn. The direction of the electric field in the sheath is also indicated.

where ϵ_0 is the vacuum permittivity. As shown by equation 3.2 the perturbing effect from a charge in a plasma only penetrate an order of the Debye length into the plasma.

The Bohm sheath criterion and the sheath thickness

We consider a non-magnetized plasma and assume that the plasma is terminated by a perfectly absorbing probe held at a negative potential, V_{pr}. We assume that the probe radius a is much greater than the Debye length $a \gg \lambda_D$. Since the sheath thickness s is typically a few times the Debye length, as will be shown below, we also assume that $a \gg s$. By this restriction it is reasonable to assume a plane probe geometry, and to use a collision-less sheath theory.

Further, we consider a time-independent model for the potential in a planar plasma sheath $V(x)$, as a function of position x. We choose the position of the probe surface to be $x = 0$, as shown in the geometry given in figure 3.1. Far from the probe there is a field-free and neutral plasma, so that $n_i = n_e = n_0$. At position $x = s$, where s is the sheath thickness, there is a transition from the non-neutral sheath to the neutral bulk plasma. When Langmuir and Mott-Smith (1924) introduced the probe theory they assumed that this transition was well-defined by a sheath-edge, i.e. that the whole drop in potential between the ionized gas and the collector is concentrated within this sheath. Later knowledge has shown that the bulk plasma is gradually converted to the sheath in a region called the pre-sheath. The pre-sheath is assumed to be approximately neutral, $n_i \approx n_e$, but is not strictly field free. Throughout this thesis the pre-sheath-sheath interface will be called the sheath edge and the subscript s denotes values at this position. The sheath potential V must satisfy Poisson's equation

$$\nabla^2 V = \frac{-e}{\epsilon_0} \left(n_i - n_e \right) . \tag{3.4}$$

The electrons are assumed to be in thermal equilibrium, so that n_e is given by equation 3.1.

The ion density must be calculated from the equation of motion. The potential is chosen to be zero at the sheath edge, so that $V_s = 0$. The sheath is assumed collisionless and ionization free so the energy conservation can be assumed, giving

$$\frac{1}{2} m_i v_{is}^2 = \frac{1}{2} m_i v_i^2 + eV \tag{3.5}$$

Solving for the ion velocity in the sheath, v_i, we obtain

$$v_i = v_{is} \left(1 - \frac{2eV}{m_i v_{is}^2} \right)^{1/2} . \tag{3.6}$$

The assumption that no ionization occurs in the sheath gives the ion continuity equation $\nabla \cdot (n_i v_i) = 0$. Thus, the particle current density in the sheath and sheath-edge are related as

$$j_{is} = n_{is} v_{is} = j_i = n_i v_i \tag{3.7}$$

Using equation 3.6 and 3.7 we find that the ion density in the sheath is

$$n_i = n_{is}\left(1 - \frac{2eV}{m_i v_{is}^2}\right)^{-1/2}. \tag{3.8}$$

Substituting n_i and n_e into 3.4, the Poisson's equation becomes

$$\frac{d^2V}{dx^2} = \frac{en_s}{\epsilon_0}\left[\exp\left(\frac{eV}{T_e}\right) - \left(1 - \frac{2eV}{m_i v_{is}^2}\right)^{-1/2}\right], \tag{3.9}$$

where $n_s = n_{is} = n_{es}$ is the density at the sheath edge. To solve this equation we use that $V_s = 0$ and that the electric field is zero at the sheath edge so that $\frac{dV}{dx}|_{x=s} = 0$. Multiplying equation 3.9 by $\frac{dV}{dx}$ and integrating we obtain

$$\frac{1}{2}\left(\frac{dV}{dx}\right)^2 = \frac{en_s}{\epsilon_0}\left\{\frac{m_i v_{is}^2}{e}\left[\left(1 - \frac{2eV}{m_i v_{is}^2}\right)^{1/2} - 1\right] + \frac{T_e}{e}\left[\exp\left(\frac{eV}{T_e}\right) - 1\right]\right\} \tag{3.10}$$

If we now consider the area close to the sheath edge, where $|eV| \ll T_e$ and $|eV| \ll \frac{1}{2}m_i v_{is}^2$, the right hand side of equation 3.10 can be simplified by Taylor expansion, yielding:

$$\frac{1}{2}\left(\frac{dV}{dx}\right)^2 = \frac{1}{2}\lambda_D^{-2}V^2\left(1 - \frac{T_e}{m_i v_{is}^2}\right). \tag{3.11}$$

We observe that the right hand side must be positive, which means that

$$v_{is} \geqslant \left(\frac{T_e}{m_i}\right)^{1/2} \equiv C_s \tag{3.12}$$

This inequality is called the Bohm sheath criterion where C_s is the ion acoustic velocity or the Bohm velocity (u_B). The criterion shows the need for a pre-sheath between the bulk plasma and the sheath region where the ions are accelerated up to the required velocity. It was Bohm *et al.* (1949) that first showed that a pre-sheath where needed to accelerate the ions.

Sheath thickness

To calculate the sheath thickness it is convenient to use another reference point for the potential. Let us now define the zero potential in the bulk

plasma so that $V = 0$ there, hence $V_s \neq 0$ in this calculation. We assume that the electron density is negligible in the sheath region so that $n_e = 0$ in equation 3.4. Using the Poisson's equation as before, performing the integrations as we did to obtain equation 3.10, we get

$$\frac{1}{2}\left(\frac{dV}{dx}\right)^2 = \frac{n_s m_i v_{is}^2}{\epsilon_0}\left(1 - \frac{2eV}{m_i v_{is}^2}\right)^{1/2} \tag{3.13}$$

Taking the square root and integrate again we have a relation between the position and the potential in the sheath given as

$$x = \frac{\sqrt{2}}{3}\left(\frac{m_i v_{is}^2 \epsilon_0}{e^2 n_s}\right)^{1/2}\left(\frac{2eV}{m_i v_{is}^2} - 1\right)^{3/4}. \tag{3.14}$$

By using the Bohm criterion found above we assume that the ion velocity at the sheath edge is equal to the ion acoustic speed, $v_{is} = C_s = \sqrt{T_e/m_i}$. Since the reference point for the potential is changed we can assume that the potential at the sheath edge is large, thus assuming that $|eV| \gg \frac{1}{2}m_i v_{is}^2 = T_e/2e$. Using the Debye length given by equation 3.3 the sheath thickness can be expressed as

$$s = \frac{\sqrt{2}}{3}\lambda_D\left(\frac{2eV_s}{T_e}\right)^{3/4}. \tag{3.15}$$

This is also known as the Child law sheath (Lieberman and Lichtenberg, 1994). If we now assume that the electron temperature is $T_e \sim 4$ eV and the sheath potential is $V_s \sim 30$ V, the sheath thickness is of the order of a few Debye lengths, $s \sim 3\lambda_D$. In a dense plasma with $n_e \sim 10^{17}\mathrm{m}^{-3}$, $\lambda_D \sim 0.05$ mm, which result in a sheath thickness of $s \sim 0.1$ mm. Thus, the sheath thickness will be small in extension compared with the dimension of the plasma.

3.2 Langmuir probe

One of the earliest and still most useful tool for diagnosing the plasma is the well known Langmuir probe, introduced by Langmuir in 1924. For a

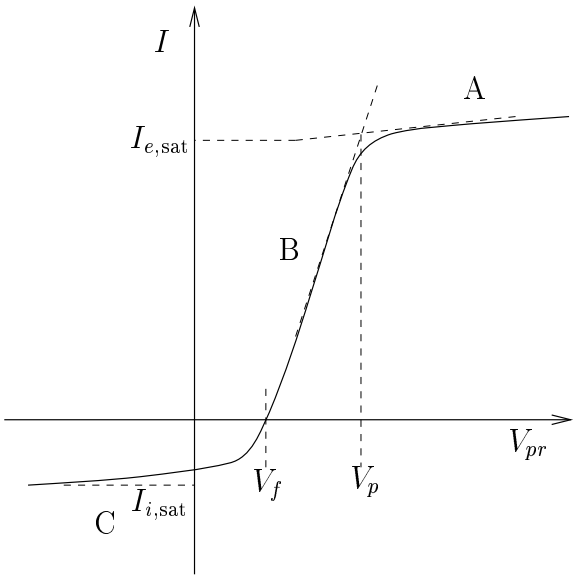

Figure 3.2: A langmuir characteristic

non-magnetized plasma there exist a well-founded theory in agreement with experimental observations (Bohm *et al.*, 1949). The analysis for this probe is well known and described in several works and papers. The first analysis was done by Langmuir and Mott-Smith (1924); other works are by Chen (1965) and Hutcinson (1995). When a magnetic field is introduced less developed theories exist. The "common" analysis theory of the probes in magnetized plasmas have not changed much since the review of Chen (1965). A kinetic theory for small probes in strongly magnetized plasmas is developed by Demidov *et al.* (1999), and there exist fluid-theory for larger probes. The probe theory presented in this works are "complicated" and is beyond the scope of this thesis. The Langmuir theory presented here are taken from the texts of Hutcinson (1995) and Chen (1965). Let us first look at the theory in a non-magnetized plasma, and then discuss briefly the problems which arise when introducing the external magnetic field.

A Langmuir probe consists of a small conductor; in this thesis Langmuir probes are made of thin tungsten wires. The probe bias is swept from negative to large positive values. The bias affects the current to the probe, thus an

ion-voltage characteristic is obtained by changing the bias around the plasma potential as shown in figure 3.2. In our case we sweep the probe from -30 to +30 volts during 30 ms.

If the probe bias is at the plasma potential, V_p (indicated in figure 3.2), no sheath is formed between the probe and the plasma. Thus, assuming that $T_i \lesssim T_e$, the probe current will to a good approximation consist of electrons only at this potential, $I \approx I_e = eA\Gamma_e$, where $\Gamma = \frac{1}{4}n\bar{v}$ is the particle current density. If the voltage is increased above the plasma potential, $V_{pr} > V_p$, the electron current cannot increase any further, since all the electrons are collected at the plasma potential. The ion current, I_i, decreases due to the repulsion of the ions, but this is already much less than the electron current, so the probe current, I, is approximately constant. This region A is known as the electron saturation and here I is equal to the electron saturation current.

In region B the probe potential decreases, $V_{pr} < V_p$, so the probe is negative with respect to the surrounding plasma. An increasing fraction of the electrons are reflected from the negative potential. When the potential is sufficiently negative the electron current will only be a small fraction of the electron saturation value. The current drawn by the probe is zero when the electron and ion current are equal, $I_e = I_i$, at the floating potential, V_f. If the potential is decreased further only ions are collected by the probe, reaching ion saturation, region C.

Analysis of a probe characteristic

Assuming that the electron current density to the probe is given by the Boltzmann factor (eq. 3.1) which gives

$$j_e = \frac{1}{4}n_{es}\bar{v}_e = \frac{1}{4}n_\infty \bar{v}_e \exp\left(\frac{eV_{pr}}{T_e}\right), \tag{3.16}$$

where $\bar{v}_e = 2(2T_e/\pi m_e)^{1/2}$ is the mean Maxwellian electron velocity.

Accelerating the ions up to the ion acoustic velocity requires a potential drop

$$V_{\text{drop}} = -\frac{m_i C_s^2}{2e} = -\frac{T_e}{2e} \tag{3.17}$$

relative to the plasma potential. The ion current density to the probe is then given by the Bohm condition as

$$j_{is} = n_\infty \left(\frac{T_e}{m_i}\right)^{\frac{1}{2}} \exp\left(-\frac{1}{2}\right) \tag{3.18}$$

Equation 3.16 and 3.18 will then give the total current measured by the probe as a function of potential V_{pr} (Hutcinson, 1995)

$$I = n_\infty e A_{pr} \left(\frac{T_e}{m_i}\right)^{\frac{1}{2}} \left[\frac{1}{2}\left(\frac{2m_i}{\pi m_e}\right)^{\frac{1}{2}} \exp\left(\frac{eV_{pr}}{T_e}\right) - \frac{A_s}{A_{pr}} \exp\left(-\frac{1}{2}\right)\right]. \tag{3.19}$$

Here A_s and A_{pr} is the sheath size and the probe size, respectively and V_{pr} is the probe potential. This equation is only valid when $T_i < T_e$, $\lambda_D \ll a$ and $A_s \approx A_{pr}$.

When the probe potential V_{pr} is at the floating potential V_f, no current is collected by the probe, so setting $I = 0$ gives V_f as

$$V_f = \frac{T_e}{2e}\left[\ln\left(\frac{2\pi m_e}{m_i}\right) - 1\right]. \tag{3.20}$$

The problem is usually to find the plasma potential V_p, which is the reference point for voltage in our treatment, and the voltage where electron saturation is reached, see Figure 3.2. To find T_e the slope of the characteristic in region B in Figure 3.2 can be used as follows

$$\frac{dI}{dV_{pr}} = \frac{e}{T_e}\left(I - I_{i,\mathrm{sat}}\right) + \frac{dI_{i,\mathrm{sat}}}{dV_{pr}}, \tag{3.21}$$

where $I_{i,\mathrm{sat}} = -eA_{pr}j_i$ is the ion saturation current. Neglecting the last term in equation 3.21, gives

$$T_e = \frac{e\left(I - I_{si}\right)}{\frac{dI}{dV_{pr}}}. \tag{3.22}$$

Note, that the current I collected by the probe is exponential as given by equation 3.19. Taking the logarithm of $I - I_{i,\mathrm{sat}}$ and differentiating with respect to the potential V_{pr} we obtain

$$\frac{d}{dV_{pr}}\left(\ln\left|I - I_{i,\mathrm{sat}}\right|\right) = \frac{e}{T_e}, \tag{3.23}$$

which shows that T_e can be obtained numerically from the characteristic by fitting a line to $\ln|I - I_{i,\mathrm{sat}}|$ versus V_{pr}.

When T_e is found the plasma density may be determined by solving $I_{i,\mathrm{sat}} = -eA_{pr}j_i$, where j_i is given by 3.18, with respect to the density given

$$n_\infty = -\frac{I_{i,\mathrm{sat}}}{eA_{pr}}\left(\frac{m_i}{T_e}\right)^{\frac{1}{2}}\exp\left(-\frac{1}{2}\right), \tag{3.24}$$

where $I_{i,\mathrm{sat}}$ can be determined from the characteristic shown in Figure 3.2.

Probes in magnetic fields

What is the main difficulties introducing the magnetic field? The magnetic field introduces an anisotropy which makes the problem at least two dimensional. The electron and ion diffusion coefficient parallel and perpendicular to the magnetic field $D_\parallel$ and $D_\perp$, respectively are estimated as (Goldston and Rutherford, 1995)

$$D_\parallel \sim \nu\lambda_{mfp}^2 \qquad D_\perp \sim \nu r_L^2, \tag{3.25}$$

where ν is the electron-neutral or ion-neutral collision frequency, λ_{mfp} is the collision mean free path along the field and $r_L = mv/eB$ is the Larmor radius for the electron or ion. Thus, the effective mean free path across the field is of the order of r_L, so the particles can travel only this far without making a collision. Since the Larmor radius is quite small for electrons even at moderate fields, there is essentially no collisionless theory in such a case (Chen, 1965).

When the probe is large compared to λ_D, it will collect so many electrons that the surrounding area will be drained faster than the electrons diffuse into the area. Hence, the electrons are collected to the probe from regions quite distant along the field, but not far away in the direction normal to the field. The number of electrons collected by the positively biased probe is therefore reduced in the presence of the magnetic field. With these arguments in mind

Bohm *et al.* (1949) claims that the electron current is not of very much use in the probe analysis.

The Larmor radius for positive ions is large compared to the probe radius, consequently the magnetic field can be neglected in the ion saturation region. Chen (1965) claims that only the ion saturation region is unaffected by the magnetic field, and therefore this region should be used in the analysis.

Hutcinson (1995) describes the general effects of a magnetic field, and the conclusion is that in a practical matter we can use a non-magnetized theory with some small modifications. The argument is that ions flowing to the sheath edge have a velocity equal to the ion acoustic velocity as shown above, but in a strong field this sonic flow can occur only along the field not across it. Therefore it can be assumed that the field-free theory can be applied except that the effective collection area is not the total probe area, but the projection of the probe surface in the direction of the magnetic field. This modification is used when the Langmuir characteristics are analyzed with the standard numerical code presently available at the laboratory, used in this thesis. In chapter 6 we will discuss this analysis method, and show that the density measurements are still underestimated to the theory.

3.3 Ion flux probe

Measuring the ion flux is a very easy experiment. An ordinary Langmuir probe can be used, usually a plane probe, which has to be large compared to the Debye length, $a \gg \lambda_D$, so the Bohm theory is valid. Instead of sweeping the probe as for Langmuir characteristics, the probe is held at a constant negative potential. The probe has to be sufficiently negative to collect the ion saturation current and prevent electrons from contributing to the current. The ions hitting the probe have to satisfy the Bohm sheath criterion (section 3.1), so that the ion velocity at the sheath edge is approximately the ion acoustic velocity C_s. As given above the current collected at the probe is

$$I_{pr} \approx I_{i,\mathrm{sat}} = -eA_{pr} j_{i,\mathrm{sat}} = -en_i C_s \tag{3.26}$$

Knowing the electron temperature and the ion mass it is easy to find the ion density in the plasma by solving equation 3.26.

3.4 Ion Energy Analyzer

The ion temperature and the ion energy distribution are important parameters for plasma processing such as deposition and sputtering. Ordinary Langmuir characteristics cannot give information about these parameters. Consequently, development of an electrostatic ion energy analyzer (IEA) is necessary. The analyzer consists of a series of grids which are maintained at various potentials, therefore it is also called a gridded energy analyzer. The number of grids in the analyzer varies from one to five depending on the plasma conditions, given by density and particle energies. The grids separate the electron and ion components, so that all the electrons are cut off and ions with sufficient energy will be collected, this is illustrated in a simplified version in Figure 3.3. The collector current will then be a function of the sweep voltage on the ion discriminator grid. Hence, also in this case an IV-characteristic is obtained. By analyzing this characteristic the ion energy distribution parallel to the magnetic field are derived as well as the ion temperature.

Design of IEA

There are a lot of considerations to make in designing an analyzer. The IEA for Menja was developed using the work of Podgornyi (1971) and the articles Böhm and Perrin (1993), Junck and Getty (1994), Guo *et al.* (1996) and Pitts (1996). The outline of the IEA is shown in Figure 3.4. The probe consist essentially of a front-plate, 3 metal grids and a collector, as shown in the figure.

If the plasma is able to flow into the probe the particle bombardment on the grids will increase and lead to perturbation of the grid bias potential,

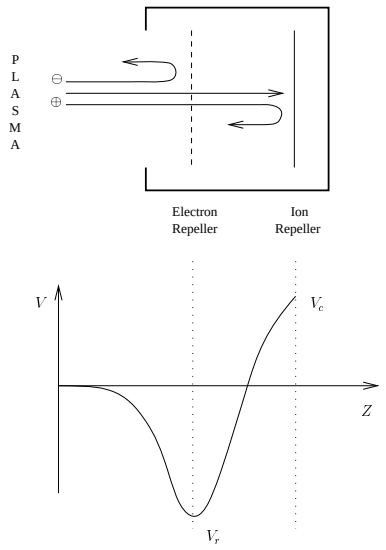

Figure 3.3: Simplified illustration of the operation of an ion energy analyzer, after Hutcinson (1995).

consequently the control of the applied bias is lost. This effect is called space charge effect, and it can destroy the measurements. When energetic ions and electrons are entering the probe they will strike the surface of the grids and collector and sputter electrons from the impact surfaces. These electrons are called secondary electrons and will cause strange effects in the analysis. Space-charge and secondary-electron effects are discussed in chapter 6. The main problem for the IEA measurements and design is to avoid space charges within the probe, and eliminate the effect of secondary electrons.

Front-plate entrance

One of the first design considerations for the IEA is the entrance aperture in the front-plate (Guo *et al.*, 1996). The aperture will perturb the sheath in front of the plate more or less depending on the size of the entrance hole. If the opening is 'too big' the sheath will no longer be planar, and the orbits for the incoming particles are perturbed and lead to a defocusing of the particle flux. The aperture diameter is recommended to be less than the

sheath thickness and of an order of $1 \sim 2\lambda_D$ to avoid this defocusing (Guo *et al.*, 1996), which correspond to a opening of $0.05 \sim 0.1$ mm for the plasma parameters expected in Menja. It is obvious that for practical reasons we have to look for alternatives. The entrance aperture in the IEA is made as small as possible (0.8 mm) with a fine metal mesh, with 60 lines/cm, covering the entrance (design adopted from Junck and Getty (1994)). If the entrance mesh is removed, the plasma will flow into the analyzer and destroy the measurements.

Grid transparency

To further reduce the plasma density inside the probe high-transparency brass grids are selected. The grids have 60 lines per cm and the wire diameter is 0.06 mm. The total geometric transmission for the grid is given by Guo *et al.* (1996)

$$\delta_T = \frac{l - d}{l^2} = 69\%, \tag{3.27}$$

where l is the line spacing and d is the wire diameter. The front-plate and the three grids decrease the plasma density in front of the collector to 23% of the density outside the probe, thus the transmission factor for the IEA is 0.23. This probe transparency reduces the problem of space charges.

Grid bias

In the papers used to design the IEA two or three grids are used in addition to the front-plate and the collector. The electrode bias configuration is chosen differently in the different works, but the theory and the argumentation are similar. The bias configuration used in the experiments in Menja is shown in Figure 3.5, which is mostly adopted from Böhm and Perrin (1993) and adjusted during the experiment to obtain a smooth characteristic with no space charge and secondary electron effects.

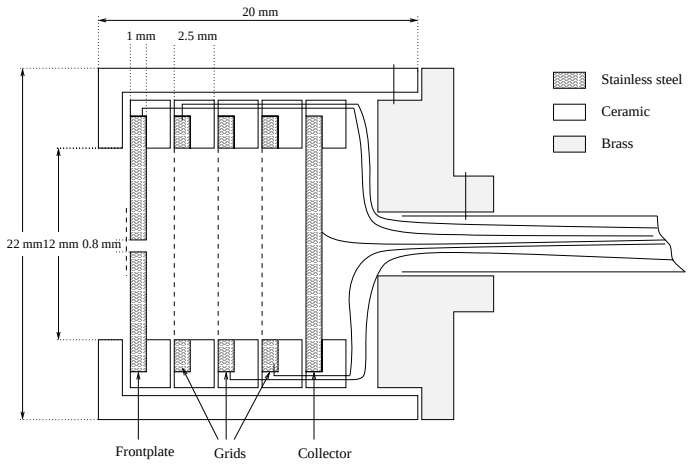

Figure 3.4: The ion energy analyzer designed for use in Menja. The sketch is drawn in scale, showing the cross section parallel to the magnetic field.

The analyzers with two grids apply a constant negative bias to the front-plate, while the analyzers with three grids have the front-plate grounded. Pitts conclude that if an electron grid is included, the front-plate may be left floating, in which case the least perturbation is exercised on the particle flux from the plasma. For the IEA designed in this thesis an electron grid is included and experiments in Menja show that a grounded front-plate is the best choice.

The electron grid, G1, see Figure 3.5, is biased slightly negative to repel most of the electrons entering from the plasma. Unfortunately the contact to G1 was lost during experiment, and the grid was left floating, which also gave good results.

The ion discriminator grid, G2, is swept from 0 to +60 volts. Only the ions with parallel energy greater than the applied voltage will pass through G2, and ions with lower energies will be reflected.

A constant negative bias is also applied to the third grid, G3. If some energetic electrons are able to pass through the first potential barrier from F and G1, they will be repelled at this grid. We also made sure that the third grid potential is lower than the collector potential, so that secondary electrons

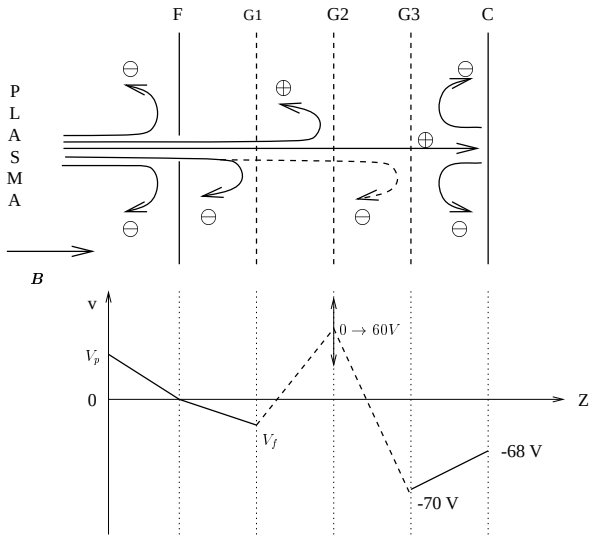

Figure 3.5: Potential distribution configuration

released from the collector by ion impact will be returned to the collector, as indicated in Figure 3.5.

The ions passing the ion grid will be accelerated towards the collector due to G3 and the collector voltage, in which case we make sure that all the ions passing G2 hit the collector and contribute to the collector current, I_c.

Other design considerations

The IEA is constructed to measure the ion velocity distribution parallel to the magnetic field, and so it requires that the parallel velocity component exceeds the perpendicular velocity, $v_{\parallel,i} \gg v_{\perp,i}$. If $v_{\perp,i}$ is too large, the ions will hit the wall of the IEA and not the collector. To avoid this loss which reduces the number of ions hitting the collector we could;

i. Decrease the length of the IEA; Which means that the distance between the grids is decreased. The drawback is that the chance of arcing increase and the voltages biased on each grid can affect each other.

ii. Increase the diameter of the probe; Which may cause a deformity of the grid so that it curves in stead of remaining flat, which may lead to a defocusing of the particle trajectories.

The structure and the dimensions of the IEA were chosen by comparing the analyzers used in the referred papers. The final decisions were made in the laboratory when the existing equipments and materials were evaluated. The resulting dimension and design are shown in Figure 3.4. The front-plate is of stainless steel with the entrance pin hole made as small as possible with diameter 0.8 mm, and a brass grid spot welded to cover the hole. The three brass grids are spot welded on thin stainless steel rings with an outer diameter of 16 mm and inner diameter of 12 mm. The collector is equal to the front-plate without the hole. All the plates and rings are made as thin as possible with a thickness of 1 mm. Ceramic discs separate the grids and the coaxial cables as shown in Figure 3.4, which results in a grid spacing of 2.5 mm. The ceramic house has a outer diameter of 22 mm and length 20 mm.

Derivation of the ion velocity distribution

As described above the collector current I_c is measured as a function of the retarding grid potential V_g applied to the ion discriminator grid. All the ions arriving at the front-plate with an energy greater than eV_g will contribute to the ion current I_c at the collector. Consequently, when sweeping the grid voltage V_g, an IV-characteristic is obtained as shown in Figure 3.6. We will deduce a relationship between the IV-characteristic and the ion velocity distribution $f(v)$, in order to find this distribution and the corresponding temperature.

The ion velocity distribution in a time independent plasma is in general a six-dimensional distribution in phase space, $f(\boldsymbol{r}, \boldsymbol{v})$, where $\boldsymbol{r} = (r_x, r_y, r_z)$ and $\boldsymbol{v} = (v_x, v_y, v_z)$ is the space and velocity vectors, respectively. The particles in our experiment are influenced by a magnetic field with direction parallel to the z-axis. Hence, assuming that $v_z \gg v_x, v_y$ the distribution function

$f(\boldsymbol{v}, \boldsymbol{r})$ is in each point reduced to a one-dimensional velocity distribution $f(v_z)$. For simplicity the v_z-component of the velocity is denoted v. The distribution function $f(v)$ is related to the total particle density n and the particle flux nv, in the positive direction where $v > 0$ by (Goldston and Rutherford, 1995)

$$n = \int_0^\infty f(v)dv \tag{3.28}$$

$$nv = \int_0^\infty vf(v)dv \tag{3.29}$$

The current I_c measured by the analyzer is equal to the ion flux passing the discriminator grid times the ion charge. Since the ions need a minimum velocity v_0 to exceed the voltage barrier the integral should go from v_0 in stead of 0 in equation 3.29. Hence, the current can be written as (Charles *et al.*, 1992)

$$I_c(v_0) = Ae \int_{v_0}^\infty vf(v)dv, \tag{3.30}$$

A is a constant depending on the front-plate aperture and the analyzers transmission factor. The minimum velocity v_0 is given by the relation between energy and grid potential,

$$E_i = \frac{1}{2}m_i v_0^2 = eV_g, \tag{3.31}$$

where E_i and m_i is the ion energy and mass, respectively. Hence, the minimum velocity is $v_0 = \sqrt{2eV_g/m_i}$. To find the relation between I_c, V_g and $f(v)$ a transformation from velocity distribution to energy distribution is necessary. From equation 3.31 we obtain $dE = m_i v dv$, hence equation 3.30 becomes

$$I_c(eV_g) = A\frac{e}{m_i} \int_{eV_g}^\infty f\left(\sqrt{\frac{2\xi}{m_i}}\right) d\xi, \tag{3.32}$$

ξ is the integration variable for the energy and $eV_g = E$.

Solving equation 3.32 shows that the ion distribution function is proportional to the differential of the measured ion current with respect to the grid potential (Böhm and Perrin, 1993)

$$f(v) = -A\frac{m_i}{e^2}\frac{dI_c(V_g)}{dV_g} \tag{3.33}$$

As mentioned above, the flux of the ions with enough parallel energy to overcome the electric field from the ion grid is recorded by the collector. The ions from the bulk plasma experience a kinetic energy gain when they fall through the sheath and pre-sheath. This energy gain is due to the potential difference between the plasma and the grounded front-plate (Podgornyi, 1971). The ions with velocity v at the sheath edge will enter the front-plate with a velocity $v_F = v + v_{sps}$, where v_{sps} is the velocity gained in the sheath and pre-sheath given by

$$v_{sps} = \sqrt{\frac{2eV_{sps}}{m_i}}, \tag{3.34}$$

where V_{sps} is the sum of the sheath and pre-sheath potential. The front-plate is grounded so that the sheath potential is equal to the plasma potential, $V_{sps} \approx V_p$. Consequently, the ions have a minimum velocity equal to v_{sps}, and the current I_c will be constant until $V_g > V_p$. Then, as the retarding potential increases, the magnitude of the measured ion current decreases. Looking at the IV-characteristic shown in Figure 3.6, we see that;

i. The plasma potential is obtained where the characteristic start to decrease (Charles *et al.*, 1992).

ii. The characteristic is numerically differentiated, and the resulting distribution is plotted in Figure 3.6.

iii. This distribution is the ion velocity distribution at the collector (equation 3.33), which is shifted in velocity space by v_{sps} compared to the velocity distribution in the plasma.

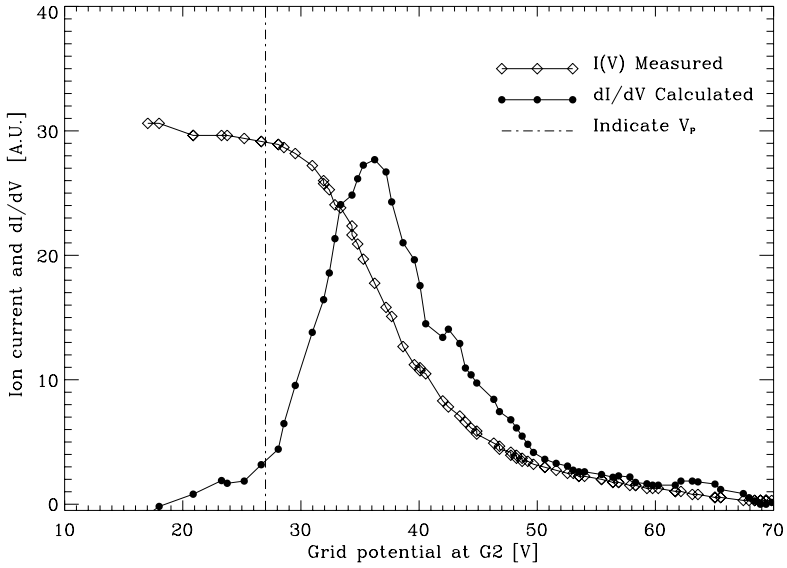

Figure 3.6: The IV-characteristic obtained by an IEA-measurement in Menja, and the corresponding distribution. The dash-dotted line indicate the plasma potential

To find the ion distribution in the bulk plasma, we take the difference between the plasma potential derived from the characteristic and the retarding potential $V' = V_g - V_p$, and plot the distribution with respect to V'. But from the plasma processing point of view the most interesting distribution is the one at the collector, since this will in principle give a "precise" control of the energy of the ions striking the substrate surface.

For a Maxwellian beam velocity distribution we have (Stenzel *et al.*, 1982)

$$f(v) = \exp\left(-\frac{m_i(v - v_b)^2}{2kT_i}\right), \tag{3.35}$$

where $v_b = v_b' + v_{sps}$ is the ion beam velocity at the collector, and v_b' is the ion beam velocity in the bulk plasma. The half-width Δv_b at the $1/e$ point defines the ion temperature T_i. The obtained distribution function is therefore fitted with a Gaussian function given by

$$\mathrm{Yfit}(v) = A_0 \exp\left(-\frac{(v - A_1)^2}{2A_2^2}\right), \tag{3.36}$$

where the numerical solution gives array A. Here A_2 gives the ion temperature, A_1 gives the ion beam velocity and A_0 is the normalization constant. This Gaussian fitting procedure is applied to the distribution function obtained by the IEA, and the resulting ion temperature are shown in section 5.3.

Chapter 4

Design of Menja

The design and operation of an Electron Cyclotron Resonance (ECR) plasma source must satisfy three main objectives (Ferreira *et al.*, 1992):

i. Filling the discharge tube with gas of required composition, pressure and flow rate;

ii. Providing the required electromagnetic field distribution and intensity to initiate and sustain a discharge;

iii. Ensuring an efficient power transfer from the microwave feed line to the plasma.

Menja is an ECR-plasma source designed with these considerations in mind, and with the purpose of applying it for thin film deposition. The source is assembled mostly by parts collected from other "antiquated" experiments, so that the size and geometry etc. of the objects have not been optimized for the purpose. Hence, most of the effort in the design considerations has been to assemble the parts to obtain the best result possible, and to design some new parts that had to be manufactured. The main layout of Menja is shown in Figure 4.1. The microwave power is injected along the magnetic field lines into a cylindrical vacuum chamber, via a dielectric vacuum window. Nine

magnetic field coils surrounding the chamber generate a diverging magnetic field. The current in the coils is chosen to achieve the ECR conditions, permitting effective wave absorption and ionization when the low-pressure gas is introduced. The plasma thus created at the resonance surface flows further into the chamber along the diverging magnetic field lines. The following sections describe each part of the source and their assistance to obtain an effective plasma source for film deposition.

4.1 Vacuum chamber

The plasma chamber is a stainless steel cylindrical ultra-high vacuum chamber. The chamber has three different diameters and therefore it is natural to divide it into three parts, which are called the plasma-production part or the neck, the expansion part and the process part. This division is done to make it easier to refer to the different parts of the chamber, it does not refer to sharp distinction between different regimes of plasma parameters.

The plasma-production takes place in the neck. The size of this part is 10 cm in diameter and 15 cm long. As we can see from Figure 4.1 and 4.2 this part is quite narrow compared to the rest of the chamber. The neck has a 100 cf port[1] which is connected to a microwave-introduction-window where microwave power is feed into the chamber, (see section 4.3). Argon is introduced into the chamber in the neck about one centimeter from the vacuum window.

The expansion region is in the central part of the chamber. After the plasma is produced in the neck it will flow into the chamber along the magnetic field lines. Here it expands due to the diverging magnetic field lines and the plasma volume will increase. Section 4.4 explains this in more detail. This part has a radius of 16 cm and a length of about 30 cm and one 35 cf port provides radial access to the plasma.

[1] 100 mm inner diameter con-flat flange

Figure 4.1: A design drawing of the ECR plasma source, Menja. Microwave power generated at the magnetron (1) is fed into the vacuum chamber via a vacuum window (2). The external magnetic field produced by nine coils (8 and 9) generates a EC-resonance in the neck (3) at the frequency of the incoming waves. The plasma thus created in the neck flows along the magnetic field lines to the expansion (4) and the process (5) parts. Axial and radial diagnostic equipment are inserted through ports 6 and 7.

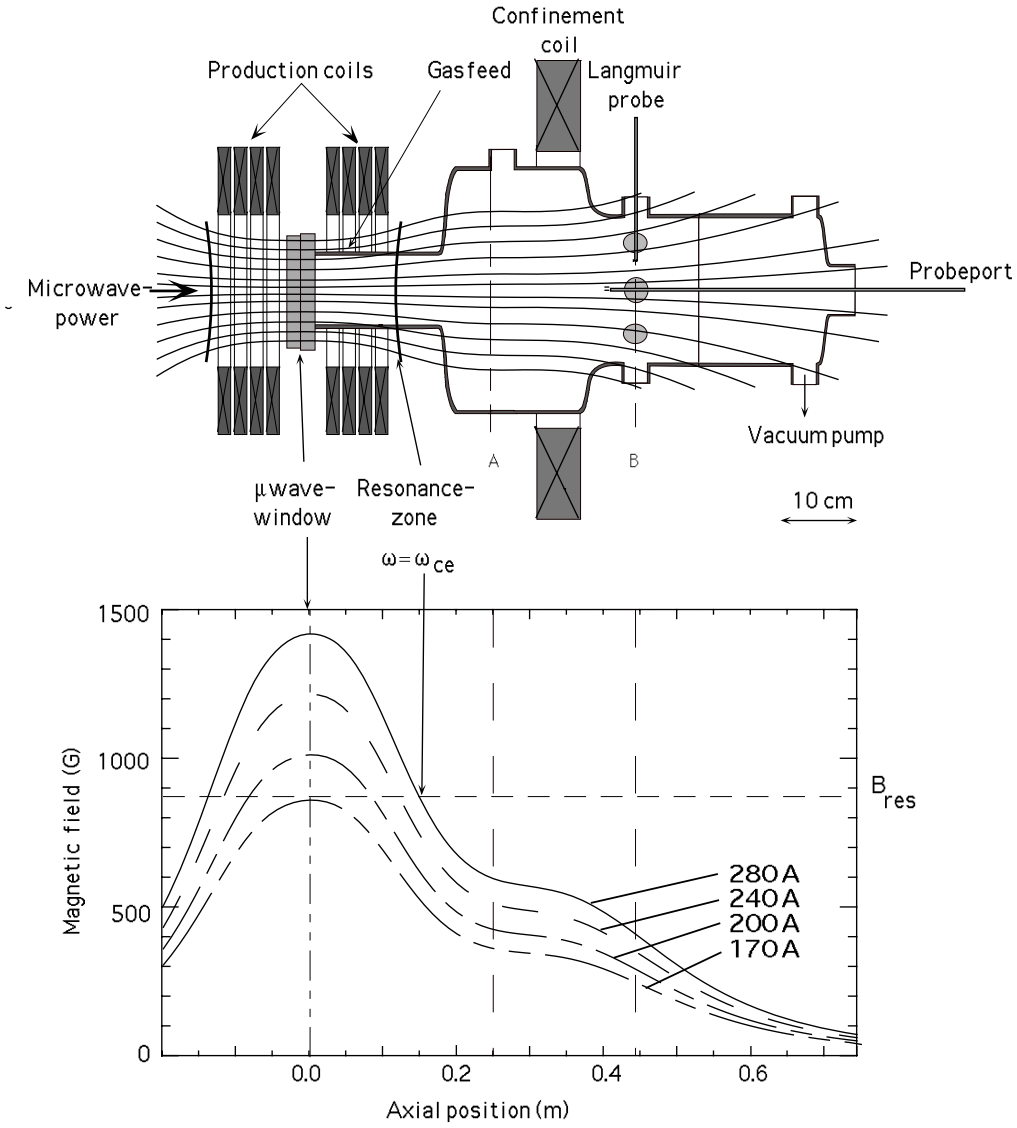

Figure 4.2: The ECR device with magnetic field configuration. a) The vacuum chamber, the production and confinement coil arrangement. The magnetic field lines from a coil-current of 240 A are plotted showing that the resonance zone is located in the neck. b) The magnetic field strength along the axis of the chamber for four different coil-currents. The horizontal line is the resonance value of 875 G, and the vertical line is the position of the vacuum window.

After the plasma expands it flows further along the field lines into the process part. This volume has a radius of 11 cm and is about 30 cm long. The process part has twelve 35 cf ports giving radial access for diagnostics, and one 63 cf end-port. The end-port gives the only axial diagnostic access to the plasma. The pumps and the penning gauge head are connected to the ports at the end (see Figure 4.1).

4.2 Vacuum system

The vacuum system in Menja can be divided into five parts; chamber, pumps, valves, pressure gauges and control system. The vacuum chamber is already described in section 4.1. The pumping system consist of a turbo molecular pump and a rotary van vacuum pump. The turbo molecular pump, a TURBOVAC 50, is connected to the chamber via a high vacuum 100 mm conflat flange/pipe to one of the 35 cf ports at the downstream end of the process chamber. In the documentation for the TURBOVAC a connection pipe length of more than 100 mm is not recommended, because this will reduce the pumping speed, it is also recommended to connect the pump to a 63 cf port, but this was not available. In setting up a vacuum system one of the most important considerations is the choice of connections between the pump and the vessel, to keep pumping losses to a minimum. When using the TURBOVAC inside a magnetic field, the magnetic induction at the pump housing surface may not exceed the values of $B = 70$ Gauss. To avoid damage we connected the pump to the 100 mm long conflat flange even though is is not recommended and will decrease the pumping speed. Hence, the pump is located at a position where the magnetic field is less than 70 gauss. Another possibility is to wrap the pump up with μ-metal, hence the μ-metal will cause magnetic shielding and the long connection "tube" would be avoided.

The rotary vane pump, a TRIVAC D25B, is used as a fore-vacuum pump. It is located below the machine and connected to the TURBOVAC via a metal hose. The oil vapor exhaust from the pump is led out of the building through a hose. The TRIVAC is able to pump a chamber down to a pressure of $< 1 \cdot 10^{-4}$

mbar, with a pumping speed of 7.1 l/s. The TURBOVAC is able to pump the chamber further down to a pressure of $< 8 \cdot 10^{-9}$ mbar at a pumping speed of 55 l/s for N_2 gas. This is the technical data given in the product data sheets. The real pressure and pumping time achievable in Menja is also effected by the chamber geometry, leak- and out-gassing- rates and the flange that connect the pumps to the chamber. The minimum pressure achieved in Menja is $9.0 \cdot 10^{-7}$ mbar.

The pressure of the working gas is controlled by a manual needle valve where the gas is introduced into the chamber. The valve opens so that the wanted pressure is achieved when the gas flow through the valve and the pumping speed are in equilibrium. This system gives a quite stable pressure, but it is difficult to adjust the pressure to the desired value.

The pressure is measured by a penning gauge (PENNINGVAC PM31) where the gauge head is connected to a port close to the vacuum pump. Operation of the PENNINGVAC is based on the cold cathode principle. To measure the pressure a gas discharge is produced within the sensor by applying a high voltage. The ion current created is then output as a signal which is proportional to the prevailing pressure. The sensor design permits "reliable" measurement operation in a pressure range between $1 \cdot 10^{-9}$ and $1 \cdot 10^{-2}$ mbar. The measurement uncertainty inherent in cold cathode gauges in this range is $\pm 30\%$. The instrument is calibrated for air (N_2), hence the actual gas pressure is $P_{\text{eff}} = K \cdot P_{\text{nom}}$, where K is a proportionality constant depending on gas type, $K(\text{argon}) = 0.8$. Hence, to obtain the real argon pressure we must multiply the nominal pressure by the transformation factor equal to 0.8. Note that later reference to the operating pressure will be given by the nominal pressure.

4.3 Microwave power system

The microwave power system is shown in Figure 4.3. A DC power supply drives a magnetron source producing waves with frequency 2.45 GHz. The power supply is able to deliver power between 0.5 to 5 kW.

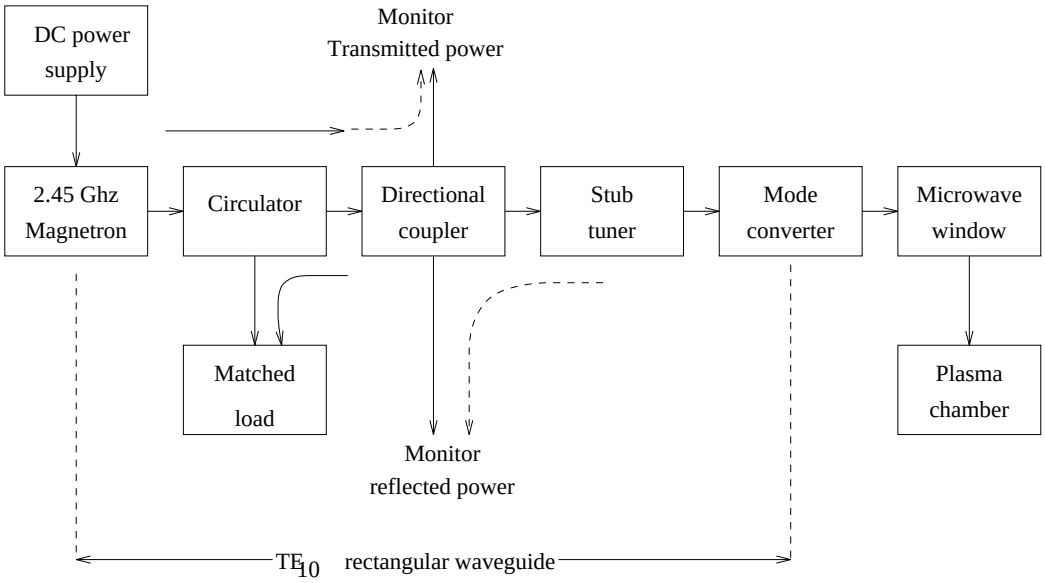

Figure 4.3: A schematic drawing of the major components of the microwave power system in Menja

The circulator is a non-reciprocal waveguide device. The general properties of the circulator are given schematically in Figure 4.4, which shows its circuit symbol. Power is incident on port 1 and will exit at port 2 and there will be no power coupled to the other ports. Similarly power incident on port 2 will exit at port 3, etc. The circulator is coupled so that the magnetron is connected to port 1, the waveguide leading to the plasma device to port 2, and the matched load (also called dummy load) to port 3 (see Figure 4.3). The microwave power circulates from the magnetron source to the plasma, but diverts the reflected power to the matched load where it is absorbed. Hence, the magnetron head is protected against any reflected power on the transmission line.

The matched load absorbs all the electromagnetic waves entering the loader, without causing reflection of electromagnetic power from the termination. The matched load operates as a one-way valve for microwave power, it can dissipate 2 kW continuously and 5 kW for up to one minute.

A directional coupler consists of microwave circuit elements. It measures the

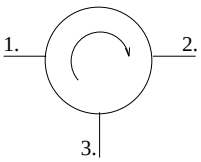

Figure 4.4: The circulator circuit symbol

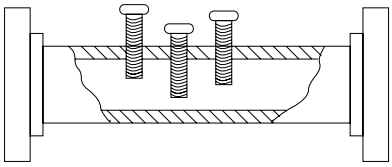

Figure 4.5: Three-stub tuner

microwave power passing through the circulator and the directional coupler into the plasma source, and it also measures the microwave power reflected from the plasma and absorbed at the matched load. The difference between the measured powers is absorbed by the plasma or dissipated in the rest of the system, as heating of chamber- and waveguide-walls etc.

The three-stub tuner is used to match the impedances presented by the system, and thus minimize the reflected power from the waveguide system. The effects of any mismatch in a waveguide system can be cancelled by introducing another mismatch elsewhere in the system whose reflection coefficient is in anti-phase with that of the original mismatch, hence cancelling the reflected wave. The stub tuner produces variable mismatches with variable phase. This is done by using a number of posts at fixed positions in the waveguide, shown in Figure 4.5, then a suitable combination of post insertions will give the required mismatch in the correct phase. According to Baden Fuller (1969) any mismatch could be cancelled using three posts or stubs.

Waveguides

Waveguides connect different parts of the microwave power system, and guides the microwaves into the plasma chamber. The size and shape of the waveguide affects the wave mode propagation, and the length of the guide improve matching of the system. The size of the waveguide is intimately related to the wavelength/frequency of the wave it is intended to guide. Let us now briefly look at the propagation in a rectangular and a circular waveguide.

Rectangular waveguides

We now consider a rectangular waveguide with dimensions a in the x-direction and b in the y-direction, where $a > b$ by definition. The full set of modes with the mathematical expressions for the fields are determined from the solution of Maxwells equations and the wave equation. Within the waveguide the charge and current densities are zero, hence Maxwells equations becomes:

$$\nabla \cdot \boldsymbol{E} = 0 \tag{4.1}$$

$$\nabla \cdot \boldsymbol{B} = 0 \tag{4.2}$$

$$\nabla \times \boldsymbol{E} = -\frac{\partial \boldsymbol{B}}{\partial t} \tag{4.3}$$

$$\nabla \times \boldsymbol{B} = -\epsilon_0 \mu_0 \frac{\partial \boldsymbol{E}}{\partial t} \tag{4.4}$$

and the wave equation for $\boldsymbol{E}$ is

$$\nabla^2 \boldsymbol{E} = \epsilon_0 \mu_0 \frac{\partial^2 \boldsymbol{E}}{\partial t^2}. \tag{4.5}$$

We now consider a particular sub-set of the waveguide modes which is known to include the most important one. These are the transverse electric modes (TE-modes), in which the $\boldsymbol{E}$-field vector is normal to the direction of propagation $\boldsymbol{E} \perp \boldsymbol{k}$. We also restrict the sub-set by letting the $\boldsymbol{E}$-vector be parallel to the short wall b, i.e. the y-direction, so that $E_x = E_z = 0$ and $E_y \neq 0$ (E_z is always zero in a TE-mode). If the waveguide has perfectly conducting walls the electromagnetic boundary conditions require that the tangential component of $\boldsymbol{E}$ and the normal component of $\boldsymbol{B}$ are zero at the wall ($E_y = 0$ at $x = 0$ and $x = a$ and $B_x = 0$ at $y = 0$ and $y = b$) By solving equation 4.1 to 4.5 with these boundary conditions we obtain (Cronin, 1995)

$$E_y = E_0 \sin\left(\frac{n\pi x}{a}\right) e^{j(\omega t - k_z z)} \tag{4.6}$$

$$B_x = -\frac{k_z E_0}{\omega} \sin\left(\frac{n\pi x}{a}\right) e^{j(\omega t - k_z z)} \tag{4.7}$$

$$B_z = \frac{jE_0}{\omega}\frac{n\pi}{a} \cos\left(\frac{n\pi x}{a}\right) e^{j(\omega t - k_z z)} \tag{4.8}$$

$$B_y = 0, \tag{4.9}$$

where E_0 is the wave amplitude, n is an integer and a is the dimension of the longest waveguide wall.

Equation 4.6 to 4.9 give the fields of the entire class of TE-modes which are labeled TE_{n0}, where n is the integer occurring in the equations above. The subscript 0 indicates the particular subset where $E_x = 0$.

All the modes derived above have a z-dependence $e^{j(\omega t - k_z z)}$, where k_z is related to the wave frequency ω and the integer n characterizing the mode, by the dispersion relation (Cronin, 1995)

$$k_z^2 = \left(\frac{\omega}{c}\right)^2 - \left(\frac{n\pi}{a}\right)^2. \tag{4.10}$$

If k_z is real the wave propagates down the waveguide, and if k_z is imaginary the wave decays exponentially along the guide. For propagation of waves equation 4.10 requires that $\omega >= n\pi c/a$, thus the cut-off frequency ν_c for propagation of a mode is given by

$$\nu_c = \frac{\omega}{2\pi} = \frac{nc}{2a}, \tag{4.11}$$

where the waves with lower frequencies than ν_c are evanescent. This equation shows that the cut-off frequency increases with increasing integer n. For the TE_{10}-mode we have

$$\nu_c(\mathrm{TE}_{10}) = \frac{c}{2a} \quad \rightarrow \quad \lambda_c = 2a, \tag{4.12}$$

where λ_c is the corresponding cut-off wavelength. Although we have not considered all the possible waveguide modes the TE_{10}-mode with the lowest ν_c, has the longest wavelength which can propagate in a waveguide of width a, as given by 4.12, see figure 4.6(a).

Circular waveguides

To determine the wave modes in a circular waveguide we solve the Maxwells equations and wave equation as for the rectangular case. Since the cylindrical geometry is involved, it is appropriate to employ cylindrical coordinates. The

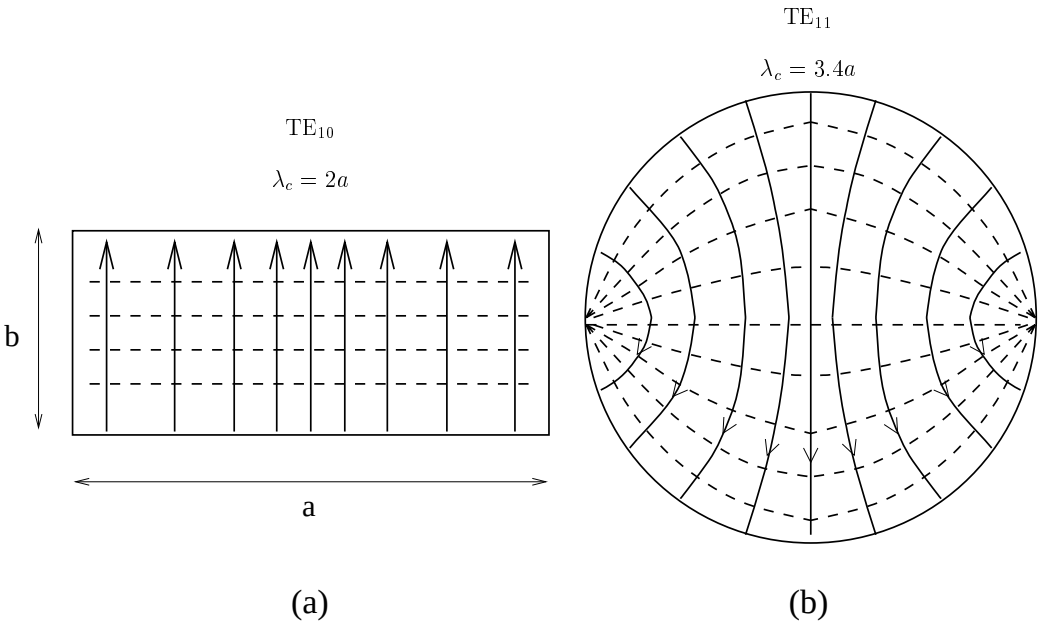

Figure 4.6: Line representation of the fields of the rectangular TE_{10}-mode (a), and the circular TE_{11}-mode (b). The solid lines represents the $\boldsymbol{E}$-field and the dashed lines represents the $\boldsymbol{B}$-field. The density of the lines indicates the field strength.

transverse fields in cylindrical coordinates can be derived from E_z and B_z field components to obtain TM and TE modes, respectively (TM means transverse magnetic). The solutions of equation 4.1 to 4.5 give for the TM-modes a cut-off frequency of (Cronin, 1995)

$$\nu_c(\mathrm{TM_{nl}}) = \frac{cP_{nl}}{2\pi a}, \tag{4.13}$$

and for the TE-mode

$$\nu_c(\mathrm{TE}_{nl}) = \frac{cQ_{nl}}{2\pi a}, \tag{4.14}$$

where P_{nl} and Q_{nl} are the lth roots of the Bessel function $J_n(x)$ and $J'_n(x)$, respectively, where $P_{nl}(\mathrm{TM}_{01}) = 2.41$ and $Q_{nl}(\mathrm{TE}_{11}) = 1.84$. The TE_{11}-mode has the lowest cut-off frequency of all the modes, and is therefore by definition the fundamental mode of the circular waveguide. The propagation is therefore not possible for waves with wavelength larger than 3.4 times the waveguide radius a, $\lambda_c(\mathrm{TE}_{11}) = 2\pi a/P_{nl} = 3.4a$, see figure 4.6(b).

Mode propagation in Menja

The dimension of the rectangular waveguide in Menja are $a = 74$ mm and $b = 35$ mm, hence the cut off frequency for the TE_{10}-mode is $\nu_c = 2.0$ GHz. The dominating mode in our rectangular wave guide is therefore the TE_{10}-mode, where the electromagnetic field lines in the cross section of the guide are as shown in figure 4.6(a).

The rectangular guide is converted to a circular waveguide with radius $a = 50$ mm, before it is connected to the vacuum window. This waveguide size lead to a cut-off frequency for the TE_{11}-mode equal to $\nu_c = 1.75$ GHz. Hence, the dominating mode launched into the vacuum chamber is the TE_{11} circular mode. The electromagnetic field lines for this mode is shown in figure 4.6(b).

Microwave window

Microwaves propagating from the power source/waveguide enters into the vacuum chamber through a microwave introduction window. The window is made of a dielectric transparent to microwaves, which has several functions in the system:

i. It seals the ultra high vacuum from the microwave power system;

ii. It provides the propagation of microwaves of particular modes into the plasma depending on the size;

iii. There is negligible amount of power absorption in the window;

iv. It provides matching of the waveguide impedance and the plasma impedance.

In general, microwave discharges create high densities of exited, charged and free radical species in low pressure plasmas, without having the disadvantage of large sheath potentials and contaminations from electrodes as in the

common RF-discharges. Hence, the microwave power coupled through a microwave window in microwave discharges replace the electrodes in RF-discharges. One weakness with the usage of a microwave window is that the window can be exposed to ion bombardment. The result can be an undesirable erosion of the window and contamination of the plasma, or a deposited thin film/layer on the window changing the transparency. Therefor, the microwave window is the fragile point of the microwave power system, and improvements are necessary. There are several types of microwave windows described in the literature, usually made of different single or multi layered dielectric materials.

One of the first ECR plasma stream sources used a ceramic disk with a thickness of half the wavelength of the TE_{11} circular microwave mode (Kosmahl *et al.*, 1967). Musil *et al.* (1973) showed that high reflection of the incident RHP-wave on a resonant plasma can be considerably reduced if the matching system consisting of dielectric plates is placed in front of the plasma. Musil *et al.* used a double window consisting of two quarter-wavelength dielectric plates, mutually separated by a quarter-wavelength gaps, $\frac{1}{4}\lambda$, which resulted in more than 95 % microwave power absorption in the plasma. The most common window used in ECR experiments is a single quartz window, used by Gadgil *et al.* (1992), Gorbatkin and Barry (1992a), Ono *et al.* (1986), and Popov (1989) to mention some. Misina *et al.* (1997) also use a quartz window. In this case the window was screened from the plasma sputtering when a double bended rectangular waveguide was coupled between the window and the vacuum chamber.

Torii *et al.* (1987) developed a double layer window to protect the microwave introduction window from back-stream particles (electrons and ions). A dielectric block made of heat resistant material was placed between the quartz window and the plasma chamber for protection. With an appropriate combination of materials in the window it can also improve the microwave introduction efficiency. Torii *et al.* found that with a quartz and alumina window, the density is three times higher than with quartz and BN. The explanation given is that alumina has higher dielectric constant compared with quartz and BN, and will therefor allows better impedance matching for a higher

plasma density. Which is in agreement with the work done by Stevens *et al.* (1991) where the impedance matching using dielectric windows is examined.

Gorbatkin *et al.* (1990) use a single quartz window in the ECR microwave plasma system, and with powers $\geqslant 750$ W and downstream pressure of $\leqslant 5$ mTorr the window became coated due to sputtering from the chamber walls. An *in situ* technique for cleaning the window was developed so that reproducible measurement were achievable. This technique is described in Gorbatkin and Barry (1992a), the keys to cleaning the window are the specific magnetic field configuration and operation at low pressure. The magnetic field is produces so that the EC-resonance is close to the window, and increasing away from the window. Thus, the electrons are rapidly lost to the window since they are accelerated towards the decreasing field. The resulting space charge field accelerates ions towards the window. Since low pressure increases the electron temperature, it drives up the plasma potential, and provide high enough ion energies for sputtering and thereby cleaning of the window.

Some authors has solved the problem with the microwave window by using a coaxial converter instead of the window. The microwaves are then usually converted from the waveguide to a coaxial line and introduced to the source through a coaxial-horn antenna. This is done in O'keeffe *et al.* (1997), Fujiyama *et al.* (1993), and Sakudo *et al.* (1977). Coaxial cables are less capable of transmission higher-power microwaves than waveguides, and horn antennas cause many kinds of contamination inside the vacuum chamber (Hidaka *et al.*, 1993). Hence, to obtain a uniform and dense plasma the selection of microwave windows for the power transmission appears to be the best alternative.

In Menja a water cooled single layer ceramic window was first used between the waveguide and the chamber. It was 100 mm in diameter and 14 mm thick. Unfortunately this window cracked after about 10 hours of operation. The crack was large enough to be visible. A deposited film was visible on the vacuum side as shown in Figure 4.8. This film is not likely the cause of the crack, it should only prevent microwave transmission. One possible cause of

the crack is high material stress due to large temperature gradients. These gradients were created since the water encircled the window-edge, i.e. cooled the rim of the surface, while the central or entire window surface was heated by ion impact.

The ceramic window was replaced by an air cooled single layer quartz window, with thickness 16 mm. Compressed air is introduced through a hole in the microwave mode converter, where a manual reduction valve reduces the air-pressure to a suitable level. Several holes are made in the converter wall to let the air out, and a fine meshed metal-net surrounds the converter to avoid microwave leakage. The air cools the entire surface of the window, hence avoiding large temperature gradients as in the water-cooled ceramic window. After about 10 to 15 hours of operations large microwave reflections was a problem, and it was difficult to achieve a discharge. A deposited film was observed with the same pattern as for the ceramic case, see Figure 4.8.

4.4 Magnetic field

Calculation of the magnetic field for some coil configurations makes it possible to find the optimal positions of the coils for ECR plasma generation. On the axis of symmetry of the coil system the calculation of the field is fairly simple, using Amperes low for the magnetic field. The magnetic field strength of a circular loop, carrying a current I, at an axial position R from the center is given by

$$B_z(R) = \frac{\mu_0 I a^2}{2\left(a^2 + R^2\right)^{3/2}}, \tag{4.15}$$

where μ_0 is the vacuum permeability, a is the radius of the loop, and B_z is given in Tesla ($= 10^4$ Gauss). Hence, the field strength from a coil containing N windings is given by NB_z, where the radius a in equation 4.15 is now the mean radius of the coil. The total magnetic field from all the coils is the sum of the magnetic field from each coil,

$$B_{tot}(R) = \sum_{i=1}^{n} N_i B_z(I_i, R_i, a_i), \tag{4.16}$$

taking $R = 0$ to be the vacuum window position so that $R_i = R-$coil position with respect to the vacuum window. $B_{z,i}$ is the magnetic field generated by one winding of coil i and is given by equation 4.15, and N_i is the number of windings in the coil.

To calculate the magnetic field in Menja, a program developed by Fredriksen (1995) to study the contour-lines from the $\boldsymbol{B}$-field of an ensemble of coils was used. One example of the field lines are plotted in the drawing of the chamber in Figure 4.2. The field lines are calculated for the coil configuration described below, with a coil current of 240 A.

There are mainly four magnetic field structures described in the literature:

i. Radially and axially uniform magnetic field;

ii. Divergent field;

iii. Mirror field;

iv. Mirrorlike structure with downstream magnets.

All four magnetic field configurations have their own magnetic coil arrangement. It is necessary to optimize the magnetic field configuration to generate a uniform ECR plasma. This optimalization has been investigated by several authors and reviewed by Popov (1994). Different conclusion are reached depending on the purpose of the plasma source.

The uniform magnetic field reduces radial plasma losses and decreases wall material sputtering caused by ion bombardment and thereby reduce the contamination of the plasma. Murata *et al.* (1992) measures the axial distribution of the plasma parameters and the deposition rate obtained, using a uniform as well as a divergent magnetic field. They conclude that the plasma density is more homogeneous in the axial direction in the uniform field than in the divergent field, and that the deposition rate is larger in the uniform field. The conclusion in this paper is that the uniform magnetic field is more

useful for ECR PECVD than divergent magnetic field. To produce a uniform magnetic field in the entire axial length of a source chamber the coils have to be separated by a certain distance, and more coils than the number producing a divergent field are needed. In Murata *et al.* eight coils are used to produce the uniform mirrorlike field, while six coils are used for the divergent field. Therefore, producing a divergent field is less complicated from the engineering point of view, and with lower costs compared to a uniform field.

Hirotsu *et al.* (1994) are also comparing the plasmas arising from using uniform or divergent magnetic field, but they measure the radial distribution of the plasma parameters, instead of the axial distribution as in Murata *et al.* (1992). The experiments show that the magnetic field strength at the injection point affects the coupling of the electric field of the injected microwaves with the waves propagating in the plasma. They found that efficient conversion of the TE_{01} mode to generate a uniform ECR plasma occurred for high magnetic field strength at the injection point. This is more easily achieved with a divergent field.

The first applications of a mirror magnetic field for ECR electron heating were made in the context of magnetic fusion experiment (Seidl, 1964; Lichtenberg *et al.*, 1969). The microwave power absorption was associated with the heating of a single electron bouncing between two mirrors with many passages through two ECR zones. However authors who use a mirror magnetic field in ECR plasma sources for plasma processing, report that one ECR region is sufficient for complete microwave power absorption, provided the plasma density exceeds cutoff density (Popov, 1994).

Matsuoka and Ono (1988) investigate the magnetic field gradient effects on ion energies in ECR plasma. It is shown that the floating potential profile strongly depends on the magnetic field configuration. The floating potential decrease is reduced for the mirror field compared with the divergent field. The ion energy depends on the potential difference between the plasma and the surface and therefore the mean ion energy in the mirror field is lower than in the divergent field. Consequently, the mirror field has a cooling effect on

dense plasma outside the resonance area.

In the review by Popov (1994) it is claimed that ECR plasma sources with a divergent magnetic field are attractive for PECVD technology because of the enhancement of the ion deposition process by the ion bombardment of the growing film. Two coils placed around an ECR plasma chamber and one coil set downstream is probably the most popular configuration in the 1990's.

The magnetic field in Menja is generated by maximum nine magnetic coils. Due to the lack of independent power supplies for the coils, we have to connect all the coils in series so that the same current flows through all the coil. The power supply delivers up to 400 A at 50 volts. By calculating the magnetic field for the nine coils in different positions, using equation 4.16, one can arrange the coils to obtain a magnetic field distribution satisfying the following criteria:

i. The ECR surface is located in the neck of the chamber, i.e. on a "point" along the neck the magnetic field strength has to be 875 Gauss.

ii. In view of the discussion in section 4.3 about the ion bombardment on the microwave window, one way of avoiding large damaging effects is to produce a maximum magnetic field $>$ 875 Gauss at the microwave window. The charged particles are accelerated in a diverging magnetic field and decelerated in a converging field, hence the ions bombarding the window will be decelerated before they hit the window, and the damaging effect is reduced.

iii. From the engineering point of view the coils can not be placed where they will obstruct access to diagnostic ports, cooling and gas connection, etc.

Taking these three points into account we decided to arrange the coils as shown in Figure 4.2. The magnetic field is generated by 9 independent circular coils carrying a DC-current. Eight coils, called the production coils (see Figure 4.2), are placed at the neck and control the electron cyclotron resonance. The production coils have an inner diameter of 20 cm, outer diameter

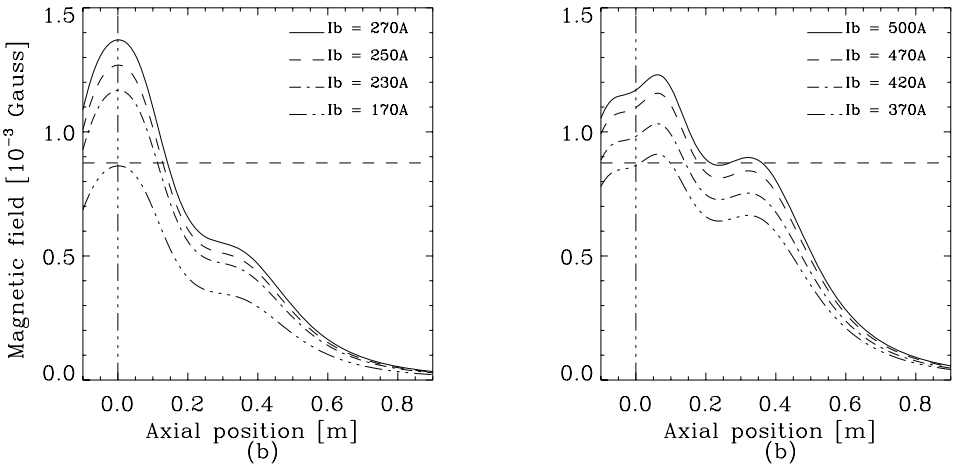

Figure 4.7: The magnetic field from 9 (a) and 5 (b) coils.

of 36 cm, a width of 2 cm and 18 windings of copper conductor with a bore for cooling water. These coils are assembled in two sets of four coils each, with no space between them. One set is positioned in front of the vacuum window and the other after the window 2 cm from the first set. One larger coil, the confinement coil, is located in the expansion area, 35 cm from the vacuum window. This coil reduces the divergence of the field, and thereby controls the effective plasma diameter and the confinement. It has a width of 6 cm, an inner diameter of 38 cm and a outer diameter of 60 cm. It has 60 windings of hollow copper conductors which allows water cooling.

The total magnetic field strength for this configuration are plotted in figure 4.2 and 4.7(a), for four different coil-currents. In the figures the resonance value, 875 G, is indicated as a horizontal stapled line. The vacuum window is located at the axial position 0. We can see that a threshold coil-current at about 170 A is needed to achieve a resonance inside the vacuum chamber. If the coil-current is lower than this threshold value no resonance surface exists on the vacuum side, and no discharge will occur. The coils are arranged so that the magnetic field strength peaks at the vacuum window, so for higher coil-currents there are two resonance positions, but only one is located inside the chamber. Figure 4.7(a) shows that when the current increases, the

resonance surface moves to the right, but the shape of the field is the same for all currents. When the current is 300 A the resonance is just outside the neck.

We are able to disconnect some of the coils, to use fewer coils, or to change their positions. These adjustments will affect the shape of the field. One example is plotted in Figure 4.7(b). Here the two first and the two last of the production coils are used together with the confinement coil. As we can see from the curves corresponding to coil current 370 A and 500 A there can be more than one resonance surface in the chamber. One disadvantage of this arrangement is that we need higher current to produce a resonance since we use fewer coils. The maximum current for our power supply is 400 A, so the 500 A example is ruled out. In this thesis variations in the magnetic field will be made by varying the current in the interval between 200 A and 300 A, retaining all nine coils.

4.5 Trouble shooting

During operation there are some problems producing a stable plasma for curtain parameter regimes. The reflection are then high and they are very difficult to reduce. We can also observe a fluctuation light from the plasma under this conditions. Usually this happens for very low or very high pressures. If the tuning does not succeed it usually helps to slightly adjust the coil current. From experimental experience the pressure around $1.5 \cdot 10^{-4}$ mbar is a difficult pressure regime. In some occasions the plasma died out suddenly or no discharge was achieved during start up even if no microwave reflection was measured. Under one of this events a large microwave leakage was observed in the space surrounding the device. Investigation showed a "thick" deposited film on the quartz window as shown in figure 4.8(b). During operation with the ceramic window there were also some problems with reflections, and the same pattern of the deposited film was observed as shown in figure 4.8(a). In this figure also the crack discussed in section 4.3 is clearly shown.

The injected microwave power could in principle be varied from 0.5 to 5 kW, but in practise 0.5 to 2.5 kW. The operational problems are probably due to a mismatch in the system, which is larger for some operating conditions. Most probably this mismatch is due to the "home-made" microwave converter which is slightly uneven and dented in shape.

Figure 4.8: The coated microwave windows. (a) shows the ceramic window with the crack. and (b) shows the quarts window.

Chapter 5

Results

5.1 Langmuir probe measurements

The Langmuir probe measurements are done by one axial and one radial probe. The axial probe is a plane probe of tungsten with diameter 18 mm. This probe is used to scan in axial direction from 23 cm to 50 cm from the microwave window, as well as to obtain the characteristics when the coil current or the argon pressure are varied at a constant axial position 45 cm from the vacuum window. The radial Langmuir probe is a cylindrical probe with diameter 0.2 mm and length 2 mm, which scans the radial cross section of the chamber 45 cm from the window. The characteristics are obtained at two different nominal pressures $2 \cdot 10^{-3}$ and $5 \cdot 10^{-4}$ mbar, which will be referred to as the high and low pressure, respectively. For each pressure three different coil currents 230, 250 and 270 Ampere' are used, which are plotted with circular, diamond and triangle points, respectively in all the results shown in this thesis.

Electron temperature

The electron temperatures obtained with the Langmuir probes are shown in Figure 5.1. In (a) and (b) the radial temperature results are shown, in

(c) and (d) the axial results. (e) is obtained with increasing coil current at constant high pressure, and (f) is obtained with increasing pressure at two different constant coil currents, 230 A and 270 A.

In the radial measurements we can see that the temperature peaks at a distance -5 cm and 6 cm from the center, while decreasing inwards to reach a minimum at the center. This tendency is most pronounced for the low pressure where the difference from peak to center is about 4 eV, which correspond to a 50% difference between maximum and minimum, while for the high pressure it is only a difference of 2 eV which results in a 30% difference.

Looking at the axial dependence in figure 5.1(c) and (d) we see a decreases in T_e when the distance from the window increases. T_e decreases most in the low pressure regime, where the 230 A coil current gives the largest gradient with a difference of 2 eV. The largest temperature is about 6 eV at the position closest to the window, and the smallest temperature is 2.5 eV at the largest distance (45 cm) from the window. At the high pressure there is a difference between largest and smallest temperature of 1 eV, where the largest temperature is 6 eV at the position closest to the window.

Increasing the coil current from 230 A to 330 A, in the same axial position 45 cm from the window and at a constant high pressure, results in a decrease in the electron temperature from 5 eV to 3 eV, see Figure 5.1(e). Also in Figure (c) and (d) we can see that the lowest coil current gives the highest electron temperature.

When the pressure increases from $2 \cdot 10^{-4}$ to $9 \cdot 10^{-3}$ mbar, in a constant position, we can see two slightly different results for the low and high coil current. For the low current case, 230 A, T_e decrease with increasing pressure from 5 eV to 2.5 eV, where after it is nearly constant between $2 \cdot 10^{-4}$ and $2 \cdot 10^{-3}$ mbar. For the high current case, 270 A, there is a minimum temperature at $1 \cdot 10^{-3}$ mbar where $T_e \approx 2$ eV, for lower pressure T_e increases sharply to a value about 6 eV, and for a larger pressure the temperature increases to 4.5 eV at about $2 \cdot 10^{-3}$ mbar before it decreases following the low coil current trend.

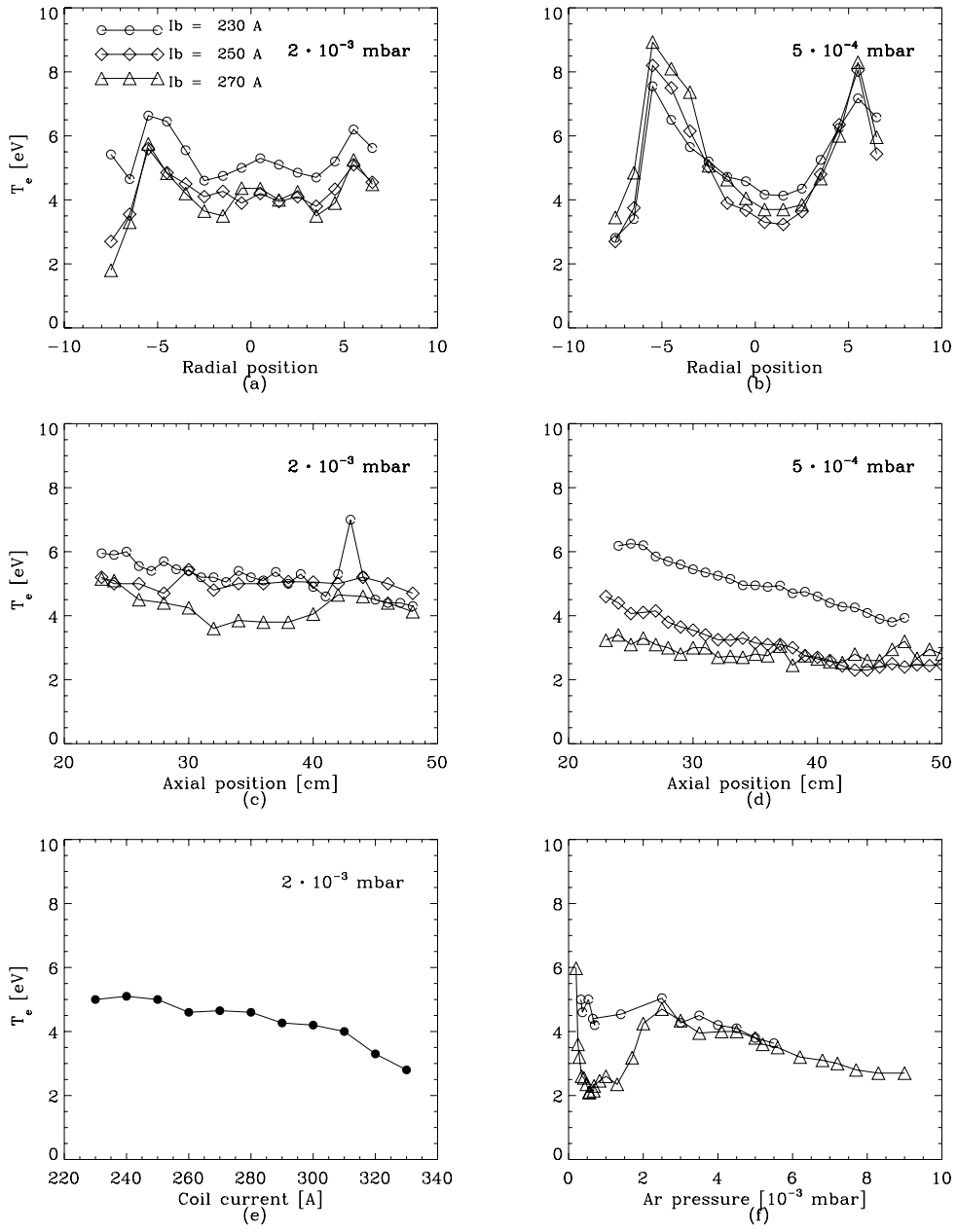

Figure 5.1: Electron temperature from Langmuir probe measurements. (a) and (b) are radial scans 45 cm from the vacuum window in the downstream position using a cylindrical tungsten probe. (c) and (d) are axial scans where axial position 0 is at the vacuum window. These results are obtained with a plan tungsten probe. (e) and (f) are obtained with the plan probe in the same position as the radial measurements (45 cm from window). (e) are obtained while increasing the coil current and (f) are obtained increasing the argon pressure.

Plasma potential

The plasma potential obtained with the Langmuir probe measurements are shown in Figure 5.2. In (a) and (b) the radial results are shown, in (c) and (d) the axial results, while (e) and (f) show the behavior with increasing coil current and argon pressure, respectively.

In the low pressure regime we can see that the plasma potential is constant in the entire radial cross section, where 230 A coil current gives a plasma potential of 33 V $\pm 5\%$ while a current at 270 A gives V_p equal to 40 V $\pm 5\%$. In the high pressure the plasma potential is less uniform. The worst case is at 230 A coil current where V_p increases from 23 V to 30 V outwards from radial positions about ± 5 cm from the center, which result in a difference of 25 %.

The axial dependence (figure 5.2(c) and (d)) show a decrease in V_p at high pressure from 28 V closest to the window to 25 V at the largest distance from the window. At low pressure V_p is higher with an even smaller gradient compared to the high pressure regime.

The plasma potential shows no dependence on coil current, which differs from both the axial and radial measurements where a difference in the potential for the different currents are obtained. Note that this difference is largest in the low pressure regime, and the variation with coil current is obtained in the high pressure regime which shows only a small change in the potential.

Figure 5.2(f) shows that the plasma potential decreases with increasing pressure, with the gradient being largest for low pressure. We also observe that in this measurement there is no difference in the two cases of 230 and 270 A.

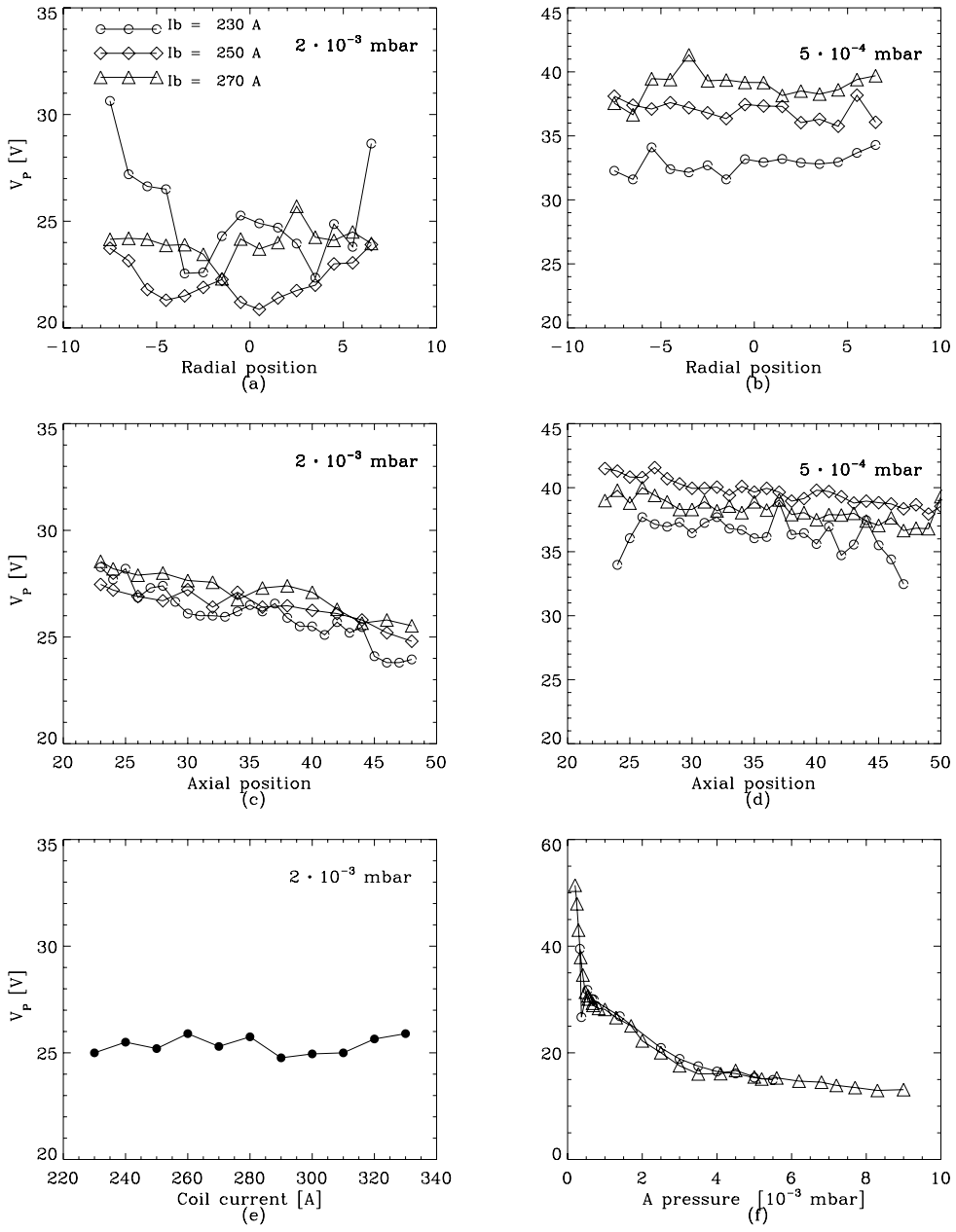

Figure 5.2: Plasma potential from Langmuir probe measurements. (a) and (b) are radial scans, (c) and (d) are axial scans, while (e) and (f) show variations with coil current and pressure, respectively.

Plasma density

The plasma density obtained with the Langmuir probes are shown in Figure 5.3. In (a) and (b) the radial results are shown, in (c) and (d) the axial results, while (e) and (f) show the dependence with increasing coil current and argon pressure, respectively as for the temperature and plasma potential results.

The radial densities, figure (a) and (b), are quite uniform with a variation $<$30 % over the cross section until it decreases sharply near the edge, at a radial position from -6 to -3 cm and 4 to 6 cm from the center depending on the coil current and pressure. The best uniformity is achieved when the coil current is 250 A for both the high and low pressure, at which the density is constant at a value about $7 \cdot 10^{16}\mathrm{m}^{-3} \pm 10\%$ over a diameter of 11 cm. The density is largest for 270 A coil current with a maximum density of $1.2 \cdot 10^{17}\mathrm{m}^{-3}$, but with pore uniformity.

Looking at the axial dependence for the large pressure, figure 5.3(c), we see an increase in density when the distance from the window increase. For the low pressure we can also see a slightly increasing density with increasing axial position, figure (d). The density values from the radial results agree well with those obtained from the axial measurements 45 cm from the window.

Figure 5.3(e) shows that the plasma density increases with increasing coil current, and there is no sign of saturation at the highest currents. The minimum density, at 230 A, is $3 \cdot 10^{16}\mathrm{m}^{-3}$ while the maximum density is $1.4 \cdot 10^{17}\mathrm{m}^{-3}$ at 330 A coil current.

When the pressure increases, 5.3(f), we observe two slightly different behaviors for the low (230 A) and the high (270 A) magnetic field, as in the temperature versus pressure result in figure 5.1(f) The results at 230 A show that the density is constant or slightly decreasing until the pressure is $2.5 \cdot 10^{-3}$ mbar where it increases until it saturates at $5 \cdot 10^{-3}$ mbar at a value of $1.3 \cdot 10^{17}\mathrm{m}^{-3}$. The result at 270 A coil current has a maximum of $1.1 \cdot 10^{17}\mathrm{m}^{-3}$ at $5 \cdot 10^{-4}$ mbar, following by a minimum at $2.5 \cdot 10^{-3}$ mbar from where it increases until it saturates at $2.7 \cdot 10^{17}\mathrm{m}^{-3}$ at a pressure around $7 \cdot 10^{-3}$ mbar.

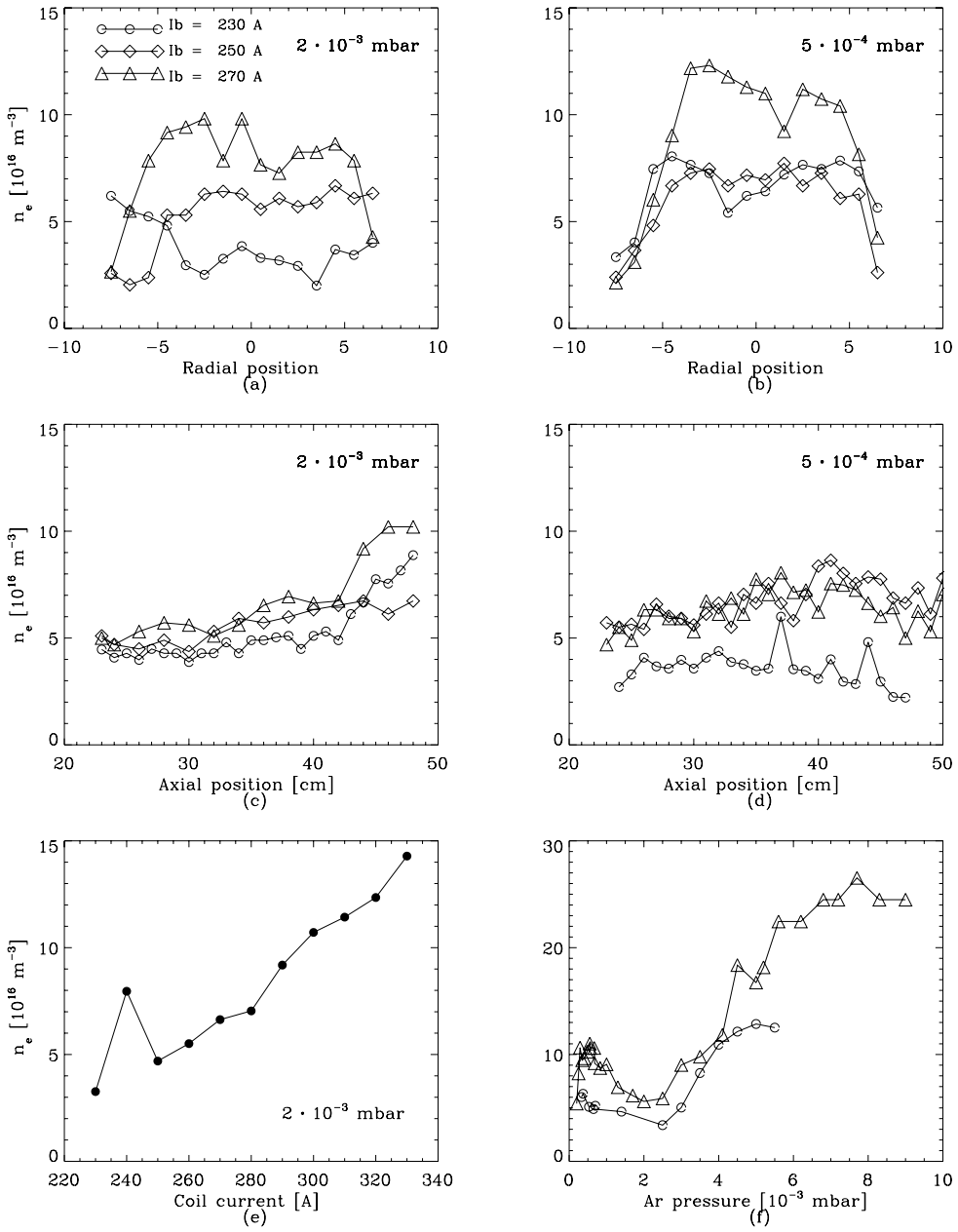

Figure 5.3: Plasma density from Langmuir probe measurements. (a) and (b) are radial scans obtained 45 cm downstream from window, (c) and (d) are axial scans, and (e) and (f) show the dependence on coil current and argon pressure, respectively, as measured 45 cm from the window.

5.2 Ion saturation current

The ion saturation current is measured with the radial and axial probes being held at a constant negative potential to achieve ion saturation. This negative potential was by a mistake held at a too large potential (about -300 Volt) which results in a large increase in the sheath thickness, see equation 3.15 in section 3.1. Thus, the ion saturation current measured is too large. This mistake was corrected by comparing the axial and radial result for the high pressure and high magnetic field (270 A), with the same radial and axial measurements using a moderate negative bias of -50 Volt. This comparison showed that the high bias measurement and the moderate bias measurements differed by a factor of 1.7 axially and a factor 2.4 radially. The reason for the different factors are probably caused by the geometrical difference of the axial and radial probes. Therefore, the high bias measurements represented in Figure 5.4 are divided by 1.7 and 2.4 for the axial and radial results, respectively.

The radial result for the high pressure 270 A coil current shows a flat uniform ion saturation at a value of 30 mA/cm^2 $\pm$ 7% over a radial distance of 12 cm. The other radial results show small dips in I_{sat} in the center, with this tendency being largest for the low pressure, with 30 % difference between maximum and minimum. We can also see that the ion saturation values for the low pressure are larger than for the high pressure.

In the axial direction we see a small decrease from the vacuum window and downstream, with a difference of about 3 mA/cm^2 for the high pressure and $<$2 mA/cm^2 for the low pressure.

Figure 5.4(e) shows that I_{sat} increases with coil current in both the low and high pressure regime. Figure 5.4(f) shows that I_{sat} decreases when the pressure increases from $2 \cdot 10^{-4}$ to $2.5 \cdot 10^{-3}$ mbar, and when the pressure increases further I_{sat} increases until it saturates. For the 230 A case I_{sat} saturates at about 35 mA/cm^2, and for 270 A I_{sat} saturates at 60 mA/cm^2.

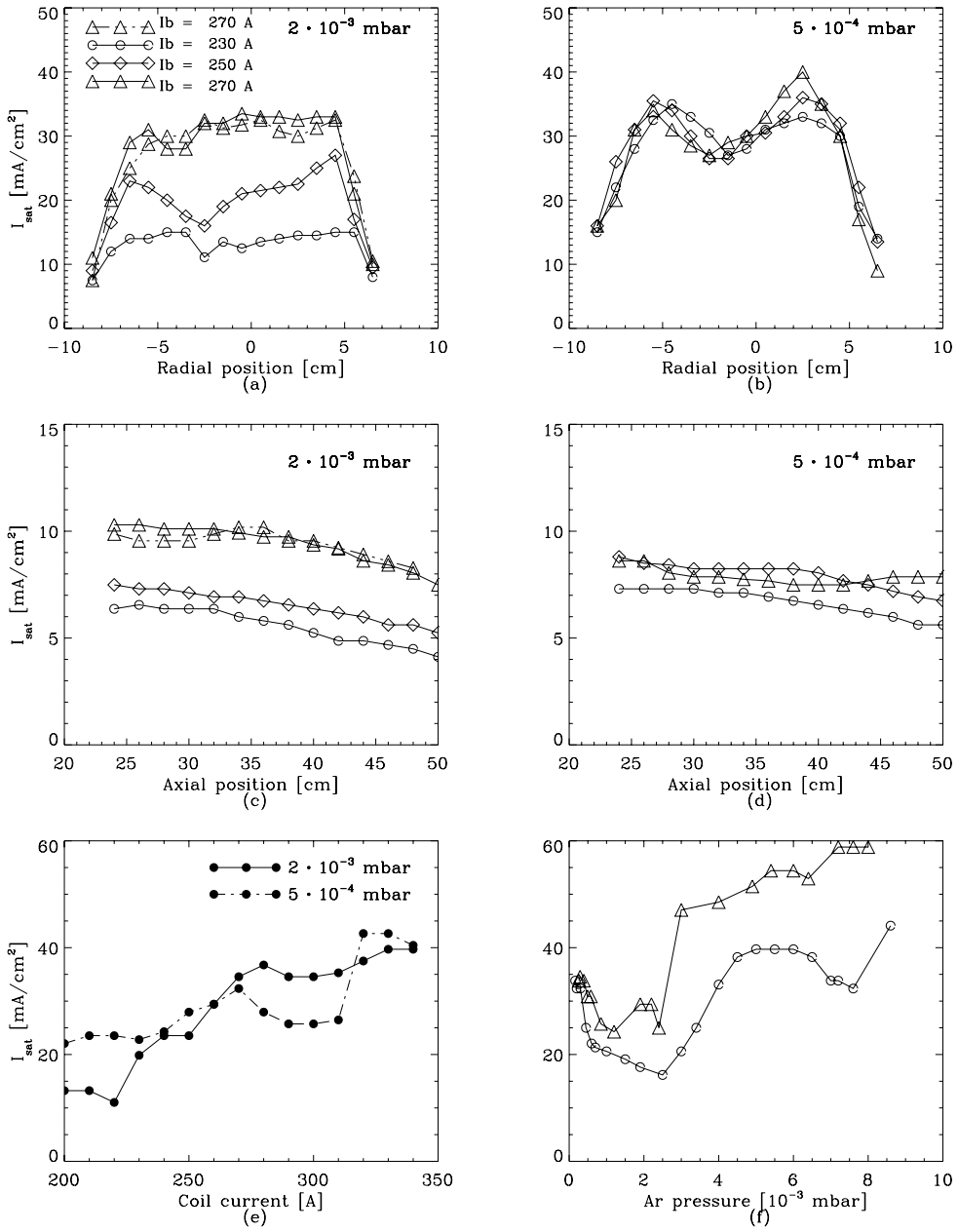

Figure 5.4: Ion saturation current measured by the radial and axial probes. (a) and (b) show the radial scans 45 cm from the window for high and low pressure, respectively. (c) and (d) show the I_{sat} in the axial direction for the high and low pressure, respectively. (e) are obtained by changing the coil current for both high and low pressure and (f) are obtained increasing the argon pressure from $2 \cdot 10^{-4}$ to $9 \cdot 10^{-3}$ mbar using two different coil currents.

Ion density from the ion saturation current

The ion density can be found from the ion saturation current and the electron temperature by equation 3.26 in section 3.3. The ion densities shown in figure 5.5(a) and (b) are calculated from the current obtained by the radial and the axial tungsten probes respectively, while (c) are obtained from I_{sat} measured by a stainless steal flux probe of 58 mm in diameter.

In the calculation of ion density in (a) and (b) we used the electron temperature results from the Langmuir characteristics to find the ion acoustic velocity, $C_s = \sqrt{T_e/m_i}$. Thus, by using the results from figure 5.1(b) and 5.4(b) we obtain the ion density in the radial cross section shown in figure 5.5(a). The results from 5.1(c) and 5.4(c) gave the ion density in the axial cross section shown in figure 5.5(b).

The radial ion density is fairly constant at a value about $1.2 \cdot 10^{17}\text{m}^{-3}5\%$ over a radial distance of 7 cm in diameter before it decrease. The axial ion density decreases slightly downstream from the window. The largest density is obtained at 270 A coil current with a value about $1.7 \cdot 10^{17}\text{m}^{-3}$ in the position 32 cm from the window. The smallest density, $6 \cdot 10^{16}\text{m}^{-3}$, is achieved with 230 A coil current furthest away from the window.

Ion saturation measurements obtained with the flux probe were done without corresponding Langmuir probe measurements. Thus, the electron temperature is not given so we estimate T_e to be 4 eV when calculating the ion acoustic velocity. This experiment was done in a constant low pressure, changing the input microwave power from 500 to 2000 W. The experiment was done with the ceramic vacuum window, and due to some problem with microwave reflections the coil current was changed during operation because this reduced the reflections. From Figure 5.5(c) we can see that the ion density increases with power, and there is no sign of saturation. The largest density is obtained at 2000 W with a value of $9 \cdot 10^{17}\text{m}^{-3}$. The dashed line is the plasma density versus power calculated using equation 2.30.

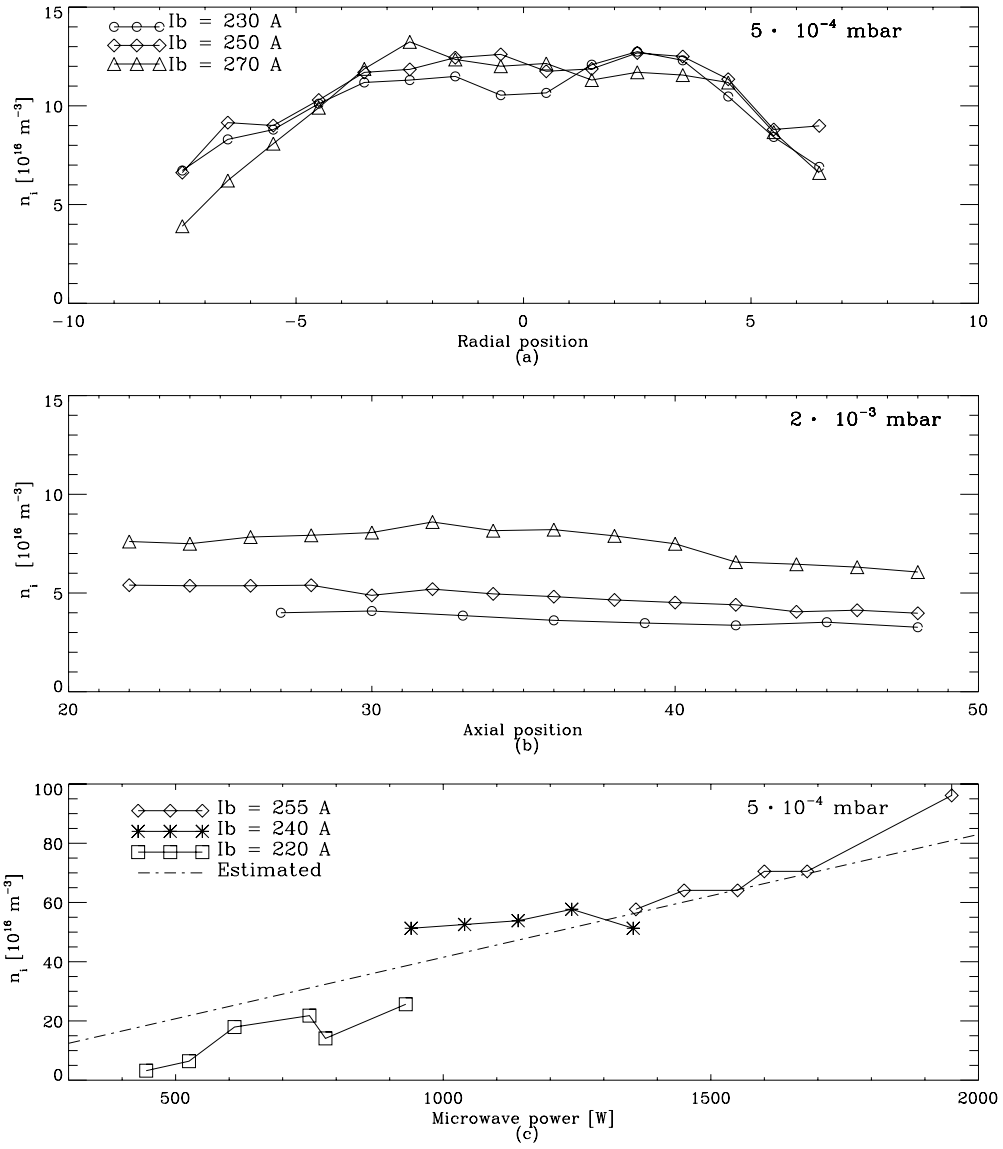

Figure 5.5: Ion density calculated from the ion saturation current. (a) shows the ion density in the radial cross section at low pressure calculated from results shown in figure 5.1 and 5.4(b). (b) shows the results of n_i in the axial direction at high pressure, calculated from results shown in figure 5.1 and 5.4(c). In (c) the results of n_i with increasing microwave power using an estimate of T_e equal to 4 eV, are shown.

5.3 Ion velocity distribution from the IEA

The ion velocity distributions are obtained by the IEA probe as described in section 3.4. The bias used for the IEA grids in the measurements are shown in Figure 3.5, with the front plate grounded, and the first grid floating. The second grid is swept from -3 to +57 V, the third grid is held at -70 V and the collector at -68 V. There was a leakage problem at the probe-entrance each time the probe was moved. Therefore, from practical reasons the probe was kept at four different axial positions 24, 31, 38 and 45 cm from the vacuum window. For each position the vacuum chamber was pumped down to minimum pressure at $3 \cdot 10^{-5}$ mbar, which was very high due to the leakage. In each position the coil current was changed from 220 A to 350 A, given 14 different coil currents, at constant high pressure, and the argon pressure was changed from $2 \cdot 10^{-4}$ to $7 \cdot 10^{-3}$ mbar, given 7 different pressures, using 270 A coil current. The results of the coil current scan and the pressure scan are shown as contour plots in Figure 5.6 and 5.7, respectively. The ion velocity distribution obtained in each position for the coil current 230, 250 and 270 A are plotted in three dimensions in Figure 5.8. The distribution obtained in each position for the pressure $5 \cdot 10^{-4}$, $2 \cdot 10^{-3}$, $7 \cdot 10^{-3}$ mbar are plotted in Figure 5.9.

Coil current dependence

Figure 5.6 shows the coil current dependence on the ion velocity distribution. (a) is obtained 24 cm, (b) 31, (c) 38 and (d) 45 cm from the window. The results in (a) shows a wide distribution which shifts slightly to lower velocities when the coil current increases. At low coil current, 220 A, the ion peak/average velocity is about 12 km/s while for higher coil current, 330 A, the peak velocity is 9.5 km/s. The velocity of 12 km/s equals an ion energy of 30 eV and a velocity of 10 km/s equals an energy of 20 eV. When the probe is moved 7 cm further away from the window, figure (b), the width of the distribution is decreased compared with (a) and the shift in peak velocity from low to high coil current is decreased. In figure (c) the probe is 14 cm

from the start position (a). The distribution is narrower compared to the result in (a). The peak velocity is 12 km/s as for the 220 A case in (a). Increasing the current decreases the velocity until the current is 280 A from where the velocity tend to increase again. At 350 A the peak velocity is again equal to 12 km/s. At the largest distance (45 cm) from the window, shown in figure 5.6(d), a slight increase from 11 to 12 km/s in peak velocity is seen. The overall impression is that the distribution cools down when the distance from the window increases. The distribution width shows no dependence on coil current.

Pressure dependence

Figure 5.7 shows the pressure dependence of the ion velocity distribution. (a), (b), (c) and (d) correspond to the same position as for the coil current variation in figure 5.6. Figure 5.7 shows that in all four positions the distribution shifts towards lower velocities as the pressure increases. Looking at the position closest to the window (a) we see a decrease in peak velocity from 13 km/s to 9.5 km/s when the pressure increases from $5 \cdot 10^{-4}$ to $7 \cdot 10^{-3}$ mbar. This decrease equals a difference in peak energy of 16 eV. 31 cm from the window (b) the distribution shift is lower with a peak velocity changing from 11.5 to 9.5 km/s, i.e. the peak energy difference is 8 eV. 38 cm from the window (c) the distribution shift is even lower with a peak energy difference equal to 6 eV. This energy difference is obtained also at the largest distance (45 cm) from the window, but at this position the velocities has increased compares to the results in (c). In this figure it is difficult to see significant broadening of the distribution.

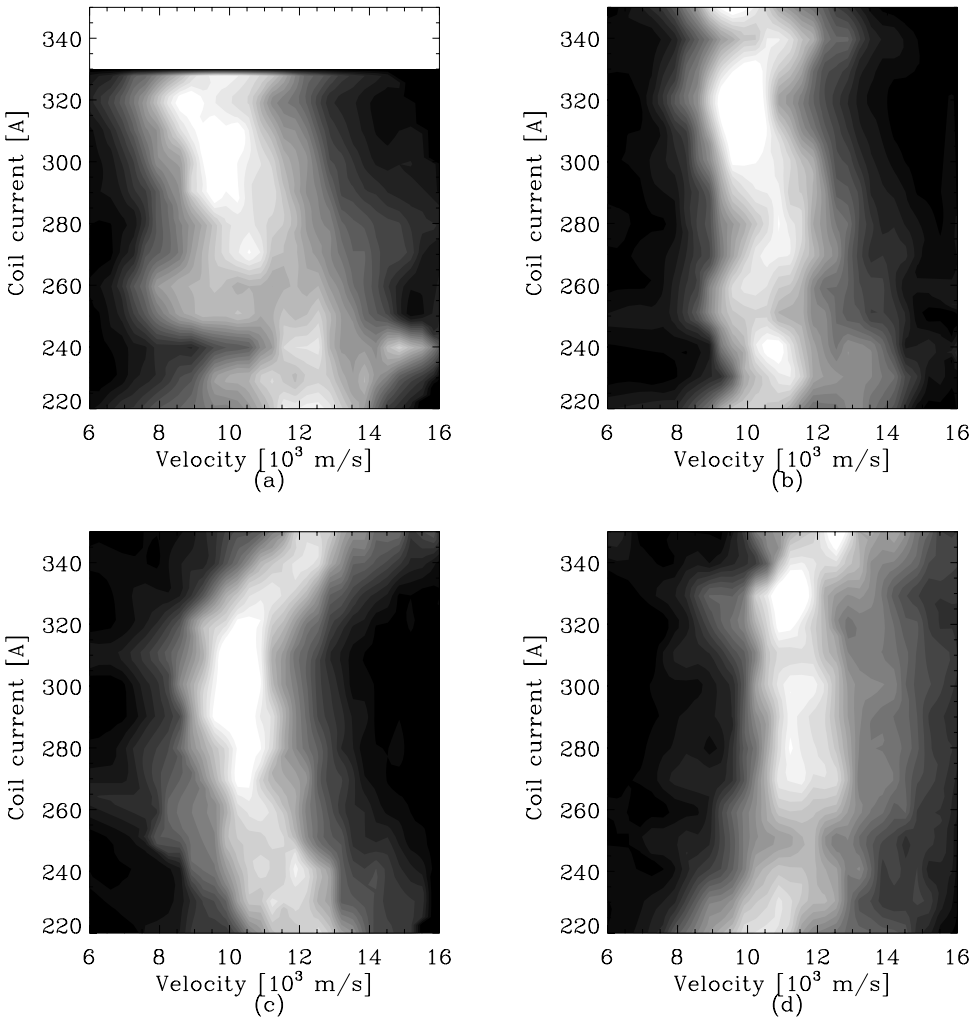

Figure 5.6: Contour plot from the ion velocity distribution obtained by the IEA probe, showing the dependence of coil current at high pressure. (a) is measured 24 cm, (b) 31 cm, (c) 38 and (d) 45 cm from the window.

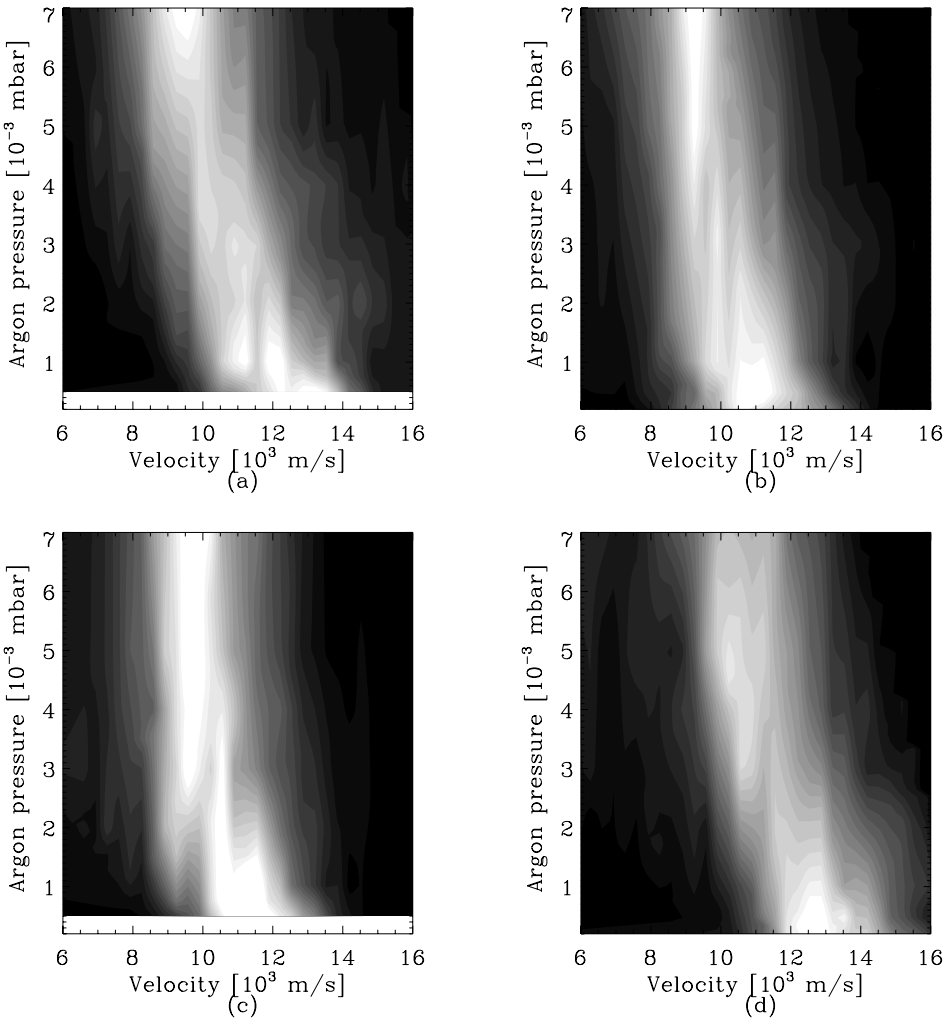

Figure 5.7: Contour plots of the ion velocity distribution obtained by the IEA probe, showing the dependence of argon pressure at 270 A coil current. The IEA is kept in four different positions 24 cm (a), 31 cm (b), 38 cm (c) and 45 cm (d) from the vacuum window.

Position dependence

In figure 5.8 and 5.9 the ion distribution function versus position are plotted in three dimensions. Figure 5.8 are obtained by choosing the distributions at each of the four position for the desired coil current. Figure 5.9 are obtained in the same way choosing the desired pressure.

In Figure 5.8(a) the results obtained at 230 A coil current and high pressure are shown. In (b) the 250 A and in (c) the 270 A coil current results are shown. The distribution shifts when the distance from the window increases first to lower velocities and the to higher velocities. The broadening of the distribution also tend to decrease downstream with the axial position. When the coil current is 270 A (c) the shift is still shown, but the broadening is not that clear.

In Figure 5.9 the results from the pressure variation are shown, where (a) are plotted with $5 \cdot 10^{-4}$ mbar, (b) $2 \cdot 10^{-3}$ mbar and (c) $7 \cdot 10^{-3}$ mbar.

For the lowest pressure, $5 \cdot 10^{-4}$ mbar, figure (a), a shifting of the distribution is clear, first it shifts towards lower velocities then towards higher velocities. When the pressure increases to $2 \cdot 10^{-3}$ mbar (b) the shift is not as distinct as for the low pressure in (a). At even higher pressure $7 \cdot 10^{-3}$ mbar (c) the distribution shifts only towards higher velocities, and the distributions are narrower than for lower pressure.

Note that the parameters in Figure 5.8(c) and 5.9(b) are the same, and they are in very good accordance with each other....

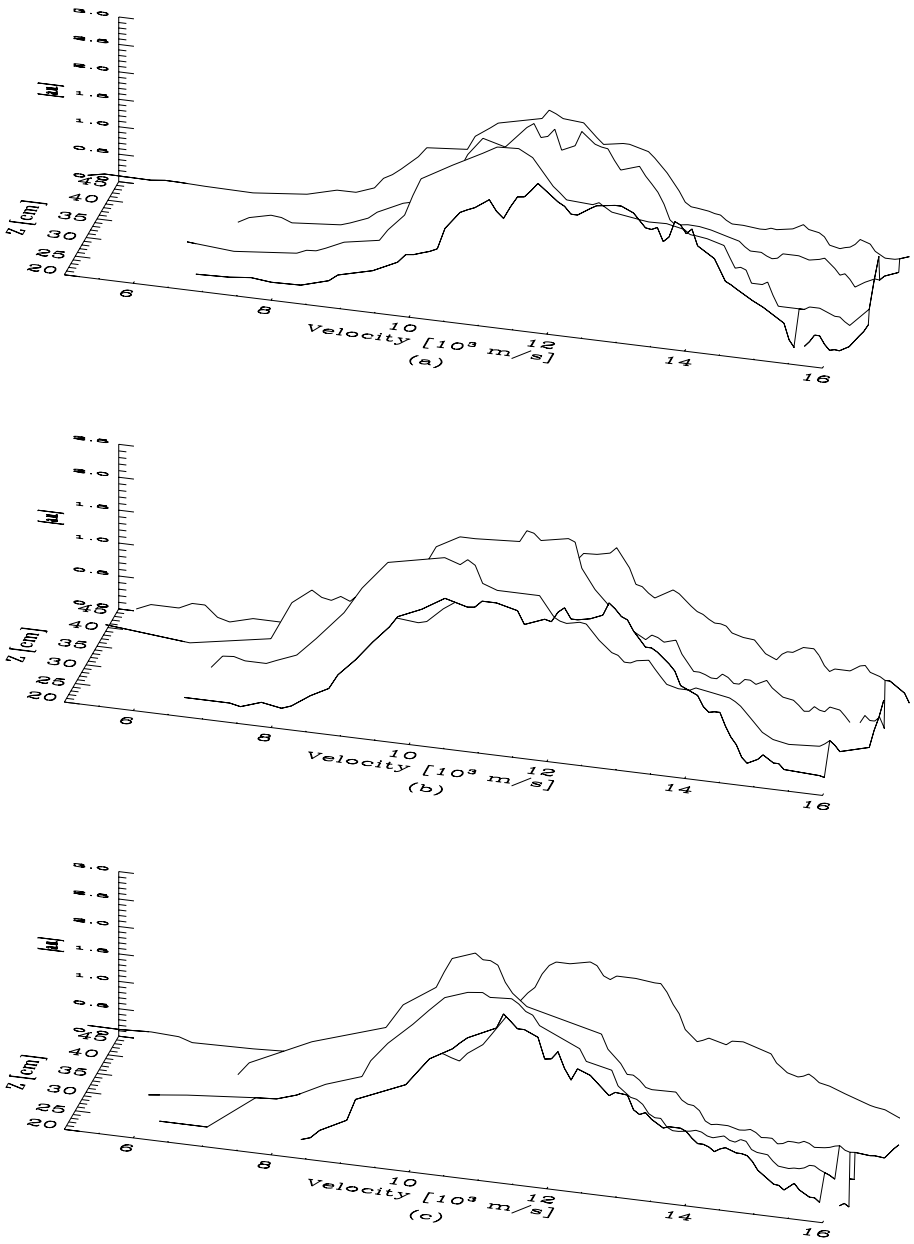

Figure 5.8: Ion velocity distribution as a function of position from the vacuum window. The first distribution is obtained 24 cm from the window and the next 7 cm from the first one, etc. (a) is the results obtained with 230 A coil current and $2 \cdot 10^{-3}$ mbar argon pressure. (b) is obtained with 250 A and (c) with 270 A coil current using the same high pressure as in (a).

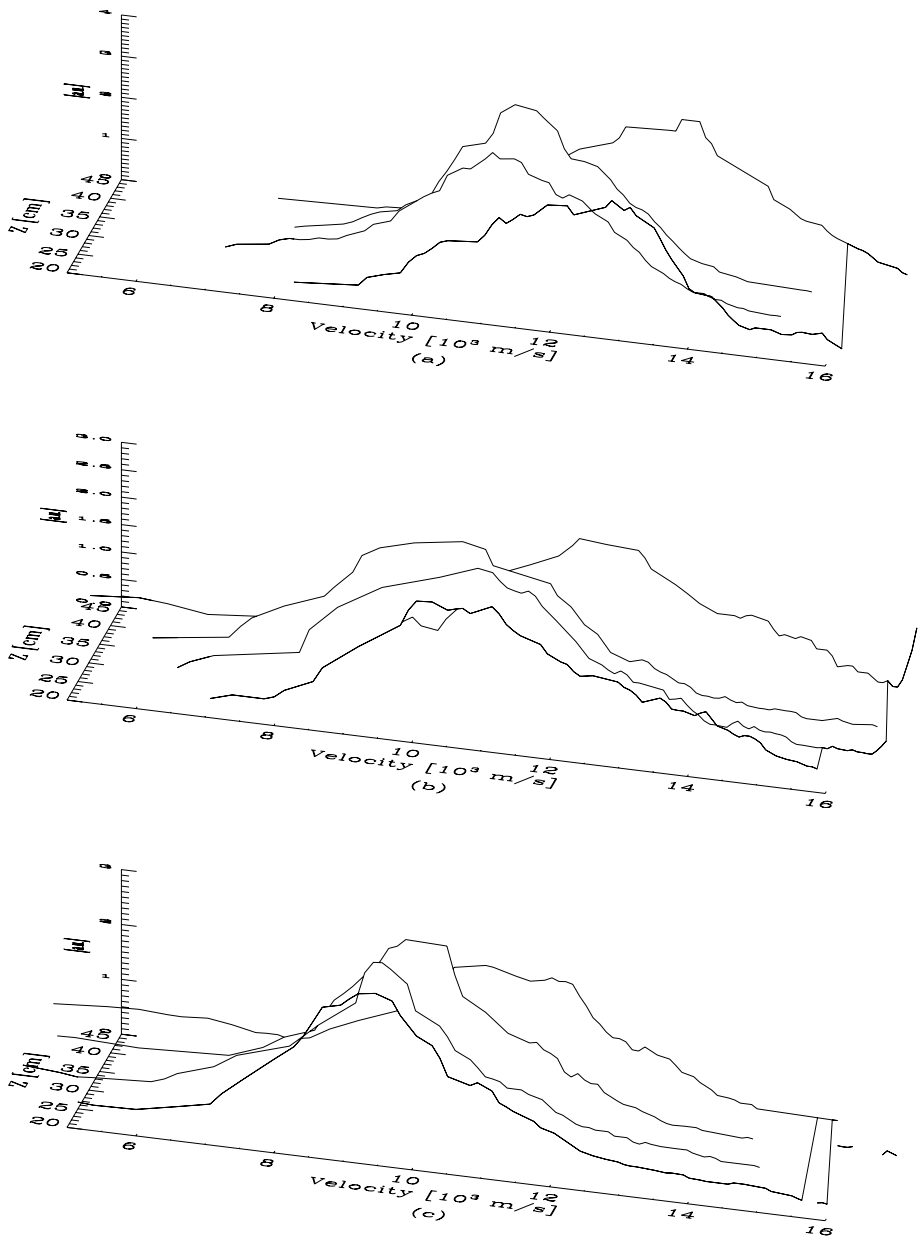

Figure 5.9: Ion velocity distribution as a function of position from the vacuum window. The first distribution is obtained 24 cm from the window and the next 7 cm from the first one, etc. (a) is the results obtained with $5 \cdot 10^{-4}$ mbar argon pressure and 270 A coil current. (b) is obtained with $2 \cdot 10^{-3}$ mbar and (c) with $7 \cdot 10^{-3}$ mbar argon pressure using the same high coil current as in (a).

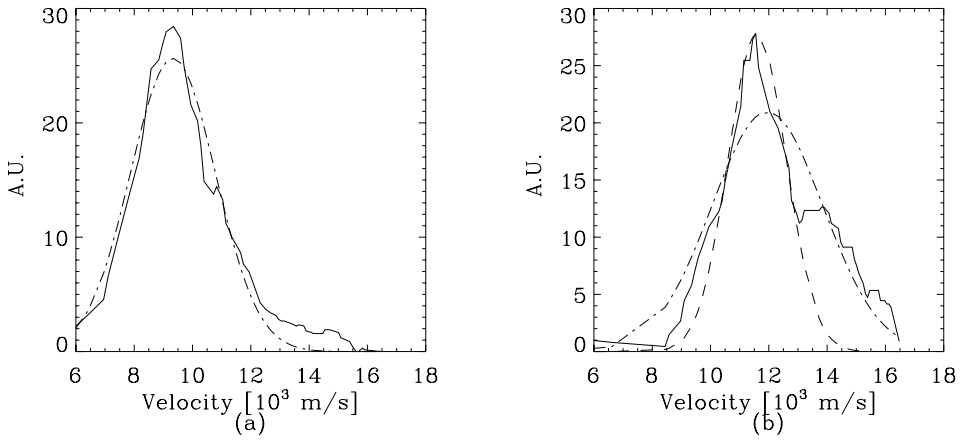

Figure 5.10: Ion velocity distribution

5.4 Ion temperature from the IEA

The ion temperature is obtained by a numerical fit of a Gaussian distribution to the ion distribution measured by the IEA. The temperature is defined as the half-with of the normalized distribution at the value $1/e$ which is found numerically by the fitting procedure. Examples of the numerical fit are shown in figure 5.10. The solid line is the result obtained by a numerical differentiation of the measured IV-characteristic from the IEA. The dashed lines are the functions obtained in the fitting procedure. (a) is an example of a good fit with a resulting temperature of 0.9 eV. This distribution is obtained at the high pressure $7 \cdot 10^{-3}$ mbar and 270 A coil current. (b) is and example of a distribution which is difficult to fit to a Gaussian function. The dash-dotted line is the numerical fit to the 'entire' distribution which indicates an ion temperature of 1.5 eV. The dashed line is the numerical fit when the distribution tail is 'neglected', thus only the distribution from 6 to 13 km/s was fitted, which gave a result of 1.0 eV. This distribution is obtained at a pressure of $2 \cdot 10^{-3}$ mbar and 310 A coil current.

The ion velocity distributions from the contour plots in figure 5.6 and 5.7 are all fitted to a Gaussian to find the corresponding ion temperature. The results are given in figure 5.11 and 5.12. The error bars are estimated from

several fits of the distribution as shown by the example in figure 5.10(b).

In Figure 5.11 the ion temperature versus coil current are shown. The temperature increases from 220 A to 250-260 A and then decreases with increasing coil current. This characteristic are more distinct at 24 and 45 cm from the probe. The maximum ion temperature are obtained at 250-260 A coil current for each position. The largest temperature, $T_i \approx 1.5$ eV, is obtained at the position close to the window and the minimum temperature, $T_i \approx 0.5$ eV, is obtained at high coil current at the largest distance from the window.

In Figure 5.12 the ion temperature dependence with respect to pressure are shown. We can see a "large" dip in temperature at the pressure range around $1 \cdot 10^{-3}$ mbar. This dip is largest in the position furthest away from the window, where $T_i = 0.6$ eV at the minimum.

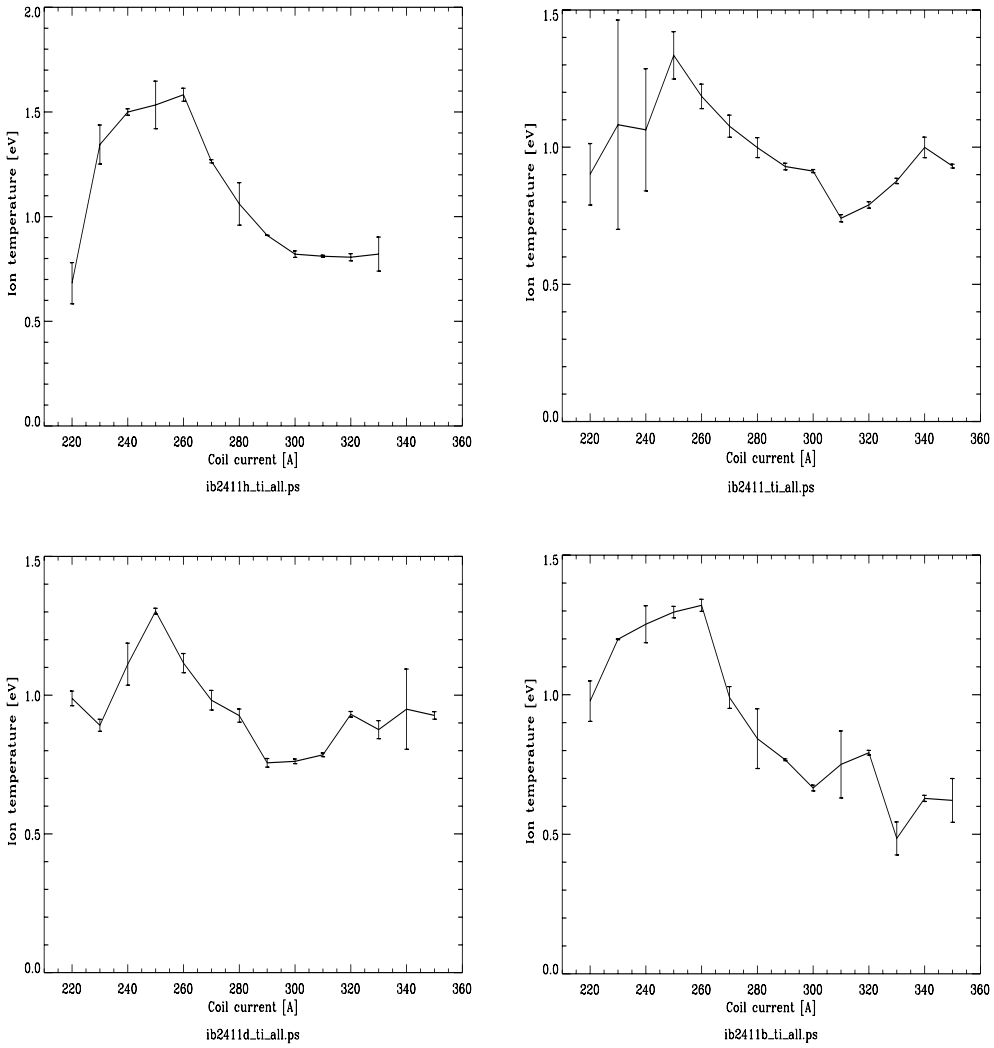

Figure 5.11: Ion temperature

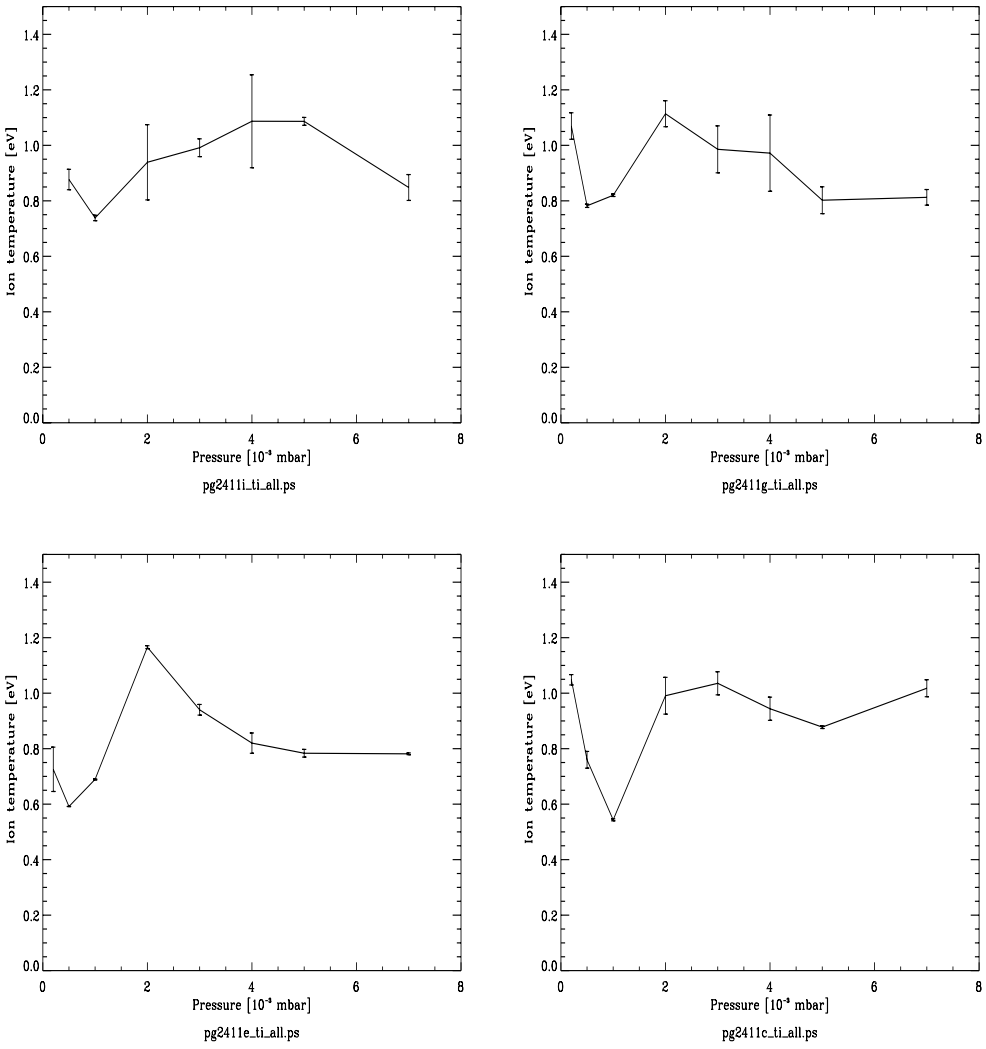

Figure 5.12: Ion temperature

Chapter 6

Discussion

6.1 Axial density results

Figure 5.5(c) shows that the ion densities obtained from the ion-saturation current are constant or decrease slowly in the axial direction from the vacuum window. The density is calculated using the Bohm sheath theory in section 3.1. On the other hand, Figure 5.3(c) shows that the electron density obtained from the Langmuir characteristic increases in the axial direction. Since the plasma is quasi-neutral $n_e \approx n_i$, this is an indication that one of the analysis methods give wrong results.

The electron and ion Larmor radius $r_{Le,i}$ is given by

$$r_{Le,i} = \frac{m_{e,i} v_\perp}{eB}, \tag{6.1}$$

where $v_\perp$ is the electron or ion velocity perpendicular to the magnetic field. At resonance (875 G) the ion Larmor radius is 5 mm at an ion temperature of 0.5 eV and 7 mm when $T_i = 1$ eV. Hence, $r_{Li} > a$ where a is the probe radius (0.2 mm), so the ions can be considered unmagnetized, and the Bohm theory given in section 3.1 can be applied. The electron Larmor radius equals 0.06 mm at resonance for an electron temperature of 5 eV. Hence, $r_{Le} < a$ so that

the electrons are strongly magnetized, and the Langmuir theory developed in section 3.2 is not applicable.

Demidov *et al.* (1999) have developed a kinetic probe theory for magnetized plasmas. In strong magnetic fields the electron distribution is given as

$$f(eV) \propto \frac{1}{r_{Le}} \frac{dj_e}{dV}, \tag{6.2}$$

where j_e is the electron current density to the probe and V the probe voltage. The electron density can be found by integrating equation 6.2 from the minimum energy eV to infinity. If we assume r_{Le} to be roughly constant, not depending on the integral variable, we obtain

$$n_e \propto \frac{1}{r_{Le}} j_e \propto B j_e. \tag{6.3}$$

Thus, the current measured by the probe is proportional to n_e/B. The numerical code used to analyze the Langmuir characteristics presented in this thesis applies a non-magnetized theory where the magnetic field is not included. If we multiply n_e and B from the same axial position we obtain $n_{24}B_{24} \approx n_{45}B_{45}$ within $<$20 %, where index 24 and 45 represent the position. Investigation of the result obtained using 270 A coil current in the high pressure shows that

$$n'_{24} = n_{24}\frac{B_{24}}{B_{45}} = 7.8 \cdot 10^{-16}\mathrm{m}^{-3}, \tag{6.4}$$

where n'_{24} is the density which should be expected at position 24. Comparing the modified density n'_{24} and the density measured in position 45, n_{45}, we see that n'_{24} is 10 % larger than n_{45}. If we compare n'_{24} with the result of n_i obtained from the ion saturation current at the same position, these densities agree within 5 %. This result strongly indicates that the increasing density obtained in the axial scan in figure 5.3(c) is due to the Langmuir analysis, which under-estimate the density at high magnetic fields. We can therefore conclude that the densities given in figure 5.5(c) are reliable.

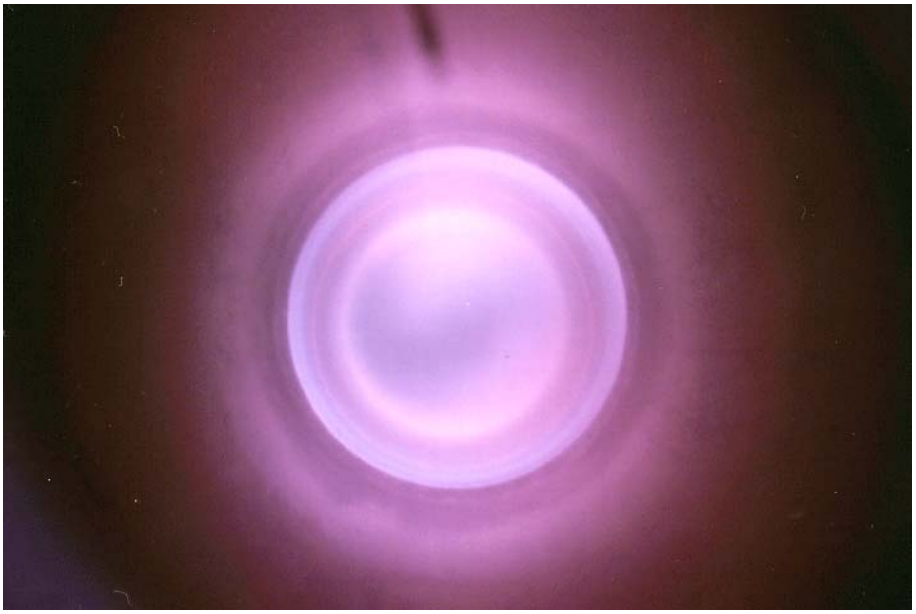

Figure 6.1: Typical light intensity of the argon plasma. View through the axial port.

6.2 The radial temperature peaks

In figure 5.1(a) and (b) we see that the temperature peaks off axis at a radial position 5 cm from center. The most prominent peak is at low pressure where the difference between peak and center is 50 %. The same pattern is obtained from floating potential measurements, which indicates that this has a physical explanation, and can not be explained by errors in the analysis.

Investigation of the light emission from the plasma in a cross-sectional view, shows that the light intensity is at a minimum in the center and increases with increasing radius. This is shown in figure 6.1 by a photograph taken through the axial view port. Gorbatkin *et al.* (1990) observe similar peaks in the temperature, and similar pattern in the light emission. The magnitude of light emitted from the plasma will be proportional to the sum of numerous excitation rates, with the rate $\mathcal{R}$ for an individual process given by

(Gorbatkin *et al.*, 1990)

$$\Re = K n_e n_{Ar,i}, \tag{6.5}$$

where K is the rate constant, which is given similar as equation 2.20, n_e is the electron density and $n_{Ar,i}$ is the argon neutral or argon ion density. Thus, the lack of emitted light intensity may indicate;

i. Lack of electrons,

ii. Lack of neutrals and/or ions,

iii. Low K due to low T_e,

iv. Combination thereof.

A potential contributor to the hollow light emission profile is a hollow radial electric field, characterized by the TM_{01}-mode, which would cause a decreased electron heating in the center, and increased heating at the edge (Gorbatkin *et al.*, 1990). In Gadgil *et al.* (1992) the input microwave power is introduced from a rectangular TE_{10}- to a circular TM_{01}- waveguide mode converter into the vacuum chamber. The results presented here show also that T_e peaks off axis, with a difference of 20 % between maximum and center. This may indicate that the TM_{10}-mode contribute to a nonuniform heating of the plasma. Misina *et al.* (1997) also obtain a radial distribution of T_e with a maxima off the axis and the explanation given is in agreement with the one given above.

Another explanation of the T_e peaks can be given by the existence of secondary electrons caused by Auger emission from the production chamber walls. Some of the ions produced in the resonance zone will hit the wall with an energy ε_{i1}. The wall consist of a metal where the potential energy level for an electron to escape from the conduction band is given by the work function ε_ϕ. An electron with energy $\varepsilon_{e1} \geqslant \varepsilon_\phi$ from within the conduction band can tunnel through the potential barrier ε_ϕ into the ion to neutralize

it. If the electron enters the ground state of the ion the released energy from the neutralization is (Lieberman and Lichtenberg, 1994)

$$\Delta\varepsilon = \varepsilon_{iz} - \varepsilon_{e1} \tag{6.6}$$

Where ε_{iz} is the ionization energy which is released in a neutralization process, and ε_{e1} is the energy required for the electron to escape from the wall and enter the ion. A second electron from within the the conduction band can absorb the excess energy from the neutralization process, and gain an energy equal to $\Delta\varepsilon$.

If $\Delta\varepsilon$ exceeds the energy ε_{e2} required for the second electron to be released from the metal it is free to move away from the wall, and a secondary electron is born. The condition for the release of this electron is most easily met if both electrons come from the top of the conduction band so that $\varepsilon_{e1} = \varepsilon_{e2} = \varepsilon_{\phi}$. The released electron has then a maximum kinetic energy

$$\varepsilon_{max} = \varepsilon_{iz} - 2\varepsilon_{\phi}. \tag{6.7}$$

The ionization energy for argon is 15.8 eV and the work function for stainless steal (Fe) is $\varepsilon_{\phi} = 4.6$ eV (Nordling and Östermann, 1982, Physics Handbook). Thus, the maximum energy for the sputtered electrons is 6.6 eV.

The secondary electrons emitted from the production wall correspond to a radial distance of 5 cm from the center, which equals the temperature peak position. The microwave window coating shown in figure 4.8 indicates a strong sputtering of the chamber walls, which is in agreement with the second theory of the temperature peaks. But we see that the secondary electron temperature of 6.6 eV is 20 % less than the electron peak temperature, which weigh against this hypothesis.

The pattern of the coated film on the window indicates that the wave mode is responsible for the radial non-uniformity. We can also see a non-uniformity with a minimum in the center, for the ion saturation current obtained in figure 5.4(b). On the consequence of the existing data it is difficult to decide what theory to believe, and probably there is a combination of both mechanisms is present..

6.3 Temperature and density versus pressure

The electron temperature decreases with increasing pressure above $2.5 \cdot 10^{-3}$ mbar, see figure 5.1(f). This decrease was expected from the calculation in chapter 2, where temperature versus $n_g d_{\text{eff}} \propto p^{1/2}$ is plotted in figure 2.2. From equation 2.18 we see that $\nu_{en} = K n_g \propto p$. Thus, the temperature decrease can be due to the increasing number of collisions electron undergo with neutrals. This trend of decreasing T_e with pressure is observed by several authors (Forster.J. and Holber, 1989; Gorbatkin *et al.*, 1990).

From equation 2.30 we see that $n_0 \propto d_{\text{eff}}/C_s \propto 1/(T_e p^{1/2})$, thus the results obtained in figure 5.3(f) and 5.4(f) showing an increase in density with pressure from $2.5 \cdot 10^{-3}$ mbar is no surprise. Similar dependence were also observed by other authors (Popov *et al.*, 1994; Forster.J. and Holber, 1989; Gorbatkin *et al.*, 1990) The increase in electron density and ion saturation current may be due to the increase in the number of particles available for ionization when the pressure increases. The decrease observed in the ion saturation current for the low coil current, 5.4(f), at even higher pressures can be explained due to the decrease in electron temperature. Consequently there will be a reduction in ionization rate (Forster.J. and Holber, 1989), or radial plasma losses via collisions with neutral particles, which increase with gas pressure (Popov *et al.*, 1994).

As the pressure decreases below $2.5 \cdot 10^{-3}$ mbar, however, a sudden transition occurs where there is a large change in plasma appearance, which appears as a dip in electron temperature, figure 5.1(f). This dip is also observed for the ion temperature in figure 5.12. This transition is also present in the density/ion saturation results in figure 5.3(f) and 5.4(f). The electron density in the transition regime is $n_e < 7 \cdot 10^{16} \text{m}^{-3} = n_c$, where n_c is the cutoff density for the microwave frequency of 2.45 GHz (Goldston and Rutherford, 1995). Thus, the observed sudden change in plasma mode appearance is believed to be a transition from an overdense $n_e > n_c$, to an underdense mode $n_e < n_c$. The explanation for the changes in the plasma properties is associated with the result of wave propagation phenomena. The left-hand polarized wave can now propagate downstream, whereas at higher densities

they are reflected back to the microwave generator. The right-hand polarized wave propagates towards lower magnetic field, and will "always" be absorbed at or near resonance as treated above. Gorbatkin *et al.* (1990) show that when the pressure decreases the net microwave power measured downstream increases, and they observe an underdense mode in the pressure range $1 \cdot 10^{-4}$ mbar to $3 \cdot 10^{-4}$ mbar, which agrees well with the results presented in this thesis. This gives a good support for this hypothesis. Hence, when the LHP-wave propagates in the underdense regime in the plasma it carries away some of the energy which in the overdense regime is heating the plasma.

6.4 Temperature and density versus coil current

The results in Figure 5.1, 5.3 and 5.4 show that the density increases and the temperature decreases with coil current. To seek an explanation we first consider the calculation done in chapter 2. From equation 2.30 we see that $n_0 \propto d_{\text{eff}}$. When the coil current increases the resonance position moves away from the microwave window towards the probe. This should indicate that the characteristic discharge length, d_{eff}, should decrease with increasing coil current. Hence, n_0 should decrease with increasing coil current, which can not explain the observed increase in n_0.

The magnetic field strength at the probe position increases with increasing current. Therefore, also the interpretation given in section 6.1 fails to provide the right answer for this result.

Hirotsu *et al.* (1994) measure the wave propagation in the plasma produced in a divergent and a uniform magnetic field. The experiments show that the magnetic field strength at the microwave window affects the coupling of the electric field of the injected microwaves with the wave propagating in the plasma. It is considered that, to make good use of the electric field distribution of the TE_{01} mode to generate a uniform dense plasma, it is effective to make the magnetic field strength high at the microwave window.

Thus, by increasing the coil current the magnetic field strength at the window increases. Thus, this might explain the denser plasma and decreasing temperature obtained.

6.5 Ion velocity distribution function

Measurements of the ion energies in ECR plasmas are reported by many research groups. Matsuoka and Ono (1988) and Junck and Getty (1994) measure the ion energy distribution at the substrate using a gridded ion energy analyzer similar to the one used in this thesis. Both groups report similar results as those obtained in Menja when using argon plasma. The peak energy, the width of the distribution (corresponding to T_i) and the plasma potential all decreases with increasing neutral argon pressure.

Hussein *et al.* (1992) used a one-dimensional kinetic code to simulate the ion dynamics in an ECR plasma etching reactor. The work focused on the study of ion-neutral and ion-ion collision effects on the ion distribution function in the downstream region of the source. Their results show that charge exchange and elastic scattering play a significant role in reducing the electrostatic potential variation in the axial direction. For pressures above $1 \cdot 10^{-3}$ mbar the potential drop downstream from the production region is small, which is observed in figure 5.2(d). This means that most of the energy with which ions hit the substrate is gained while crossing the substrate sheath potential. The results shown in figure 5.8 and 5.9 show that the peak energy variation becomes less prominent when the pressure increases, which is in good agreement with the above statement.

From figure 5.2(f) we see that the plasma potential drop is more significant for lower pressure. This drop in plasma potential is also presented in Junck and Getty (1994). The decreasing potential leads to a decrease in the energy gain for the ions crossing the sheath. Hence, this might be the reason for the observed increase in peak velocity for lower pressure as shown in figure 5.7. In addition the ion-neutral collision frequency decreases with decreas-

ing pressure, which also affect the increase in peak velocity with decreasing pressure (Hussein *et al.*, 1992).

Hussein *et al.* (1992) also show that ion-ion collision are responsible for transferring energy from the parallel to the perpendicular direction and hence increasing the perpendicular and decreasing the parallel ion temperature. Thus, the decrease in ion parallel temperature with pressure shown in figure 5.12 can be explained by the increase in ion-ion collision frequency with pressure (the dip in ion temperature is discussed in section 6.3)

Results obtained from the IEA-probe during operation with the ceramic window is presented in Fredriksen *et al.* (1998) and show some discrepancy with the result presented here. This is probably due to different matching of the system with the different microwave windows.

Chapter 7

Conclusion and further research

7.1 Conclusion

With careful consideration of several design factors, implementation of the ECR-plasma source Menja has provided a dense and uniform plasma production in the process chamber. The results presented in this thesis show good agreement with each other, and is shown to be reproducible.

It was found that in the best operating regime, the plasma density is uniform within a variation $<10\%$ over a radial distance of 10-12 cm. The density increases with pressure, magnetic field strength at the microwave window, and input microwave power.

The electron temperature obtains peaks off axis, with a local minimum temperature in the center, which is probably due to the wave modes in the plasma. The plasma is cooled by collisions downstream along the axis. Increase in both pressure and magnetic field results in a decrease in electron and ion temperature.

There is a moderate axial and radial dependence on the plasma potential. The most significant variations are obtained with pressure variations, where the potential decreases with increasing pressure.

The ion energy analyzer was successfully implemented, and the obtained ion energy distributions are in good agreement with the results represented in the literature. The peak ion velocities are around 10-12 km/s which correspond to a ion energy of 20-30 eV at the substrate surface.

7.2 Further research

Successful coating of TiN thin films was made on coins and hard metal cutting tools. The results of the coating are shown in figure 7.1. The deposition was done using a sputter target of titanium in a nitrogen plasma. However, while the coating was performed successfully, the control of the deposition process was insufficient. To achieve a better control and understanding of the deposition process to improve the film quality, further research of the kinetic energies of the impinging reactants are recommended. This involve the ions as well as neutrals and radicals. Up to now, bulk ion energies have been studied extensively in most plasma sources, mainly by means of the gridded energy analyzer without the opportunity to distinguish between different species of ions. A recently acquired energy- and mass analyzer will provide excellent opportunities for further studies in this field.

It should also be interesting to investigate the transition between the low density mode (the underdense plasma) and the high density mode (the overdense plasma) with an electric-field probe. This will measure the electric field intensity from the incident microwave, thus the theory discussed in section 6.3 can be verified.

Figure 7.1: Titanium nitride coating results. Three different results under different operating conditions are shown, and compared with the original Norwegian coin, upper left.

Bibliography

Asmussen, J. Electron cyclotron resonance microwave discharges for etching and thin-film deposition. *J. Vac. Sci. Technol. A 7(3)*, pages 883 – 893, 1989.

Asmussen, J., T. Grotjohn, P. Mak, and M. Perrin. The design and application of electron cyclotron resonance discharges. *IEEE Transactions on plasma science 25(6)*, pages 1196 – 1221, 1997.

Baden Fuller, A. J. *Microwaves*. Pergamon Press, 1969.

Böhm, C. and J. Perrin. Retarding field analyzer for measurements of ion energy distributions and secondary electron emission coefficients in low-pressure. *Rev. Sci. Instrum.64(1)*, pages 31 – 44, 1993.

Bohm, D., E. Burhop, and H. Massey. The use of probes for plasma exploration in strong magnetic fields. In **Guthrie, A. and R. Wakerling**, editors, *The characteristics of electrical discharges in magnetic fields*. McGraw-Hill, 1949.

Charles, C., R. Boswell, and R. Porteous. Measurements and modeling of ion energy distribution functions ion a low pressure argon plasma diffusing from a 13.56 MHz helicon source. *J. Vac. Sci. Technol.A 10(2)*, pages 398 – 403, 1992.

Chen, F. F. Plasma diagnostic techniques. *R.H. Huddlestone and S.L Leonard*, pages 113 – 200, 1965.

Cronin, N. *Microwave and optical waveguides*. Bristol : Institute of Physics Publishing, 1995. ISBN 0-7503-0215-1.

Demidov, V., S. Ratynskaia, R. Armstrong, and K. Rypdal. Probe measurements of electron energy distribution in a strongly magnetized low-pressure helium plasma. *Physics of plasmas*, pages 350 – 358, 1999.

Ferreira, C., M. Moisan, and Z. Zakrzewski. *Physical principles of microwave plasma generation*, chapter 2, pages 11 – 52. Elsevier, 1992. ISBN 0-444-88815-2.

Forster.J. and W. Holber. Plasma characterization for a divergent field electron cyclotron resonance source. *J. Vac. Sci. Technol. A 7 (3)*, pages 899 – 902, 1989.

Fredriksen, Å., A. Aanesland, G. Hellblom, and K. Rypdal. ECR-device for studies of plasmas for thin film PECVD. *1998 ICPP, Praha*, 1998.

Fredriksen, H. The programe bfield.web with examples. Institute of mathematical and physical science, 1995.

Fujiyama, H., H. Kawasaki, T. Fujiyama, and S. Takagi. Sputter coating on high speed steel tube using a hybrid plasma produced by coaxial ECR and magnetron discharges. *Surface and Coatings Technology. 59*, pages 140 – 143, 1993.

Gadgil, P. K., D. Dane, and T. D. Mantei. Anisotropic highly selective eletron cyclotron resonance plasma etching of polysilicon. *J. Vac. Sci. Technol. A 10 (4)*, pages 1303 – 1306, 1992.

Geller, R. *Electron cyclotron resonance ion sources and ECR plasmas.* IOP, 1996. ISBN 0-7503-0107-4.

Goldston, R. J. and P. H. Rutherford. *Introduction to Plasma Physics.* Institute of Physics Publlishing (IOP), 1995. ISBN 0-7503-0325-5.

Gorbatkin, S. M. and L. A. Barry. Contamination by sputtering in a mirror field electron cyclotron resonance microwave plasma sources. *J. Vac. Sci. Technol. A 10 (5)*, pages 3104 – 3113, 1992a.

Gorbatkin, S. M. and L. A. Barry. Poly-si etching using electron cyclotron resonance microwave plasma sources with multipole confinement. *J. Vac. Sci. Technol. A 10 (4)*, pages 1295 – 1302, 1992b.

Gorbatkin, S. M., L. A. Barry, and J. B. Roberto. Behavior of Ar plasmas formed in a mirror field electron cyclotron resonance microwave ion sources. *J. Vac. Sci. Technol. A 8 (3)*, pages 2893 – 2899, 1990.

Guo, H., G. Matthews, S. Davies, S. Erents, L. Horton, R. Monk, and P. Stangeby. Ion temperature measurement in JET boundary plasmas using a retarding field analyser. *Contrib. Plasma Phys.*, pages 81 – 86, 1996.

Hidaka, R., T. Yamaguchi, N. Hirotsu, T. Ohshima, R. Koga, M. Tanaka, and Y. Kawai. 8" uniform electron cyclotron resonance plasma source using a circular TE_{01} mode microwave. *Jpn. J. Appl. Phys. 32 (1)*, pages 174 – 178, 1993.

Hirotsu, N., T. Yamaguchi, R. Hidaka, and M. Tanaka. Production machanism of a large-diameter uniform electron cyclotron resonance plasma generated by a circular TE_{01} mode microwave. *Jpn. J. Appl. Phys. 33 (1)*, pages 2712 – 2717, 1994.

Hussein, M., G. Emmert, N. Hershkowitz, and R. Woods. Effect of collision on ion dynamics in electron-cyclotron-resonance plasmas. *J. Appl. Phys. 72(5)*, pages 1720 – 1728, 1992.

Hutcinson, I. *Principles of plasma diagnostics*. Institute of Physics Publlishing (IOP), 1995. ISBN 0-7503-0325-5.

Junck, K. and W. Getty. Comparison of argon electron-cyclotron-resonance plasmas in three magnetic field configurations. II Energy distribution of argon ions. *J. Vac. Sci. Technol.A 12(3)*, pages 760 – 768, 1994.

Kim, J., E. Lee, J. Baek, and W. Lee. Effects of deposition parameters on composition structure resistivity ans step coverage of TiN thin films

deposited by electron cyclotron resonance plasma-enhanced chemical vapor deposition. *Thin Solid Films*, pages 103 – 109, 1997.

Kosmahl, H. G., D. B. Miller, and G. Bethke. Plasma acceleration with microwaves near cyclotron resonance. *J. Appl. Phys.*, **38**, 4576 – 4582, 1967.

Langmuir, I. and H. Mott-Smith. Studies of electric discharges in gases at low pressures. *Gen. Elect. Rev.*, **27**, 1924.

Lichtenberg, A., M. Schwartz, and D. Tuma. Non-adiabatic and stochastic mechanisms for cyclotron resonance trapping and heating in mirror geometries. *Plasma Physics 11*, pages 101 – 116, 1969.

Lieberman, M. and R. Gottscho. *Design of high-density plasma sources for material processing*, chapter 1, pages 2 – 121. Academic Press, 1994. ISBN 0-12-533018-9.

Lieberman, M. and A. Lichtenberg. *Principles of plasma discharges and materials processing*. Wiley-Interscience, 1994. ISBN 0-471-00577-0.

Ma, D. X., T.-A. Lin, and C.-H. Chen. High selectivity electron cyclotron resonance etching of submicron polysilicon gate structures. *J. Vac. Sci. Technol. A 10 (4)*, pages 1217 – 1226, 1992.

Matsuo, S. and M. Kiuchi. Low temperature chemical vapor deposition method utilizing an electron cyclotron resonance plasma. *Jpn. J. Appl. Phys. 22(4)*, pages L210 – L212, 1983.

Matsuoka, M. and K. Ono. Magnetic field gradient effects on ion energy for electron cyclotron resonance microwave plasma stream. *J. Vac. Sci. Technol. A 6 (1)*, pages 25 – 29, 1988.

Misina, M., Y. Setsuhara, and S. Miyake. Electron cyclotron resonance plasma enhanced direct current sputtering discharge with magnetic-mirror plasma confinement. *J. Vac. Sci. Technol. A 15 (4)*, pages 1922 – 1928, 1997.

Moisan, M. and J. Pelletier. *Microwave excited plasmas*. Elsevier, 1992. ISBN 0-444-88815-2.

Murata, M., S. Uchida, K. Kishimoto, M. Tanaka, A. Komori, and Y. Kawai. ECR plasma CVD in different magnetic field configurations. *Jap. J. Appl. Phys. 3(1)*, pages 1499 – 1502, 1992.

Musil, J. Microwave plasma: its characteristics and applications in thin film technology. *Vacuum 36(3)*, pages 161 – 169, 1986.

Musil, J., F. Žáček, and V. Budnikov. The efficient inject of high microwave powers into the overdense magnetoactive plasma in the waveguide. *Czech. J. Phys. B(23)*, pages 736 – 741, 1973.

Nordling, C. and J. Östermann. *Physics handbook*. CIP, 1982. ISBN 91-44-16574-9.

O'keeffe, P., K. Yamakawa, H. Mutoh, S. Den, and Y. Hayashi. Compact electron cyclotron resonance plasma source optimalization for ion beam applications. *Jpn. J. Appl. Phys.*, pages 4576 – 4582, 1997.

Ono, T., M. Oda, C. Takahashi, and S. Matsuo. Reactive ion stream etching utilizing electron cyclotron resonance plasma. *J. Vac. Sci. Technol. B 4 (3)*, pages 696 – 700, 1986.

Ono, T., C. Takahashi, and S. Matsuo. Electron cyclotron resonance plasma deposition technique using raw material supply by sputtering. *Jpn. J. Appl. Phys. 23(8)*, pages L534 – L536, 1984.

Pitts, R. Retarding field energy analysis for ion temperature measurement in the tokamak edge. *Contrib. Plasma Phys.*, pages 87 – 94, 1996.

Podgornyi, I. *Topics in plasma diagnostics*. Plenum Press, 1971. SBN 306-30489-9.

Popov, O. A. Characteristics of electron cyclotron resonance plasma sources. *J. Vac. Sci. Technol. A 7(3)*, pages 894 – 898, 1989.

Popov, O. A. *Electron cyclotron resonance plasma sources and their use in plasma assisted chemical vapor deposition of thin films*, chapter 2, pages 122 – 233. Academic Press, 1994. ISBN 0-12-533018-9.

Popov, O. A., S. Shapoval, M. Yoder, and A. Chumakov. Electron cyclotron resonance plasma source for metalorganic chemical vapor deposition of silicon oxide films. *J. Vac. Sci. Technol. A 12(2)*, pages 300 – 307, 1994.

Roth, R. *Industrial plasma engineering.* IOP, 1995. ISBN 0-7503-0317-4.

Sakudo, N., K. Tokiguchi, H. Koike, and I. Kanomata. Microwave ion source. *Rev. Sci. Instrum. 48(7)*, pages 762 – 766, 1977.

Seidl, M. High-frequency heationg of electrons in a mirror machine. *Plasma Physics 6*, pages 597 – 616, 1964.

Spee, C., J. Driessen, and A. Kuypers. Low temperature deposition of TiN ceramic material by metal organic and/or plasma enhanced CVD. *Journal De Physique IV C5*, pages 719 – 734, 1995.

Stenzel, R., R. Williams, R. Agüero, K. Kitazaki, A. Ling, T. McDonald, and J. Spitzer. Novel directional ion energy analyzer. *Rev. Sci. Instrum.53(7)*, pages 1027 – 1031, 1982.

Stevens, J., J. Cecchi, Y. Huang, and J. R. Jarecki. Optimized microwave coupling in an electron cyclotron resonance etch tool. *J. Vac. Sci. Technol. A 9(3)*, pages 696 – 701, 1991.

Suzuki, K., S. Okudaira, N. Sakudo, and I. Kanomata. Microwave plasma etching. *Jpn. J. Appl. Phys.*, pages 1979 – 1984, 1977.

Tempermeister, I., N. Blayo, F. P. Klemens, D. Ibbotson, R. Gottscho, and J. Lee. Comparison of advanced plasma sources for etching applications. I. etching rate ,uniformity, and profile control in a helicon and multiple electron cyclotron resonence source. *J. Vac. Sci. Technol.B 12(4)*, pages 2310 – 2321, 1994.

Torii, Y., M. Shimada, and I. Watanabe. Very high current ECR ion source for an oxygen ion implanter. *Nuclear instruments and methods in physics research B21*, pages 178 – 181, 1987.

Wertheimer, M. and M. Moisan. Processing of electronic materials by microwave plasma. *Pure and Appl. Chem. 66(6)*, pages 1343 – 1352, 1994.